

## GUIDELINES AND STANDARDS

# Recommended Standards for the Performance of Transesophageal Echocardiographic Screening for Structural Heart Intervention: From the American Society of Echocardiography

Rebecca T. Hahn, MD, FASE (Chair), Muhamed Saric, MD, PhD, FASE (Co-Chair),  
 Francesco Fulvio Faletra, MD, Ruchira Garg, MD, FASE, Linda D. Gillam, MD, MPH, FASE,  
 Kenneth Horton, ACS, RCS, FASE, Omar K. Khalique, MD, FASE, Stephen H. Little, MD, FASE,  
 G. Burkhard Mackensen, MD, PhD, FASE, Jae Oh, MD, FASE, Nishath Quader, MD, FASE, Lucy Safi, DO,  
 FASE, Gregory M. Scalia, MBBS, FASE, and Roberto M. Lang, MD, FASE, *New York, New York; Lugano, Switzerland; Los Angeles, California; Morristown, New Jersey; Murray, Utah; Houston, Texas; Seattle Washington; Rochester, Minnesota; St. Louis, Missouri; Hackensack, New Jersey; Brisbane, Australia; and Chicago, Illinois*

**Keywords:** Transesophageal echocardiography, Structural heart disease

This document is endorsed by the following American Society of Echocardiography International Alliance Partners: Argentine Federation of Cardiology; Argentine Society of Cardiology; ASEAN Society of Echocardiography; Australasian Society for Ultrasound in Medicine; British Heart Valve Society; Canadian Society of Echocardiography; Chinese Society of Cardiothoracic and Vascular Anesthesiology; Chinese Society of Echocardiography; Cuban Society of Cardiology, Echocardiography Section; Indian Academy of Echocardiography; Indonesian Society of Echocardiography; Iranian Society of Echocardiography; Israel Working Group on Echocardiography; Italian Association of Cardiothoracic Anaesthesiologists; Japanese Society of Echocardiography; Korean Society of Echocardiography; Mexican Society of Echocardiography and Cardiovascular Imaging; National Association of Cardiologists of Mexico, AC; National Society of Echocardiography of Mexico, AC; Philippine Society of Echocardiography; Saudi Arabian Society of Echocardiography; Society of Cardiovascular Images of the Inter-American Society of Cardiology; Thai Society of Echocardiography; The Pan-African Society of Cardiology; Venezuelan Society of Cardiology, Echocardiography Section; and Vietnamese Society of Echocardiography.

From the Columbia University Irving College of Medicine, New York, New York (R.T.H., O.K.K.); New York University Langone Health, New York, New York (M.S.); Instituto Cardiocentro Ente Ospedaliero Cantonale, Lugano, Ticino, Switzerland (F.F.F.); Cedars-Sinai Medical Center, Los Angeles, California (R.G.); Morristown Medical Center, Morristown, New Jersey (L.D.G.); Intermountain Heart Institute, Murray, Utah (K.H.); Houston Methodist DeBakey Heart and Vascular Center, Houston, Texas (S.H.L.); the University of Washington, Seattle, Washington (G.B.M.); the Mayo Clinic, Rochester, Minnesota (J.O.); Washington University, St. Louis, Missouri (N.Q.); Hackensack University Medical Center, Hackensack, New Jersey (L.S.); Prince Charles Hospital, Brisbane, Australia (G.M.S.); and the University of Chicago, Chicago, Illinois (R.M.L.).

The following authors reported no actual or potential conflicts of interest in relation to this document: Muhamed Saric, MD, PhD, FASE, G. Burkhard Mackensen, MD, PhD, FASE, Jae Oh, MD, FASE, Nishath Quader, MD, FASE, Lucy Safi, DO, FASE, and Roberto M. Lang, MD, FASE.

The following authors reported relationships with one or more commercial interests: Rebecca T. Hahn, MD, FASE, has received speaker fees from Abbot Vascular, Baylis Medical, and Edwards Lifesciences; has institutional educational and consulting contracts for which she receives no direct compensation with Abbott Structural, Boston Scientific, Edwards Lifesciences, and Medtronic; has equity with Navigate; and is Chief Scientific Officer for the Echocardiography Core Laboratory at the Cardiovascular Research Foundation for multiple industry-sponsored trials, for which she receives no direct industry compensation. Francesco Fulvio Faletra, MD, has received speaker fees from Philips. Ruchira Garg, MD, FASE, has received grant funding from Abbott Medical, was a coinvestigator during the ADOLL AS trial, completed Abbott Medical consulting services to provide education related to the Piccolo device, is a coinvestigator in the Alterra Adaptive Prentent trial (Edwards Lifesciences), has received funding from the Pediatric Heart Network (National Heart, Lung, and Blood Institute) for the FUEL (completed) and FUEL-OLE trials (Fontan udenafil medication trial), has participated as a coinvestigator for Daiichi Sankyo in the Ennoleate trial (use of

edoxaban oral anticoagulation in pediatric aged patients), and is a consultant for legal case review (ad hoc). Linda D. Gillam, MD, MPH, FASE, is an advisory board member for Edwards Lifesciences and directs core laboratories that have contracts with Edwards Lifesciences and Medtronic (but receives no direct compensation). Kenneth Horton, ACS, RCS, FASE, is a consultant for Edwards Lifesciences, BayLabs, and NeoChord. Omar K. Khalique, MD, FASE, is on the speaker's bureau for Edwards Lifesciences, is a consultant for Cephea Valve, and is director of a CT core lab with trials from multiple device companies (JenaValve, Cephea Valves, Ancora, Lariat) but receives no direct compensation. Stephen H. Little, MD, FASE, has received institutional research support from Abbott, Medtronic, Boston Scientific, 4Tech, and Siemens; and has received personal consulting fees from BayLabs. Gregory M. Scalia, MBBS, FASE, has received fees from Abbott for proctoring regarding the MitraClip. Roberto M. Lang is on the advisory board of Philips Imaging Systems. Dr. Lang has received speaker fees from Philips and Tomtec.

#### Attention ASE Members:

Visit [www.ASELearningHub.org](http://www.ASELearningHub.org) to earn free continuing medical education credit through an online activity related to this article. Certificates are available for immediate access upon successful completion of the activity. Nonmembers will need to join the ASE to access this great member benefit!

Reprint requests: American Society of Echocardiography, Meridian Corporate Center, 2530 Meridian Parkway, Suite 450, Durham, NC 27713 (E-mail: [ase@asecho.org](mailto:ase@asecho.org)). 0894-7317/\$36.00

Copyright 2021 Published by Elsevier Inc. on behalf of the American Society of Echocardiography.

<https://doi.org/10.1016/j.echo.2021.07.006>

## Abbreviations

<b>2D</b> = Two-dimensional
<b>3D</b> = Three-dimensional
<b>AR</b> = Aortic regurgitation
<b>AS</b> = Aortic stenosis
<b>ASD</b> = Atrial septal defect
<b>ASE</b> = American Society of Echocardiography
<b>AV</b> = Aortic valve
<b>CT</b> = Computed tomography
<b>CW</b> = Continuous-wave
<b>DE</b> = Deep esophageal
<b>DT</b> = Deep transgastric
<b>IAS</b> = Interatrial septum
<b>IVC</b> = Inferior vena cava
<b>LAA</b> = Left atrial appendage
<b>LV</b> = Left ventricular
<b>LVOT</b> = Left ventricular outflow tract
<b>MAC</b> = Mitral annular calcification
<b>ME</b> = Midesophageal
<b>MR</b> = Mitral regurgitation
<b>MS</b> = Mitral stenosis
<b>MV</b> = Mitral valve
<b>PA</b> = Pulmonary artery
<b>PFO</b> = Patent foramen ovale
<b>PISA</b> = Proximal isovelocity surface area
<b>PR</b> = Pulmonic regurgitation
<b>PS</b> = Pulmonic stenosis
<b>PV</b> = Pulmonic valve
<b>RVOT</b> = Right ventricular outflow tract
<b>SAX</b> = Short-axis
<b>SVC</b> = Superior vena cava
<b>TAVI</b> = Transcatheter aortic valve implantation
<b>TEE</b> = Transesophageal echocardiographic
<b>TG</b> = Transgastric
<b>TR</b> = Tricuspid regurgitation
<b>TTE</b> = Transthoracic echocardiography

In the American Society of Echocardiography (ASE) guidelines for performing a comprehensive transesophageal echocardiographic (TEE) examination, a standard 28-view (Table 1) imaging protocol as well as specific structural imaging assessments were introduced.<sup>1</sup> Interventional echocardiography is increasingly recognized as a subspecialty requiring advanced training for intraprocedural guidance.<sup>2-4</sup> However, acquisition of preinterventional TEE images by a level II-trained echocardiographer is accepted standard practice. The purpose of the present document is to provide a reference guideline focused on the acquisition of essential preinterventional TEE images that would help identify (1) the mechanism of structural or valvular dysfunction, (2) the hemodynamic and anatomic severity of the disease, and (3) the specific anatomic features that allow appropriate device selection or exclusion. Intraprocedural imaging, whether by transesophageal or intracardiac echocardiography, is not covered, but rather a general approach to TEE screening of the structural target (e.g., aortic valve [AV], mitral valve [MV], or tricuspid valve [TV]; left atrial appendage [LAA]; septal defect) is described. It is not our intent to suggest that complete imaging protocols specific to each structure should be performed in all patients. Rather, protocols should be tailored to be comprehensive but focused on the abnormal structure identified and/or transcatheter intervention under consideration, thus facilitating assessment of device candidacy, procedural planning, and intraprocedural imaging guidance.

The present document is divided as follows: section I offers a review of the comprehensive TEE examination, including basic two-dimensional (2D) and three-dimensional (3D) image acquisition. Section II presents structure-specific imaging protocols for assessment of the AV, MV, pulmonic valve (PV), TV, left atrial appendage, atrial septum, and ventricular septum.

**TV** = Tricuspid valve  
**UE** = Upper esophageal  
**VSD** = Ventricular septal defect

## SECTION I: REVIEW OF THE COMPREHENSIVE TEE EXAMINATION

### A. Two-Dimensional Echocardiographic Acquisition

The American College of Cardiology clinical competence statement on echocardiography<sup>5</sup> addresses the minimum knowledge required for the performance and interpretation of transesophageal and perioperative echocardiography in adults. For structural heart intervention screening, we recommend acquiring the 28 views of the comprehensive TEE examination<sup>1</sup> whenever possible (Table 1). The 2013 transesophageal echocardiography guideline defined the terminology for probe manipulation (Figure 1A), and while the 2013 guideline defines the terminology for four levels of imaging (Figure 1B) as upper esophageal (UE), midesophageal (ME), transgastric (TG) and deep TG (DT), the current guideline adds a fifth level of imaging, the deep esophageal (DE) view

**Table 1** Comprehensive TEE examination views

30 views of the comprehensive TEE examination*
1. ME five-chamber view
2. ME four-chamber view
3. ME mitral commissural view
4. ME two-chamber view
5. ME long-axis view
6. ME AV view
7. ME ascending aorta long-axis view
8. ME ascending aorta SAX view
9. ME right pulmonary vein view
10. ME AV SAX view
11. ME right ventricular inflow-outflow view
12. ME modified bicaval TV view
13. ME bicaval view
14. ME right and left pulmonary veins view
15. ME LAA view
16. TG basal SAX view
17. TG LV midpapillary SAX view
18. TG ventricular apical SAX view
19. TG right ventricular basal view
20. TG right ventricular inflow-outflow view
21. DT five-chamber view
22. TG two-chamber view
23. TG RV inflow view
24. TG long-axis view
25. TG to ME descending aorta (SAX)
26. TG to ME descending aorta (long axis)
27. UE aortic arch SAX to long axis
28. UE aortic arch SAX view
Additional imaging level and views
29. DE right ventricular two-chamber view
30. DE right ventricular inflow-outflow view

RV, Right ventricular.

\*For tables of the original 28 views, see Hahn *et al.*<sup>1</sup>

## HIGHLIGHTS

- Pre-interventional TEE acquired by a level II trained echocardiographer is standard practice.
- The current reference guideline focuses on the acquisition of pre-interventional TEE images that would help accurately identify the mechanism, severity and anatomy of structural/valvular dysfunction.
- Imaging protocols should be tailored to be comprehensive but focused on the abnormal structure identified and/or transcatheter intervention under consideration.
- Appropriate image acquisition will facilitate assessment of device candidacy, procedural planning and intra-procedural imaging guidance.

between the ME and TG levels, which is particularly useful for imaging right heart structures (Table 1, Figure 1B).

In this document we describe the image acquisition required for valvular disease quantitation, but the reader is otherwise referred to the referenced guidelines for details of functional assessment.<sup>6,7</sup> Of note, with any structural heart pathology, an assessment of pulmonary artery (PA) systolic pressure, derived from the tricuspid regurgitant jet and an estimate of right atrial pressure, is recommended.<sup>8</sup> Note that

when tricuspid regurgitation (TR) is severe, this method may be less accurate.<sup>9</sup> There are a variety of methods for assessing PA mean and diastolic pressures if these measurements are required.<sup>10</sup>

### B. Three-Dimensional Echocardiographic Acquisition

The assessment of structural heart disease abnormalities requires a full understanding of 3D technical principles as well as a systematic approach to image acquisition, analysis, and display of the various cardiac structures, including knowledge of the limitations of the different 3D techniques, described in prior ASE guidelines.<sup>11</sup> Advanced 3D imaging display and navigational tools may be helpful (Figure 2). Acquiring 3D volumes of the cardiac structures (i.e., valves and LAA) should be a standard part of the TEE examination, permitting immediate as well as postacquisition processing.

The methods available for 3D data acquisition include (1) simultaneous multiplane or biplane imaging, (2) real-time or live 3D imaging, and (3) electrocardiographically triggered multiple-beat 3D imaging. The 3D study usually starts with real-time imaging modes such as live and narrow-angle acquisition. However, gated 3D modes, including 3D color Doppler, should also be used whenever electrocardiographic gating is possible to take advantage of the improved spatial and temporal resolution of these wide-angle acquisitions (Figure 3).

Current 3D systems have different resolutions for each of the three dimensions, with axial resolution (~0.5 mm) better than lateral or azimuthal (~2.5 mm) and elevational resolutions (~3 mm).<sup>12</sup>

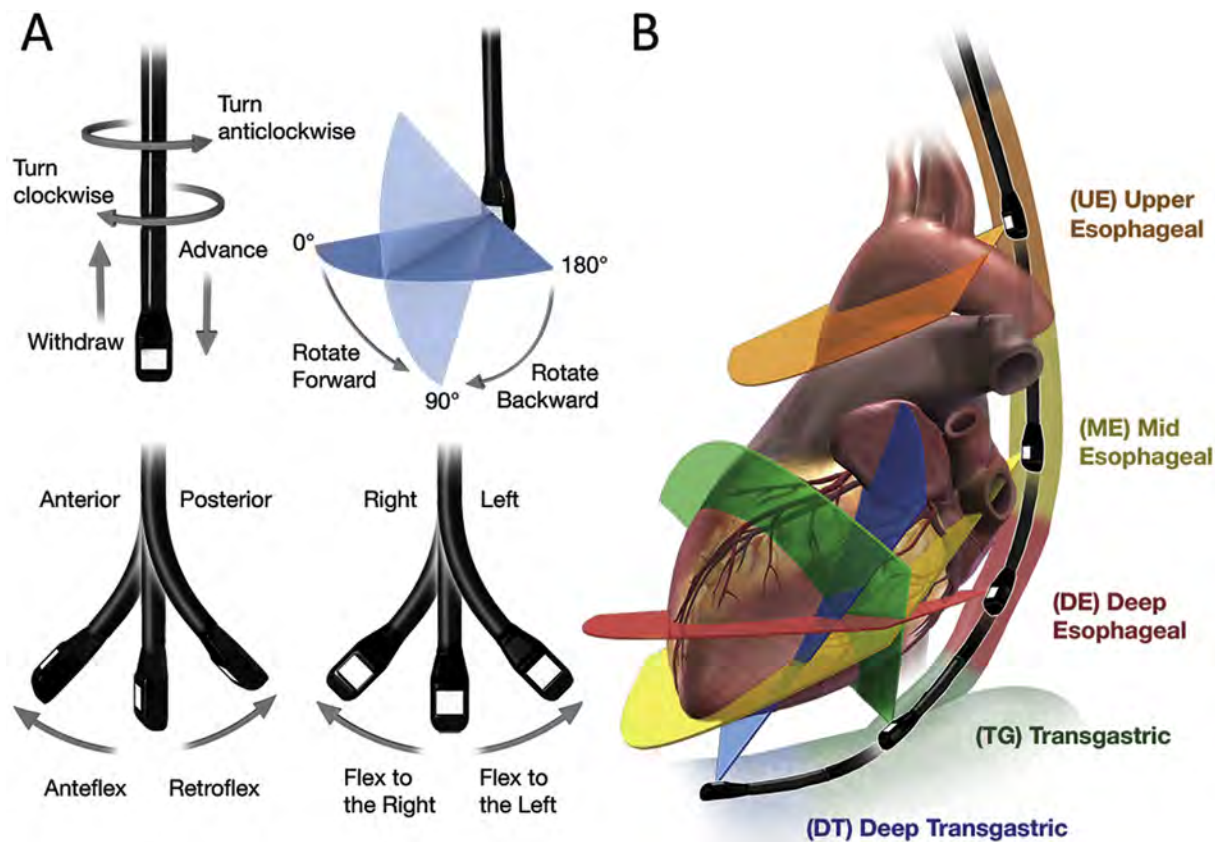


**Figure 1** Probe manipulation and levels of imaging. The terminology for probe manipulation (A) is as follows: (1) advancing or withdrawing the probe within the esophagus, (2) rotating the probe clockwise (toward the right chest) or counterclockwise (toward the left chest), (3) axial flexion of the probe (anteflexion and retroflexion), (4) lateral flexion of the probe (right flexion and left flexion, and (5) mechanical rotation (forward rotating by increasing the degrees of rotation and backward rotating by decreasing the degrees of rotation). The five levels of imaging (B) are UE, ME, DE, TG, and DT.

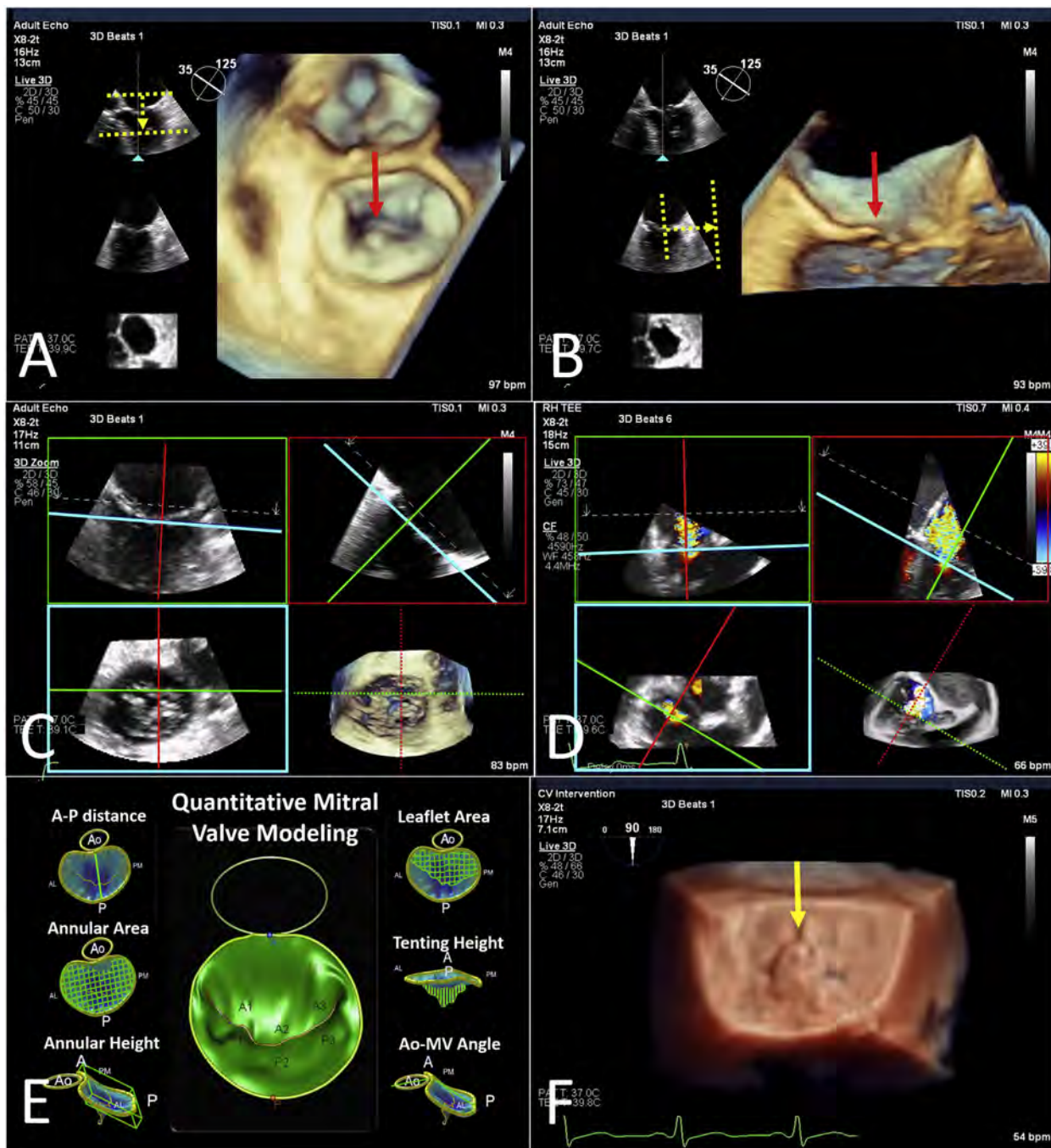


**Figure 2** Real-time 3D image cropping and rendering tools. Real-time cropping of the volume-rendered image can be performed with on-cart cropping tools. In a patient with a flail MV P2 segment (**A** and **B**, red arrow), real-time cropping tools allow the imager to rapidly position the crop plane (yellow lines), resulting in the real-time display of the MV from a surgeon's view (**A**) or looking at the lateral commissure (**B**). Panels **C** and **D** are examples of real-time 3D multiplanar reconstruction of the TV (without and with color Doppler, respectively), with on-axis alignment of the tricuspid regurgitant coaptation gap (blue lines) and a SAX image of the regurgitant orifice in the blue plane (blue box). Various rendering tools such as surface rendering (**E**) and photorealistic imaging (**F**, yellow arrow points to a flail P2 segment) may be useful. A, Anterior; AL, anterolateral; Ao, aorta; P, posterior; PM, posteromedial.

These differences create “nonisotropic voxels” such that slight changes in imaging angles or levels may result in a different 3D echocardiographic appearance of the same cardiac structure. Awareness of these limitations will help determine the best imaging plane(s) for a specific abnormality. Optimization and alignment of cross-sectional 2D imaging planes within the 3D volume, or multiplanar reconstruc-

tion, allows accurate quantification of structural dimensions and areas. Measuring directly on a 3D-rendered image is discouraged because (1) the object to be measured may be off axis in the 3D volume, changing the structural appearance compared with an on-axis image (i.e., parallax), and (2) increased slice thickness of a 3D volume may accentuate structures in the near or far field, preventing a clear

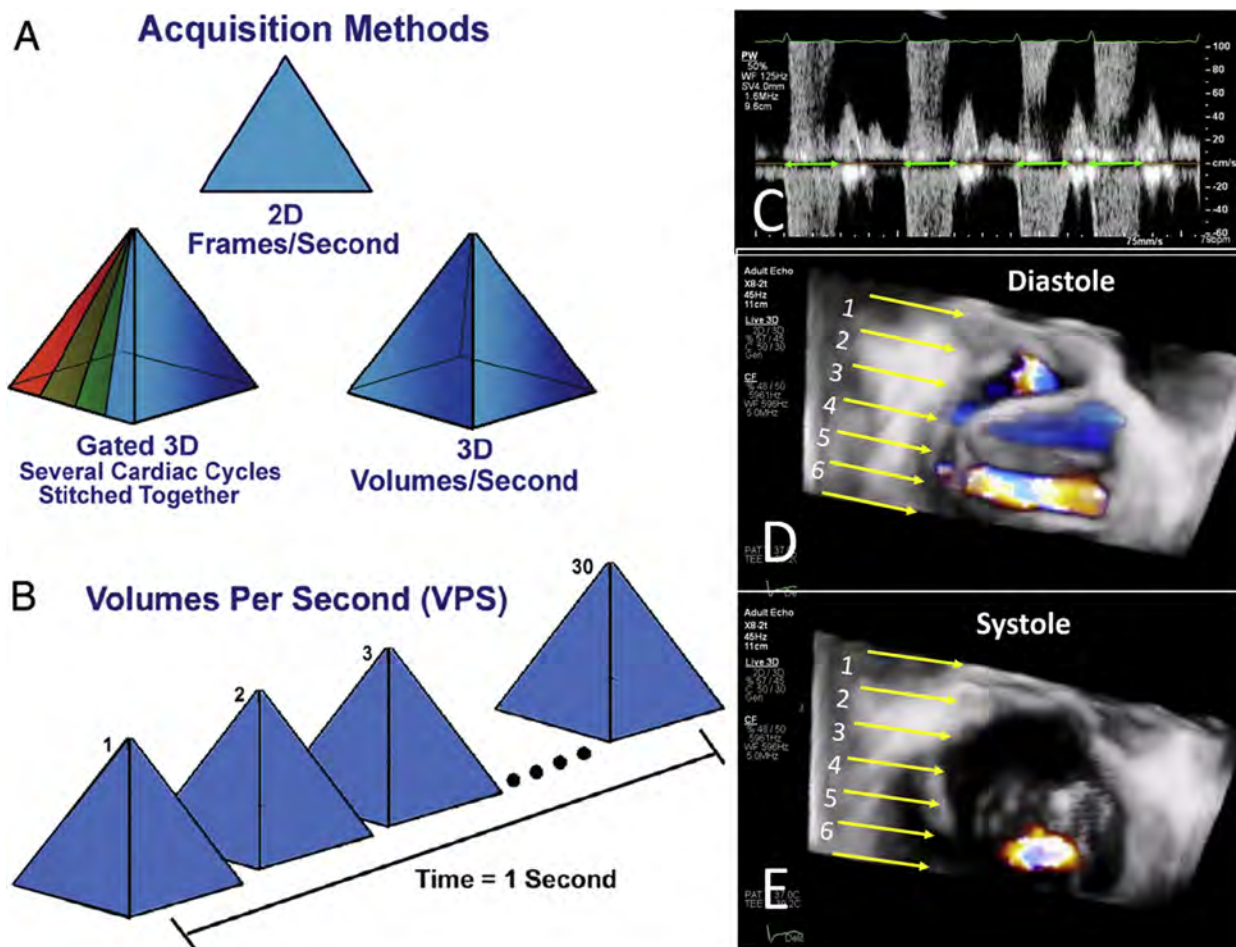


**Figure 3** Three-dimensional volume acquisition methods. Three-dimensional images can be acquired as a single-beat 3D volume or multibeam spliced volume (**A**). To increase the temporal and spatial resolution of a 3D image, splicing acquires narrow volumes of information over several heartbeats and then stitches them together to create a larger volumetric data set. This method of data acquisition compensates for the poor temporal resolution of a single-beat full volumetric real-time 3D echocardiographic acquisition (**B**). In a patient with atrial fibrillation, the systolic time interval shows less variability (**C**, green arrows) compared with the diastolic time interval. Thus, in a 3D color Doppler volume of MV regurgitation using six subvolumes (**D**, **E**), stitch artifacts in diastole (**D**) may not be prominent in systole (**E**), although undetectable splice artifacts can exist. Panels **A** and **B** reproduced with permission from Lang *et al.*<sup>11</sup>

delineation of the structure of interest. A three-step approach, described in [Figure 4](#), can be used to align a 2D imaging plane within the 3D volume using on-cart software. More recent advances (real-time multiplanar reconstruction) enable 2D reconstruction of real-time 3D acquisitions. A multibeam spliced image is not typically used when precise measurements (e.g., aortic annular area or perimeter) are required because undetectable splice artifacts may significantly affect the measurements. When multibeam acquisitions are required (e.g., to optimize volume rates), using this multiplane display will depict the subvolumes in the elevational plane, allowing the imager to choose multibeam volumes without obvious splice artifacts. Other 3D artifacts are listed in [Table 2](#).<sup>13</sup>

## SECTION II: STRUCTURE-SPECIFIC IMAGING PROTOCOLS

### A. Assessment of the AV

Transcatheter AV implantation (TAVI) has become standard therapy for many patients with severe aortic stenosis (AS).<sup>4</sup> In addition, commercially available<sup>14</sup> and investigational<sup>15,16</sup> devices have been used to treat native aortic regurgitation (AR). Although its role has

evolved, echocardiography continues to be essential before, during, and after TAVI.<sup>17</sup> Preprocedural TEE imaging to evaluate the AV and aortic root complex may be appropriate, particularly when contrast-enhanced computed tomography (CT) is contraindicated or unavailable or when anatomic features seen by transthoracic echocardiography (TTE) raise concern for TAVI feasibility or suggest a high risk for complications. Physicians involved in the care of TAVI patients should be familiar with the acquisition and interpretation of relevant TEE images and be able to use them for shared decision-making before interventions.<sup>3</sup>

**1. AV Anatomy.** The AV is composed of three cusps attached in a semilunar fashion along the entire length of the aortic root, with the highest point of attachment at the level of the sinotubular junction and the cusp nadirs defining the “virtual annulus”<sup>18</sup> ([Figure 5](#)). Short-axis (SAX) images from the aortic side at the level of the cusps ([Figures 5A](#) and [5B](#)) are the most useful for determining cusp morphology and pathology. Imaging from the left ventricular (LV) side ([Figures 5C](#) and [5D](#)) may uncover subvalvular pathologies. The majority of the annulus is composed of the base of the interleaflet

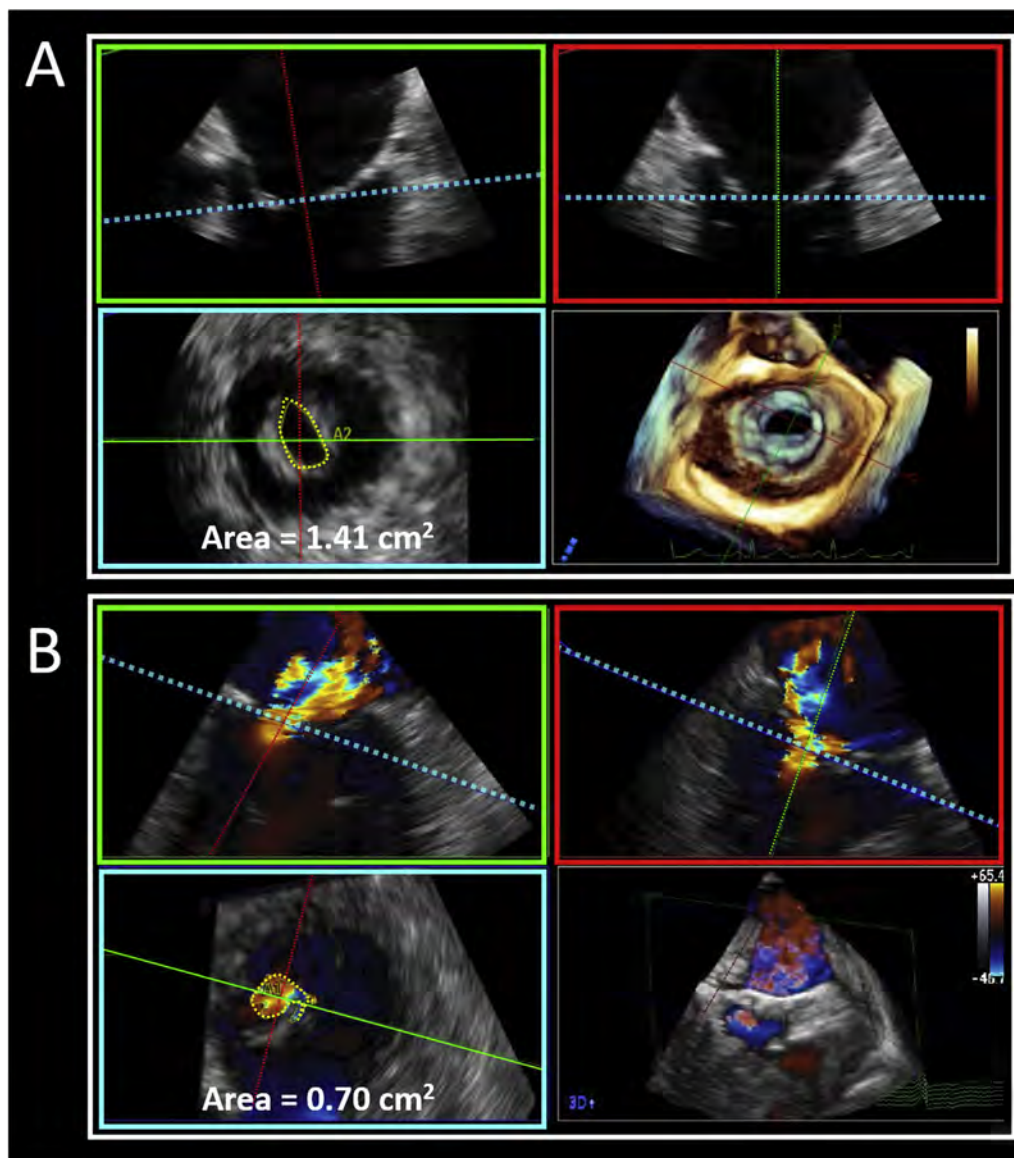


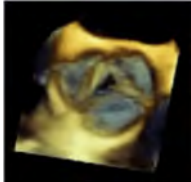
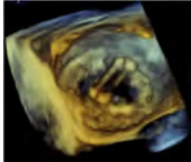
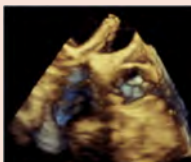
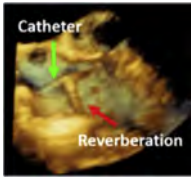
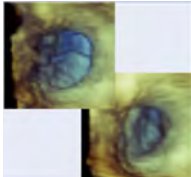
**Figure 4** Three-step approach to quantify cardiac structures. Step 1: two orthogonal 2D planes (*green and red boxes*) are oriented perpendicular to the structure to be measured. In the examples shown, the *green and red planes* are perpendicular to the MV orifice (**A**) or the regurgitant MV color Doppler jet (**B**). Step 2: the third orthogonal 2D plane (*blue box*) is now the SAX view and is positioned at the level of the structure to be measured. In the examples shown, the *blue plane* is placed at the level of the mitral leaflet tips (**A**) or regurgitant vena contracta (**B**). Step 3: the structure in the SAX plane (*blue box*) is measured. In the examples shown, the MV area (**A**) or vena contracta area (**B**) is planimetered. Note that the 3D image in the lower right-hand corner can be used to confirm the orientation of the three orthogonal imaging planes.

triangles, or trigones (Figures 5E and 5F). The ventricular-arterial junction between the ventricular myocardium and fibroelastic wall of the aortic root has muscular and fibrous elements and includes the mitral-aortic curtain and membranous septum and adjacent conduction system.<sup>19</sup> The length of the membranous septum may be an important anatomic predictor of heart block following TAVI.<sup>20</sup>

**2. General Imaging Protocol for the AV (Table 3).** *ME Views.* ME SAX (40°–60° mechanical rotation), long-axis (110°–140° mechanical rotation), or biplane imaging of the AV (Figure 6) is integral for assessing valve morphology: a tricuspid AV (Figures 6A and 6B) or bicuspid AV (Figures 6C and 6D) can be distinguished by visualizing cusp opening and closing

with 2D (Figures 6A and 6C) or color Doppler (Figures 6B and 6D) imaging. The long-axis view of the AV is essential for analyzing leaflet pathology (Figures 6E and 6F), the basal LV septum, and sub-aortic pathology. Aortic measurements are performed from the ME long-axis view at end-diastole, using the leading edge-to-leading edge technique (Figures 7A and 7B).<sup>21</sup> The aortic annular diameter is measured in the sagittal plane, from a high-resolution, zoomed ME long-axis view of the AV with the LV outflow tract (LVOT) aligned with the aortic root, perpendicular to the ultrasound beam (Figure 7C). From this view, the interleaflet trigone between the non-coronary and left coronary cusps is typically seen posteriorly, while the image should bisect the right coronary cusp anteriorly with the leaflet nadir identifying the level of the annulus (Figure 7D). The

**Table 2** Artifacts of 3D imaging

Type of artifact	Mechanism	Impact on images	3D example
Stitching	Incorrect juxtaposition at the interface of sequential subvolumes (because of arrhythmias, breathing, probe/patient motion)	Strong demarcation between subvolumes leading to a “broken” image	
Dropout	Poor echocardiographic signal strength due to weak echoes	These artifacts can be misdiagnosed as true holes/perforations	
Blurring	Indistinct edges of structures due to the assembly of nonisotropic voxels (2° to differences in axial > lateral > elevational resolution)	Thin structures (i.e., sutures) appear thicker than they are	
Blooming	Metallic structures when intersected by ultrasound produce fringes extending beyond the borders of the metallic devices/catheters	Metallic structures appear with irregular, thick edges	
Railroad-shaped	In large catheters with wide lumens, two surfaces are perpendicular to the ultrasound beam, producing strong echoes, while the other two are tangential, producing very weak echoes	Single catheter appears as two linear structures	
Reverberations	Multiple reflection of metallic component of catheters	Depending on the perspective and the position of catheter, reverberations may appear to lengthen the catheter	
Shadowing	Inability of ultrasound to pass through strong reflecting catheters/devices	Lack of tissue posterior to catheters/devices that may appear as a “tear” of cardiac structures	
Gain	Variation of gain may produce significant variation in the size of structures	Orifices may appear larger or smaller according to gain variation	

LVOT or annular measurement in systole should use the right cusp hinge as the anterior point of measurement and the posterior aortic root at the base of the interleaflet trigone (perpendicular to the aortic root) as the posterior point. Although guidelines suggest that the LVOT measurement should be made 0.5 to 1.0 cm from the annulus, studies indicate that calculating AV area using the LVOT measured at the annulus is more reproducible and accurate.<sup>22,23</sup> Other aortic anatomy, such as the coronary height above the annular plane and length of the AV cusps, can be measured from 2D reconstructed images using a 3D zoomed volume (Figure 7E). This information is used to determine the risk for coronary artery occlusion during valve deployment or balloon valvuloplasty. Three-dimensional rendered or multiplanar imaging can also be used to define morphology and quantify valve area or regurgitation severity (Figure 8).

**TG and DT Views.** DT views are essential for assessing AV function. The DT five-chamber view (Figure 9A) is important for comprehensive Doppler assessment of AV function. With AS, the pulsed-wave Doppler sample volume is positioned just proximal to the flow convergence in systole (Figure 9B), whereas for AR, the sample volume should be at the level of annulus in systole. The stroke volume is calculated using the systolic LVOT diameter from ME views (Figure 7A,C). Continuous-wave (CW) Doppler across the AV is used (Figure 9C) to calculate AV area. A TG long-axis view at 80° to 120° should be attempted (Figure 9D), as this imaging plane typically will allow ultrasound beam alignment with jets that are directed more anteriorly or toward the right. Studies have suggested that up to 50% of patients with AS will have the maximum velocity recorded from the right parasternal window on TTE,<sup>24</sup> and the TG view at 80° to 120° is a close approximation of this imaging window. If a forward stroke volume is required for calculation of AR volume, then the right ventricular outflow tract (RVOT) stroke volume should be acquired (Figure 9E–9H). For accurate assessment of stroke volume, we recommend obtaining PW Doppler from the TG or DT view for both the LVOT and RVOT calculations. Alternatively, the UE view can be used for RVOT stroke volume if the TG views are not feasible and this alternative view is aligned with the ultrasound beam.

**3. AV Stenosis. Valve Morphology and Severity of AS.** The severity of AS is accurately determined by transthoracic 2D and Doppler echocardiography.<sup>7</sup> In the setting of nondiagnostic TTE, TEE imaging can be used to determine the morphology of the AV and aortic root. Whereas prior studies had questioned the accuracy of 2D and 3D planimetry of the AV area,<sup>25</sup> more recent studies have suggested that 2D planimetry of the AV area with TEE imaging is accurate compared with 3D *ex vivo* scanned valves<sup>26</sup> as well as CT.<sup>27,28</sup> However, this method requires experience to identify the appropriate image of the leaflet tips without acoustic dropout and may not be possible in 15% to 25% of studies.<sup>27,28</sup>

**Aortic Annulus and Root.** Measurement of the “virtual annular” perimeter, diameter, or area may be used to size TAVI valves. A user-defined 3D zoom acquisition should be acquired to perform these measurements, being careful to include the entire annulus, but limiting the size of the volume to optimize frame rate (Figure 10). Once the annulus is identified on multiplanar reconstruction (Figure 10A), measurements of the annular area, perimeter, and orthogonal diameter can be performed. Manual indirect methods (Figure 10B) have been validated against CT,<sup>17</sup> but more recently introduced automated software packages (Figures 10C and 10D) still require adequate validation.

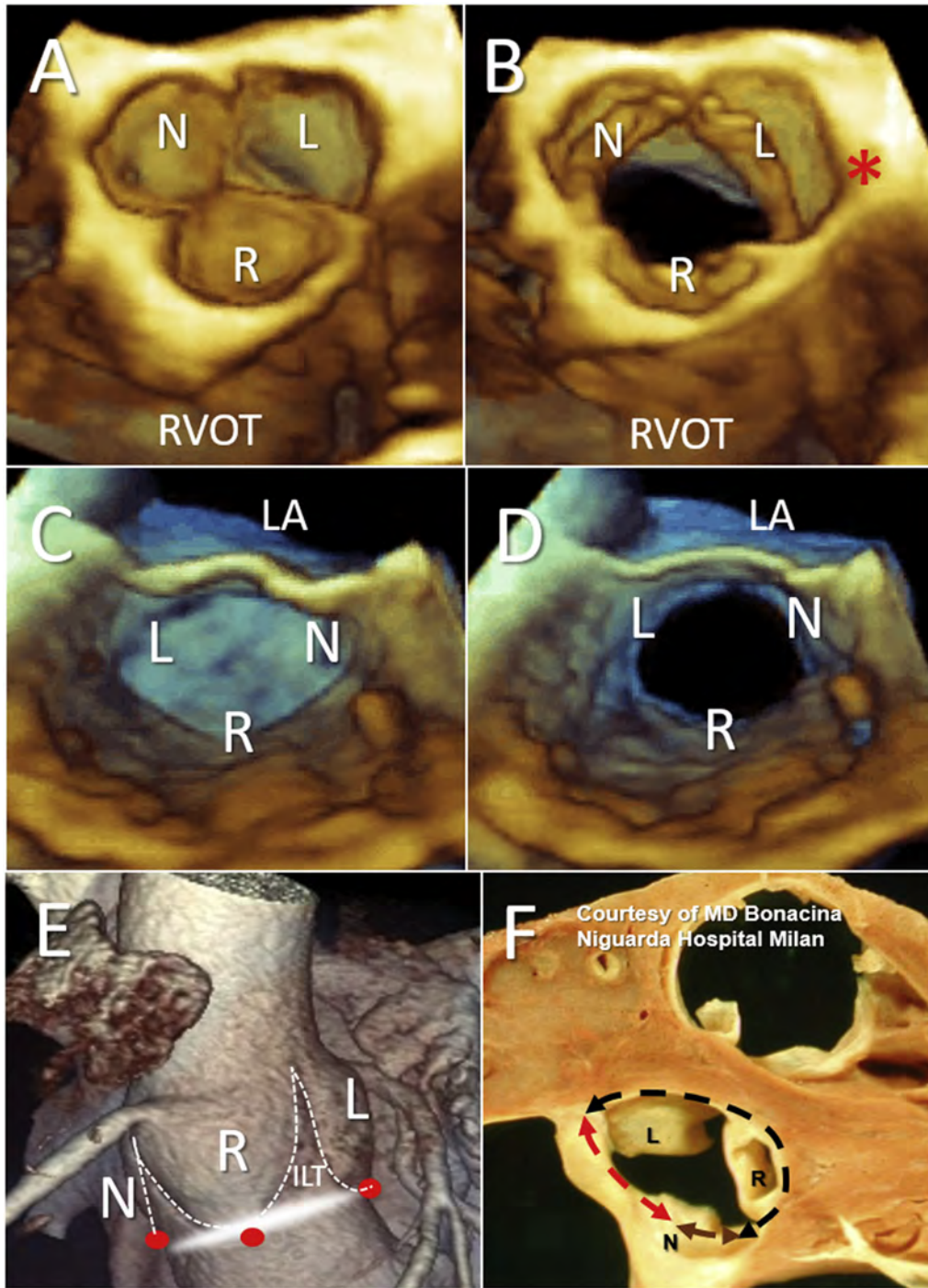
**4. AV Regurgitation. Valve Morphology and Severity of AR.** Assessing AR uses the same imaging windows as for AS and includes annular measurements and assessment of risk for coronary artery obstruction (Figure 7). Although TTE may be sufficient to assess AR severity, TEE imaging is frequently needed to assess the AR mechanism (Figure 11) and for further quantification of eccentric jets, as these may be difficult to visualize with TTE.<sup>1,6,29</sup>

**AR Quantitation.** Doppler assessment of AR should be attempted whenever the jet is aligned with the ultrasound beam. Because leaflet prolapse is a common etiology of AR (Figure 12A), regurgitant jets may be eccentric and thus aligned parallel to the ultrasound beam from on-axis (or slightly off-axis) ME views (Figure 12B). Assessment with CW (Figure 12C) and color (Figure 12D) Doppler can be performed. If the AR jet is perpendicular to the ultrasound beam from ME views, Doppler assessment can be performed from DT views. This assessment should include proximal isovelocity surface area (PISA) quantitation when possible (Figure 12E), LV stroke volume calculation, using pulsed-wave Doppler with the sample volume at the level of the aortic annulus (Figure 12F), and CW Doppler to assess AR pressure half-time, velocity-time integral, and jet density (Figure 12G). It is important to remember that color Doppler jet area and length should not be used to quantify AR and that the width of the vena contracta may be overestimated from TG views because of suboptimal lateral or azimuthal resolution. Diastolic flow reversal in the descending aorta should be assessed from both TG (Figure 12H) and mid to high esophageal (just distal to the aortic arch) views; significant AR is more likely when holodiastolic flow reversal is detected in distal portions of the aorta (Figure 12I).

## D. Assessment of the MV

**1. MV Anatomy.** The MV is a complex structure comprising the left atrial wall and annulus, leaflets, commissures, chordae tendineae, papillary muscles, and left ventricle.<sup>30–32</sup> The mitral annulus is defined by the convergence of the atrial and ventricular muscular walls, the hinge line of the mitral leaflets, epicardial adipose tissue, a discontinuous cord of fibrous tissue on its posterior aspect, and a band of robust connective tissue (mitral-aortic curtain or intervalvular fibrosa) on its anterior aspect (Figure 13A).<sup>33</sup> The mitral annulus is often described as having a saddle-shaped morphology on 3D studies with anterior and posterior peaks, and with nadirs near the fibrous trigones.<sup>34</sup> The horn of the saddle is the continuous transition from the anterior MV leaflet to the mitral-aortic curtain (Figure 13B); however, the hinge point of the anterior mitral leaflet is ventricular to the aortic annulus (Figure 13C), making the anterior horn more virtual rather than a well-defined anatomic structure. Measurement of the annulus on multimodality imaging often uses the trigone-to-trigone distance, converting the annulus into a “D-shaped” structure; the straight component is conventionally named the anterior mitral annulus, while the curved component is the posterior mitral annulus (Figure 13A).<sup>35</sup>

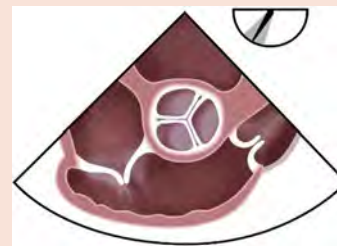
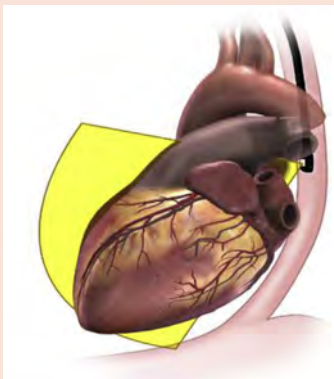
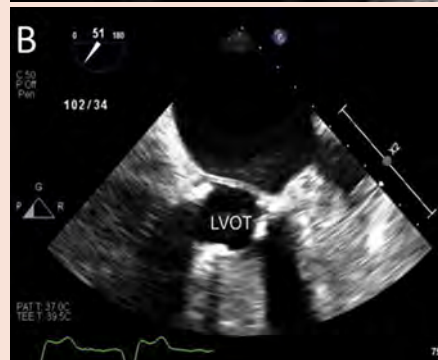
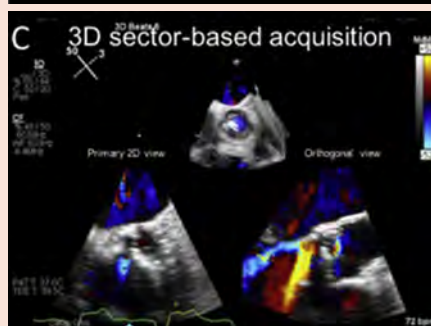
Two leaflet segmentation schemes have been proposed: the original Carpentier classification<sup>36</sup> and a modification thereof.<sup>37</sup> Because the posterior leaflet typically has two well-defined indentations, the classic Carpentier scheme refers to separate scallops as P1 (anterolateral), P2 (middle), and P3 (posteromedial). The anterior leaflet is typically devoid of indentations, and its segments are named according to the opposing posterior leaflet scallops: A1, A2, and A3 (Figure 13A). Commissural tissue varies from several millimeters to



**Figure 5** Anatomy of the AV and annulus. Panels **A** and **B** are 3D TEE images showing the AV leaflets from an aortic perspective in **(A)** systole and **(B)** diastole. The left coronary cusp (L) lies below the ostium of the left main coronary artery (*red asterisk*, **B**). The anteriorly positioned right coronary cusp (R) is adjacent to the RVOT (note that the right coronary artery is not imaged). The noncoronary cusp is adjacent to the IAS. Imaging from the ventricular perspective in **(C)** systole and **(D)** diastole helps identify LVOT abnormalities. The aortic root and sinuses of Valsalva **(E)** are shown by computed tomographic images (electronic endocast). The *dotted line* follows the hinge of the leaflets, which assumes a crown-shaped configuration. The three *red dots* identify the nadir of the hinge lines and thus the plane of the “virtual annulus” (*white ellipse*). The noncoronary sinus of Valsalva (N), right sinus of Valsalva (R), and left sinus of Valsalva (L) are noted. This anatomical specimen **(F)** shows the ventricular-arterial junction, which is partially muscular (*black dotted double arrow*) and partially fibrous (*red and violet dotted double arrows*). The fibrous component comprises the mitral-aortic curtain (*red double arrow*) and the membranous septum (*violet double arrow*). *ILT*, Interleaflet triangle; *L*, left coronary cusp or sinus of Valsalva; *LA*, left atrium; *LVOT*, left ventricular outflow tract; *N*, noncoronary cusp or sinus of Valsalva; *R*, right coronary cusp or sinus of Valsalva; *RVOT*, right ventricular outflow tract.

**Table 3** AV imaging protocol**Imaging level: ME AV SAX view 40°–60°****Acquisition protocol:**

- Clockwise or counterclockwise rotation of the TEE probe will show various aspects of the AV or prosthesis.
- Counterclockwise rotation or retroflexion for visualization of LVOT SAX.

**Planar imaging****Volumetric imaging****Functional imaging**

(Continued)

**Table 3** (Continued)

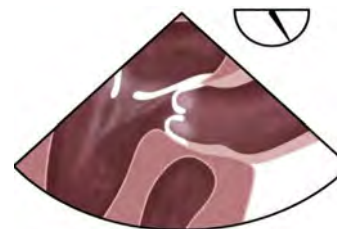
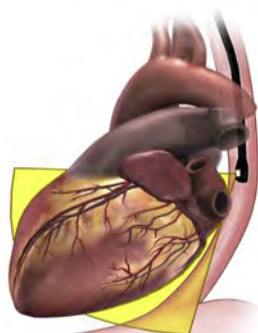
**Imaging level: ME AV SAX view 40°–60°**

- |   |  |  |
|---|--|--|
| <p>A. AV ME SAX images showing three aortic valve leaflets in systole.</p> <p>B. Counterclockwise rotation, retroflexion, or advancement from A to visualize LVOT just below the AV leaflets.</p> | <p>A. User-defined 3D acquisition in triplane view from a primary ME SAX view ensuring acquisition of entire aortic root. The primary view and two orthogonal planes are represented in the triplane display.</p> <p>B. Three-dimensional en face view of the AV during systole demonstrating leaflet anatomy.</p> <p>C. Three-dimensional sector-based color Doppler from the primary ME SAX view in biplane view ensuring inclusion of central AR jet in volume set. For assessment of the central AR jet, it is not necessary to acquire the entirety of the annular plane.</p> | <p>A. Biplane color Doppler imaging from primary ME SAX view with tilt plane off-center elucidates paravalvular leak from outer edge of medial aspect of prosthetic sewing ring on the orthogonal view on the right.</p> <p>B. SAX color Doppler image demonstrating AR arising from the center of leaflet coaptation.</p> |
|---|--|--|

**Imaging level: ME AV long-axis view 110°–140°**

Acquisition protocol

- Maneuver: advance, anteflex.
- Add biplane views as needed.
- Probe advancement ± anteflexion used to see ventricular aspects of prosthetic frame or native/prosthetic leaflets.
- Probe withdrawal ± retroflexion used to see aortic aspects of prosthetic frame or native/prosthetic leaflets.
- Required angle for LVOT and AV imaging is often >120°.



**Planar imaging**

**Volumetric imaging**

**Functional imaging**

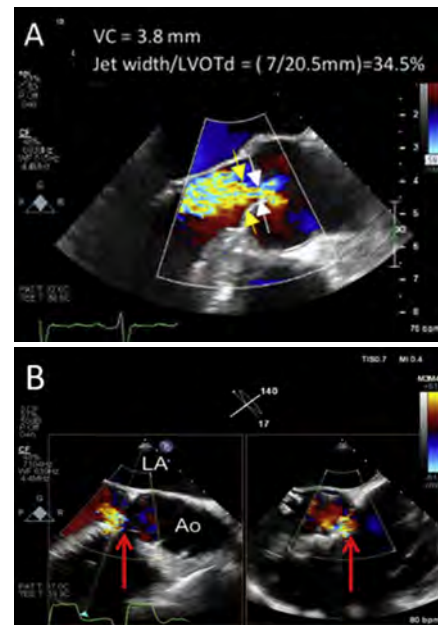
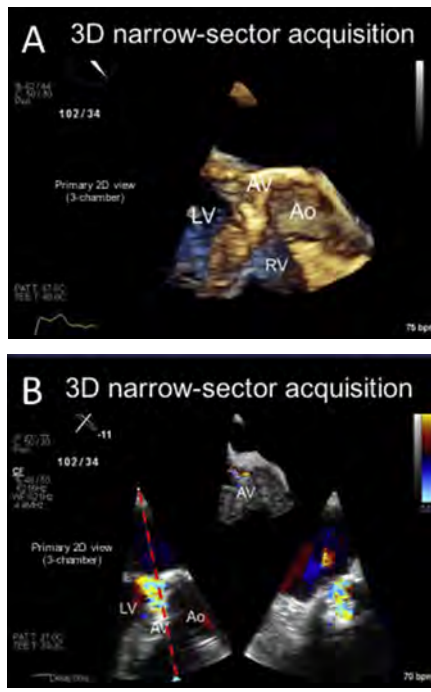
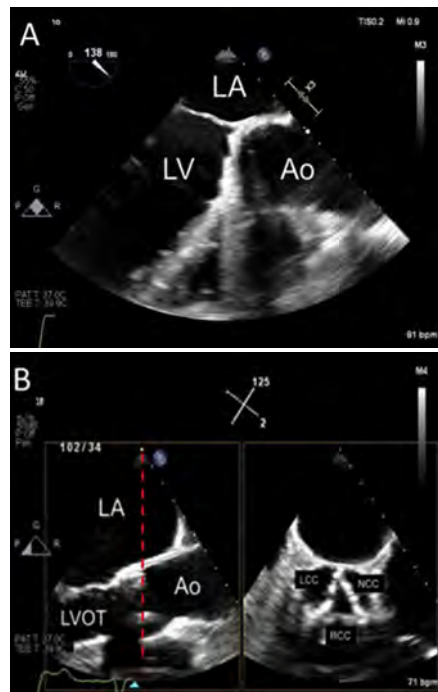
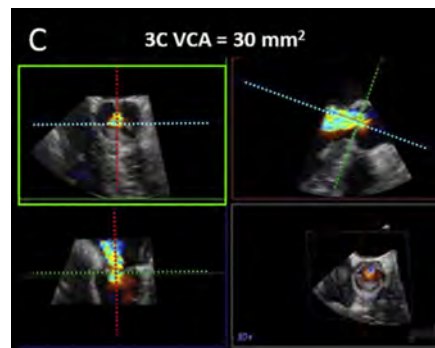


**Table 3** (Continued)

**Imaging level: ME AV long-axis view 110°–140°**



- A. AV long-axis view used to measure LVOT diameter.
- B. Biplane image from primary ME long-axis view with orthogonal image at mid AV leaflets demonstrating orthogonal tricuspid AV thickened leaflets.

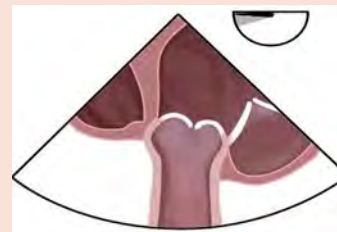
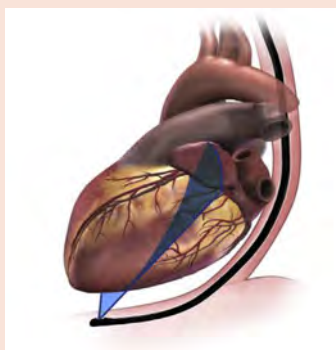
- A. Three-dimensional narrow-sector view demonstrating AV anatomy. The narrow sector in the elevation plane (into screen) translates to a direct visualization of the primary three-chamber 2D plane in 3D.
- B. Three-dimensional color Doppler narrow-sector view in biplane mode, centered on paravalvular jet.

- A. Aortic long-axis view demonstrating central AR jet VC (white arrows) measured at narrowest color Doppler convergence. Color jet width in LVOT (yellow arrows) is measured just apical to the AV in the LVOT.
- B. Aortic long-axis view with advancement/anteflexion with tilt plane on AR jet to elucidate the paravalvular leak origin on orthogonal view (red arrow).
- C. Three-dimensional VCA measurement on multiplanar reconstruction. The VC is localized in two long-axis planes (upper right and lower left) and measured by planimetry in the SAX view (upper left, green box).

**Imaging level: DT view 0°–30°**

Acquisition protocol

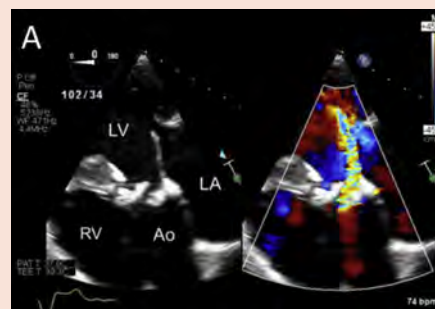
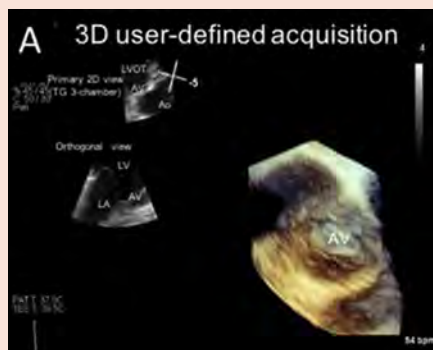
- From the DT level at 0°–30°, anteflexion brings LVOT/AV into view.
- Additional probe manipulations to optimize ultrasound beam alignment (in combination with anteflexion): counterclockwise rotation, and/or left flexion.



**Planar imaging**

**Volumetric imaging**

**Functional imaging**



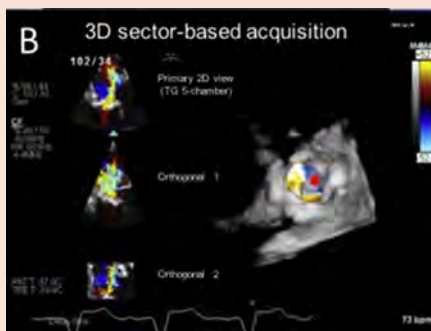
(Continued)

Table 3 (Continued)

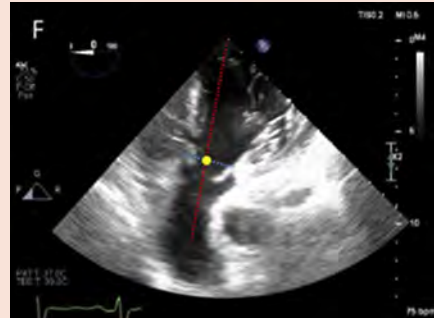
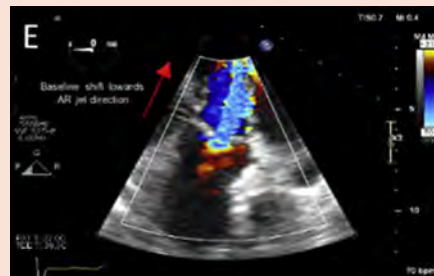
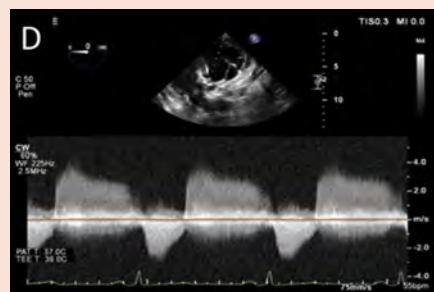
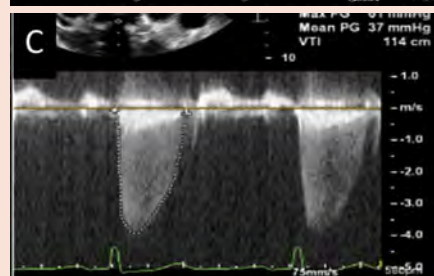
Planar imaging



Volumetric imaging

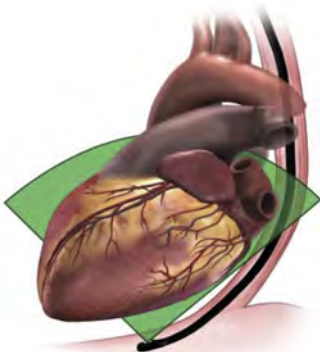
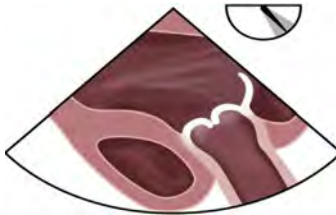


Functional imaging



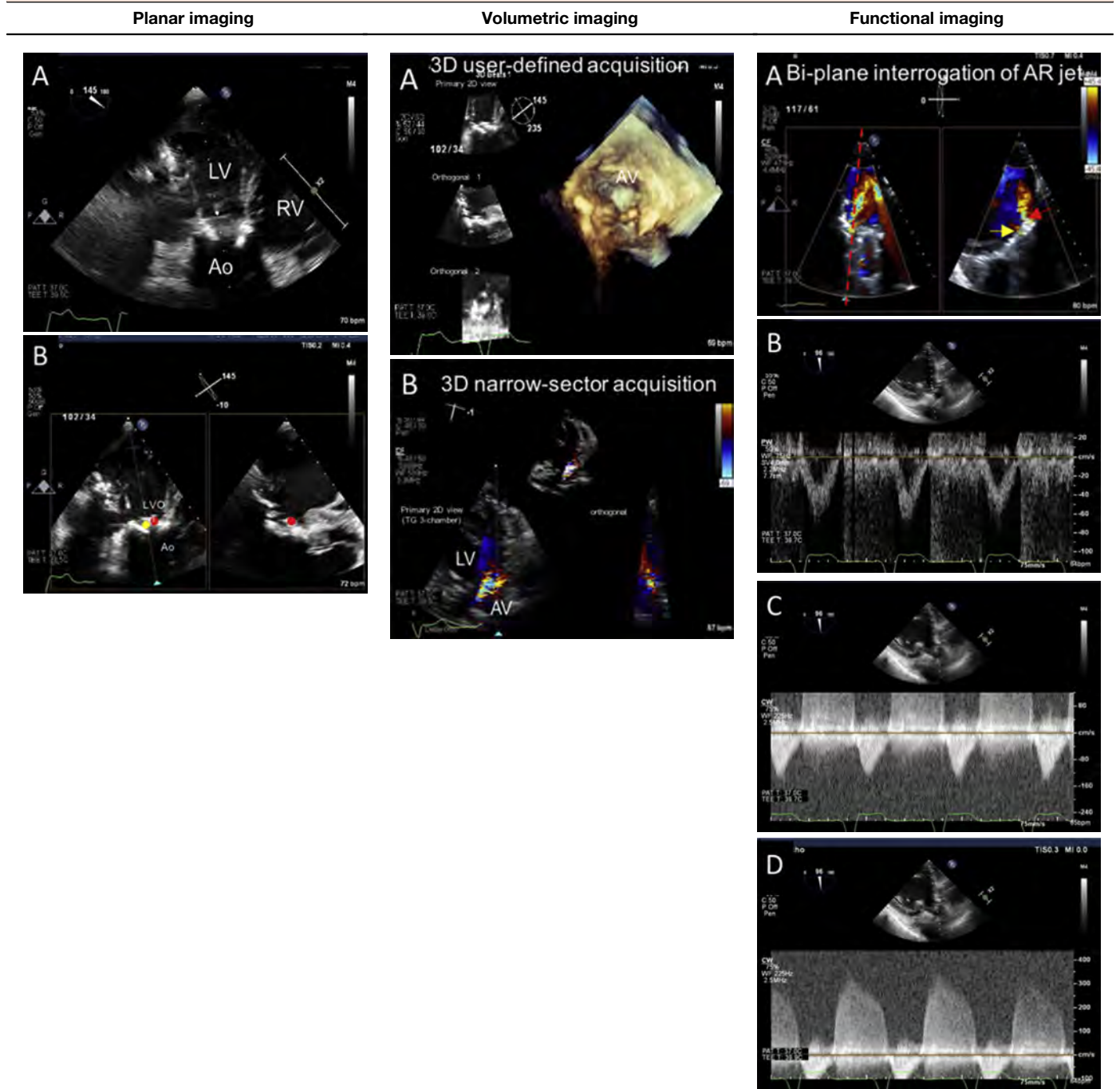
(Continued)

Table 3 (Continued)

Planar imaging	Volumetric imaging	Functional imaging
<p>A. The TG five-chamber view to demonstrates the ventricular aspect of the aortic leaflets and aligns the LVOT and AV for spectral Doppler.</p> <p>B. Two-dimensional zoomed image from the TG five-chamber view demonstrating flail leaflet anatomy (flail leaflet shown with <i>red circle</i>, flail gap shown with <i>yellow circle</i>).</p>	<p>A. Three-dimensional user-defined volume in biplane mode from a primary TG five-chamber view to ensure capture of entire valve for assessment of leaflet anatomy. The 3D rendering is en face view of the AV from the LVOT.</p> <p>B. Three-dimensional sector-based color Doppler acquisition on triplane view from a primary TG five-chamber view to ensure capture of regurgitant jet VC within the volume. The flail leaflet is shown in the 3D rendering (<i>red circle</i>).</p>	 <p>A. Color-compare image from TG five-chamber view showing a flail aortic leaflet with expected AR jet direction.</p> <p>B. PW Doppler of LVOT from TG five-chamber view used to trace LVOT VTI.</p> <p>C. CW Doppler of AV from TG five-chamber view used to assess AV gradients and AV VTI for EOA calculations.</p> <p>D. CW Doppler of AR VTI from TG five-chamber view for PHT, RVol, EROA calculations.</p> <p>E. AR PISA from TG five-chamber with baseline shifted in jet direction (toward LVOT) for hemisphere visualization.</p> <p>F. For pure AR LVOT SV calculation, PW Doppler sample volume (<i>yellow circle</i>) should be placed at the level of the AV hinge points (<i>blue dotted line</i>).</p> <p>G. For AS LVOT stroke volume calculation, PW Doppler sample volume (<i>yellow circle</i>) should be placed slightly apical to the level of the AV hinge points (<i>blue dotted line</i>) to avoid the flow acceleration zone.</p>
<b>Imaging level: DT view 110°–120°</b>		
Acquisition protocol		
<ul style="list-style-type: none"> <li>From the DT level, withdrawing the probe to the TG level with mechanical rotation of 110°–120° should generate a TG long-axis view of the LVOT/AV. Additional flexion may be needed and/or further advancement (to DT level) may improve ultrasound beam alignment.</li> <li>Note: TG 110°–120° view is an alternative to the TG 0°–30° view. Similar information can be obtained from both views, however, the insonation angle may be slightly different, and could result in better alignment with transaortic flow.</li> </ul>		
		

(Continued)

Table 3 (Continued)



(Continued)

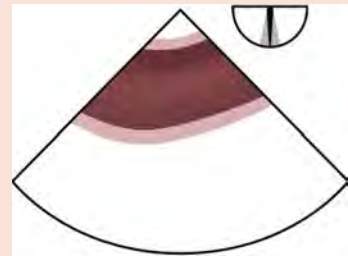
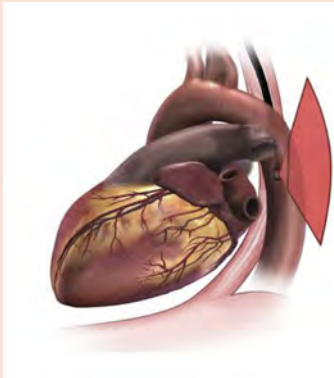
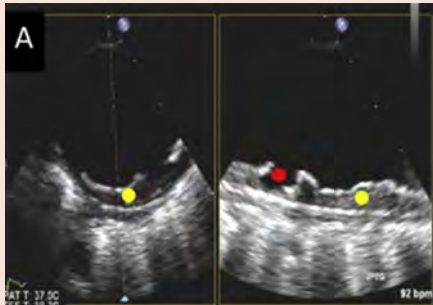
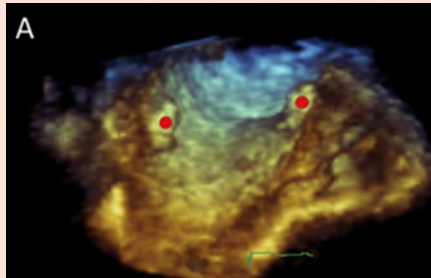
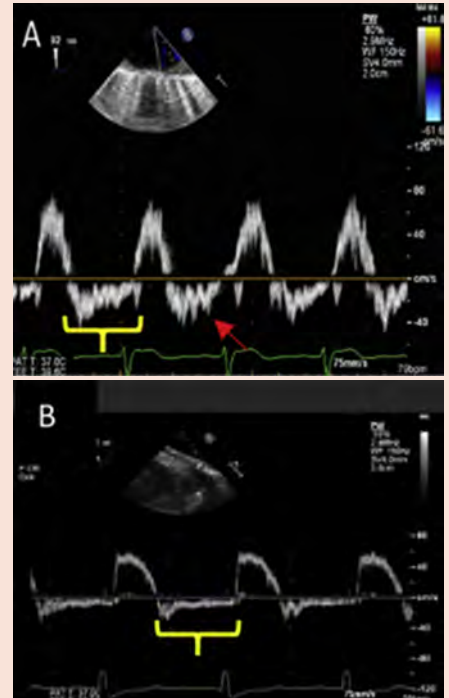
**Table 3** (Continued)**Imaging level: DT view 110°–120°**

- |  |   |   |
|--|---|---|
| <p>A. TG three-chamber view to demonstrate ventricular aspect of aortic leaflets and align LVOT and AV for spectral Doppler.</p> <p>B. Biplane imaging demonstrating prosthetic flail leaflet (<i>red circles</i>) and gap (<i>yellow circle</i>).</p> | <p>A. Three-dimensional user-defined volume in biplane mode from a primary TG three-chamber view to ensure capture of entire valve for assessment of leaflet anatomy. The 3D rendering is an en face view of the AV from the LVOT.</p> <p>B. Three-dimensional narrow-sector-based color Doppler acquisition on biplane view to ensure capture of the AR jet.</p> | <p>A. Biplane image from TG three-chamber view showing interrogation of prosthetic valve AR jets of unclear origin. The orthogonal view clarifies the location of larger paravalvular jet (<i>red arrow</i>) and smaller central jet (<i>yellow arrow</i>).</p> <p>B. Tracing of PW Doppler waveform of LVOT used to determine LVOT VTI.</p> <p>C. CW Doppler of AV from TG three-chamber view used to assess AV gradients.</p> <p>D. CW Doppler of AR VTI from TG three-chamber view for PHT, RVol, EROA calculations.</p> |
|--|---|---|

**Imaging level: UE, ME, and TG views 0° and 80°–100°**

## Acquisition protocol

- Counterclockwise rotation from the heart to the posteriorly positioned aorta, which can be imaged in SAX (0° mechanical rotation) or long axis (80°–100° mechanical rotation) views.
- To align the ultrasound beam with flow for Doppler assessment, ante flexion or retro flexion is frequently needed.

**Planar imaging****Volumetric imaging****Functional imaging**

(Continued)

**Table 3** (Continued)

A. Biplane image of the aortic arch demonstrating severe atheroma ( <i>yellow circles</i> ) with ulceration ( <i>red circle</i> ).	A. Three-dimensional view of the lesser curvature of the aortic arch demonstrating atheroma ( <i>red circles</i> ).	A. Anteflexion or retroflexion of the probe allows alignment of aortic flow with the ultrasound beam. PW Doppler sample volume at the aortic arch shows holodiastolic flow reversal ( <i>yellow bracket</i> ) with high end-diastolic velocity > 20 cm/sec ( <i>red arrow</i> ) suggestive of at least moderate AR. This finding is less specific with advanced age or concomitant disease that reduces left ventricular or aortic compliance. B. PW Doppler in the abdominal descending aorta demonstrating holodiastolic flow reversal ( <i>yellow bracket</i> ) is specific for severe AR.
--	---	--

Ao, Aorta; EOA, effective orifice area; EROA, effective regurgitant orifice area; LA, left atrium; LCC, left coronary cusp; LV, left ventricle; LVOT, left ventricular outflow tract; NCC, noncoronary cusp; PW, pulsed wave; RCC, right coronary cusp; RA, right atrium; RV, right ventricle; RVol, regurgitant volume; VC, vena contracta; VCA, vena contracta area; VTI, velocity-time integral.

distinct leaflet segments. The modified scheme divides the large middle segments into lateral (A2L and P2L) and medial (A2M and P2M) halves, respecting the separate chordal attachments of the leaflets and the midline chordal-free zone. Thus, A1, P1, A2L, and P2L have chordae arising from the anterolateral papillary muscle, whereas A3, P3, A2M, and P2M have chordae from the posteromedial papillary muscle. Marginal or primary chordae insert on the leaflet free margins and help prevent marginal prolapse, whereas secondary or “strut” chordae insert on the ventricular surface of the leaflets, preventing billowing while reducing tension on the leaflet tissues (Figure 13D). The papillary muscles arise from a network of trabeculations (Figures 13E and 13F) of the compacted myocardium.

**2. General Imaging Protocol for the MV (Table 4). ME Views.** Manipulation of the TEE probe is often required to align the mitral annulus perpendicular to the ultrasound beam (Figure 14). The ME four-chamber view is usually acquired with a mechanical rotation of 0° to 20°. Withdrawing the probe (and/or using anteflexion) will bring the lateral commissure into view, while advancing the probe (and/or further retroflexion) focuses on the medial structures. The ME mitral commissural view (50°–70°) and the ME long-axis view (120°–140°) are key views to image the mitral leaflet coaptation zone. The commissural view should aim for symmetric display of papillary muscle heads and chords. Clockwise and counterclockwise rotation of the TEE probe moves the imaging plane anteriorly and posteriorly, respectively. The LAA offers a clear landmark for the anterolateral commissure and the A1/P1 scallops, whereas the coronary sinus is adjacent to the posteromedial commissure and the A3/P3 scallops. Generating the 3D en face view of the MV is shown in Figure 15. Other essential components of a comprehensive examination are shown in Table 4.

**TG Views.** ME 3D imaging of the MV has replaced TG imaging for identification of leaflet pathology and location of the regurgitant orifice. However, TG level of imaging can still be used to confirm MV pathology (with and without color Doppler), visualize the subvalvular apparatus (chordae and papillary muscle), perform CW Doppler measurements (particularly with eccentric jets), and quantify stroke volume.

Although several qualitative and semiquantitative measurements can be obtained with TEE, quantitative measures of mitral regurgitation (MR) severity should be performed. These quantitative methods are shown in Figure 16. Biplane measurements of the mitral annulus may result in the most accurate calculation of annular area, and thus regurgitant volume,<sup>38,39</sup> however, using the four-chamber mitral annular diameter in a circular formula has been validated as an alternative to biplane imaging or 3D planimetry of the annulus.<sup>38</sup>

**3. Rheumatic Mitral Stenosis.** Mitral stenosis (MS) is commonly caused by rheumatic heart disease, although degenerative nonrheumatic calcification that originates in the annulus and extends to a variable degree onto the leaflets may also occasionally cause hemodynamically significant MS. The distinction between the two etiologies is important, because rheumatic MS may be successfully treated by percutaneous mitral balloon commissurotomy, whereas catheter-based options for mitral annular calcification (MAC) are largely limited to anecdotal experience, with percutaneous balloon valvuloplasty used as palliation or bridge to a definitive procedure and experimental placement of balloon-expandable valves (valve-in-MAC). Valve-in-MAC procedures<sup>40</sup> can be performed percutaneously<sup>41</sup> or with open thoracotomy.<sup>42</sup>

Rheumatic inflammation of leaflets and chords with subsequent healing inevitably leads to deformation of the MV (Figure 17). The main pathomorphological changes are as follows:

- thickening, retraction, and rigidity of leaflets (Figures 17A–17C);
- fusion of both commissures and folds between scallops, resulting in a “fish mouth” orifice appearance (Figure 17D);
- fusion and shortening of chordae tendineae with elimination of interchordal spaces, contributing to diastolic “doming” of the anterior mitral leaflet, immobilization of the posterior leaflet, and subvalvular thickening; and
- calcium deposition.

**Valve Morphology and Severity of MS.** Preprocedural imaging of the MV before balloon commissurotomy includes thorough assessment of MV anatomy and function (including severity of MR) as well as left atrial and right atrial size and morphology (e.g., to exclude thrombus) and severity of pulmonary hypertension. Rate and rhythm

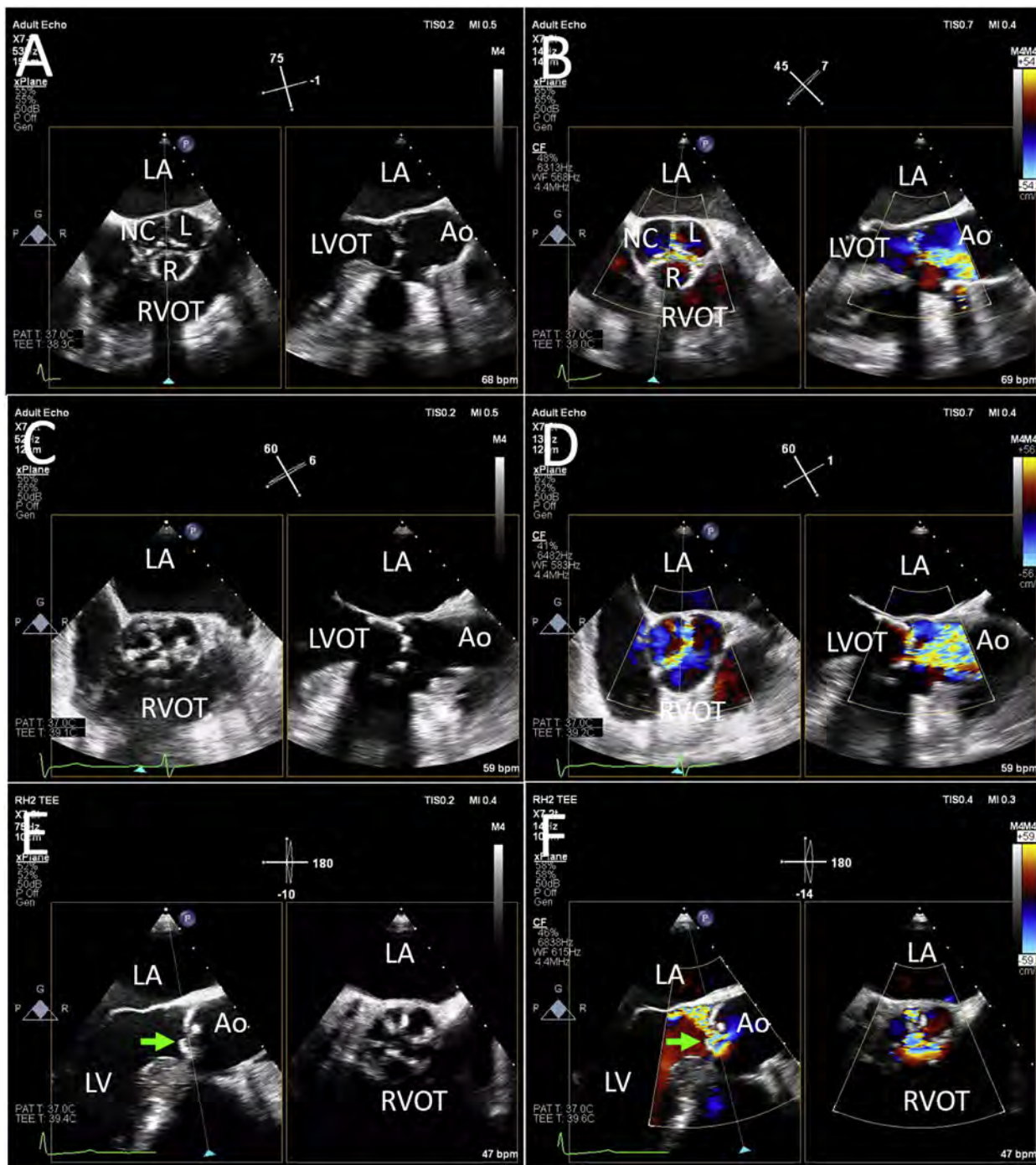


**Figure 6** Imaging of the AV and aortic root. Simultaneous multiplane imaging of the AV and aortic root are shown. In the setting of bulky calcification, distinguishing the number of cusps may be difficult, but a trileaflet AV (**A**) has three commissures seen on color Doppler of systolic SAX images (**B**), whereas a bicuspid valve (**C**, **D**) will only have two commissures. The etiology of AR should also be assessed. In panel **E** there is a flail right coronary cusp (green arrow) causing an eccentric regurgitant jet (**F**, green arrow). Ao, Aorta; L, left coronary cusp; LA, left atrium; NC, noncoronary cusp; R, right coronary cusp.

should be included when reporting mean pressure gradients. In the setting of atrial fibrillation, ASE guidelines recommend averaging values from five beats with cycle lengths that best represent the average underlying heart rate.<sup>43</sup> Leaflet thickening and calcification must be noted in each view. TG views may better display chordal abnormalities, particularly when there is acoustic shadowing due to valvular and/or annular calcification.

Although MV area is most commonly measured using direct planimetry, areas have been reported or calculated using the pressure half-time, PISA, and quantitative Doppler approaches. Although the latter two techniques are rarely used, they may be helpful in patients in whom planimetry and pressure half-time approaches are suboptimal or yield discordant measures of severity.<sup>43</sup> The two main advantages of 3D over 2D imaging are a more accurate assessment of

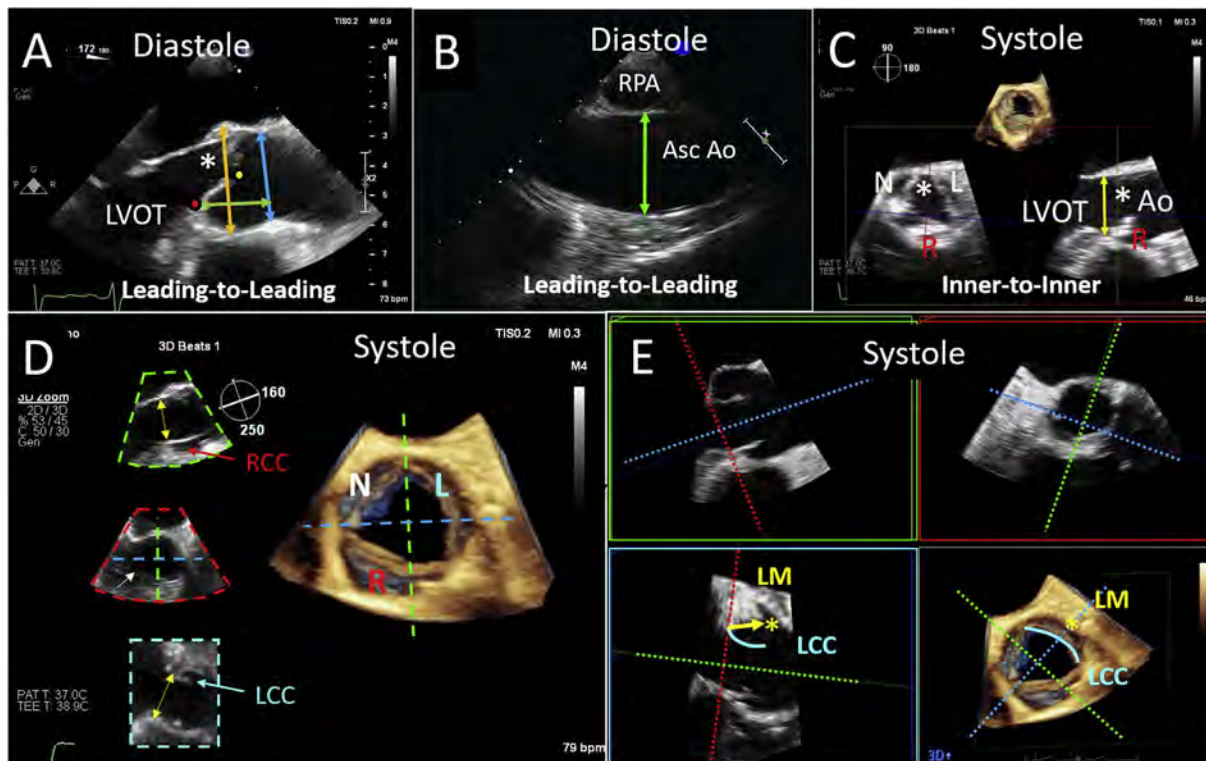


**Figure 7** ME imaging of the AV and root. The ME long-axis view of the aorta in diastole (**A**) allows measurements of the aorta using the leading edge-to-leading edge technique: sinuses of Valsalva (orange arrow), sinotubular junction (blue arrow), and sinus height (green arrow). The nadir of the right coronary cusp (RCC) is seen anteriorly (red dot) and defines the location of the annular plane. A central coaptation gap can also be appreciated (yellow dot). Withdrawing the probe and reducing the angle results in a UE view, from which the ascending aortic diameter can be measured (green arrow, **B**). Typically, when the midline of the aorta is bisected (**C**), the interleaflet trigone between the left coronary cusp (L or LCC) and noncoronary cusp (N or NCC) is seen posteriorly (white asterisk, **A** and **C**); thus, in systole the anterior right cusp (R) is often visualized but no posterior leaflet is seen (bottom right image). The aortic annulus is measured from the inner to inner borders. Multiplanar imaging during 3D acquisition (**D**) is used to check the quality of the three orthogonal 2D images. In these systolic views, one can clearly appreciate the annular plane (yellow double-headed arrows) in the long-axis view (green sector), SAX view (red sector), and coronal plane (blue sector). A small area of acoustic shadowing (white arrow, red sector) is seen in the SAX view. **Panel E** demonstrates alignment of the left main (LM) coronary artery ostium (yellow asterisk) in the coronal plane (blue box and 3D-rendered view). The LM height or distance from the virtual annulus plane to the coronary ostium (yellow arrow) is measured from the coronal plane (blue box). The left coronary leaflet (LCC; blue curved line) is seen on the 3D-rendered view and the coronal plane (blue box), and its length is measured from the 2D image. An LCC length that is <2 to 3 mm shorter than the LM height, or an LM height <10 to 11 mm (particularly in the setting of a short root), poses a risk for possible coronary artery obstruction with transcatheter valve implantation. Ao, Aorta; Asc Ao, ascending aorta; LA, left atrium; LV, left ventricle; RPA, right PA.

commissural fusion and a more precise measurement of valve area (Figure 4).<sup>44,45</sup>

**Additional Imaging Requirements.** Assessment of baseline MR is important because balloon commissurotomy may create or increase MR. The procedure is contraindicated when baseline MR is moderate or greater. The multiparametric, integrative ASE approach is recommended for assessing MR severity.<sup>6</sup> However, because MR is afterload and preload dependent, changes in loading conditions (e.g., blood pressure increases with anxiety or decreases with conscious sedation or general anesthesia) should be considered when making this assessment.

Both the right atrial appendage and LAA should be thoroughly imaged to exclude intracavitary thrombus. The use of simultaneous biplane imaging may be helpful but is associated with lower temporal and spatial resolution. Ultrasound enhancing agents may be used to

distinguish spontaneous contrast from thrombus. Because balloon commissurotomy is performed through a transseptal approach, it is also important to assess the interatrial septum (IAS) for features that would affect the ease of transseptal puncture, such as a highly mobile fossa ovalis or severe lipomatous hypertrophy. PA systolic pressure should be estimated as previously described.<sup>46</sup>

**4. Degenerative MS.** MAC is common and seen on echocardiography in >40% of patients >65 years of age.<sup>47</sup> Calcification can variably extend onto the leaflets, resulting in both MS and/or MR (Figures 18A–18D).<sup>48</sup> Because of the intrinsic limitations of echocardiography in the setting of calcified tissue (acoustic shadowing, blooming artifacts, and limited tissue characterization), preprocedural planning requires CT performed at experienced sites that are able to determine the extent and location of calcification, size the annulus<sup>49</sup> (Figure 18E), and predict the area of the neo-LVOT using “virtual valve” imaging algorithms.<sup>50</sup>

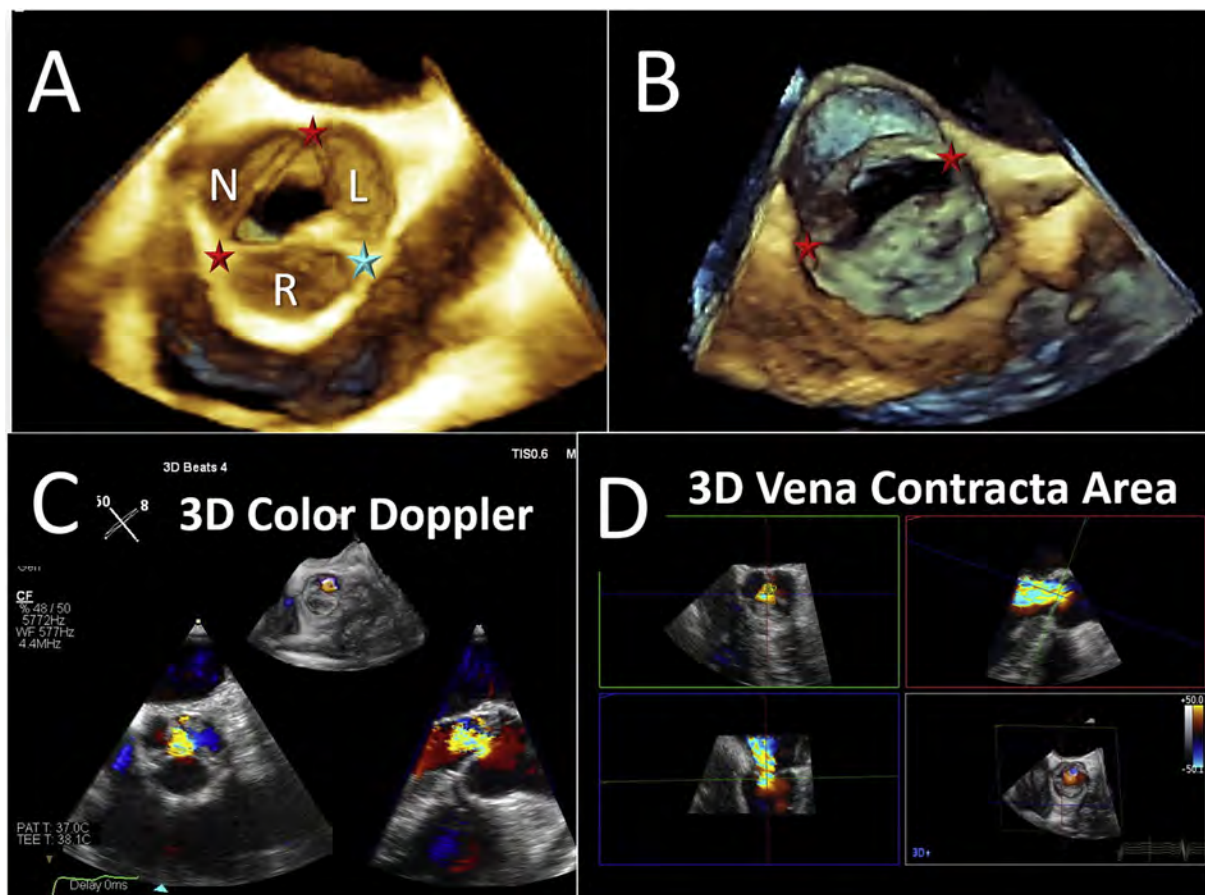


**Figure 8** Three-dimensional bicuspid AV pathology. In the 3D-rendered images of a bicuspid AV, panel **A** has two commissures (red stars) with a raphe (blue star), whereas the valve in panel **B** has no raphe. Panel **C** shows a multibeat 3D color Doppler volume data set that can be used to quantify the regurgitant vena contracta area with multiplanar reconstruction (**D**). *L*, Left coronary sinus; *N*, non-coronary sinus; *R*, right coronary sinus.

**Valve Morphology and Severity of MS.** Evaluation of the severity and extent of MAC is essential for determining the appropriateness and type of transcatheter or surgical treatment for significant, symptomatic disease. Although TTE is typically used with a variety of MAC grading criteria,<sup>51-53</sup> preprocedural TEE imaging is essential for confirming the etiology and severity of MS. The standard methods of quantifying MS severity, including the pressure half-time method, PISA, the continuity equation, and planimetry, lack robust validation in this patient population. Two-dimensional planimetry is particularly problematic in the setting of an irregular calcific orifice, as well as nonplanar and poorly defined location of flow limitation. Three-dimensional TEE studies have suggested that flow limitation typically occurs at the annulus (Figure 18C) rather than at the leaflet tips.<sup>54</sup>

Other important morphologic characteristics to be assessed include the following:

1. Distribution of calcification, as valves will seat best when the calcium is relatively uniform and circumferential. The distribution of calcification is best displayed with the 3D surgeon's view acquired from a ME window (Figure 18B).
2. Shape of the annulus, with marked eccentricity predisposing to postprocedural paravalvular regurgitation. This may be assessed with echocardiography, although quantitation is best performed with CT.
3. Angle between the mitral annulus and LVOT or AV annulus (mitral-aortic angle; Figure 18F), resting or provokable LVOT obstruction, and presence

of septal hypertrophy. The echocardiographic approach to assessing the mitral inflow-to-LV outflow angle mimics that used for CT and is best performed with multiplanar reconstruction on 3D volume data sets. These features help predict the likelihood that the valve will obstruct the LVOT, in which case alcohol septal ablation to reduce septal thickening may be necessary before a valve-in-MAC procedure in order to create enough space for the new valve.<sup>55</sup> Alternative procedures such as intentional laceration of the anterior mitral valve leaflet to prevent LVOT obstruction (LAMPOON) may also be considered.<sup>56,57</sup>

4. Severity of concomitant MR.

**5. Primary MR.** Primary MR is defined by abnormalities in the leaflets, chords, annulus, and/or papillary muscles.<sup>4,58</sup> Whereas both Carpentier type I (normal leaflet motion with annular dilatation such as with atrial fibrillation or endocarditis) and Carpentier type IIIa (restricted leaflet motion during diastole and systole such as with rheumatic disease, collagen vascular disease, and MAC) disease may cause regurgitation, the most common cause of primary MR is Carpentier type II disease associated with excess leaflet motion and/or leaflet destruction (Figure 19).<sup>58</sup> Excess leaflet motion is principally caused by one of two fundamentally different pathoanatomies: chordal lengthening and chordal rupture. These may coexist as a spectrum, collectively termed degenerative MR.<sup>59</sup> Although an individual patient may have more than one mechanism, whenever possible the relative contributions of these mechanisms should be

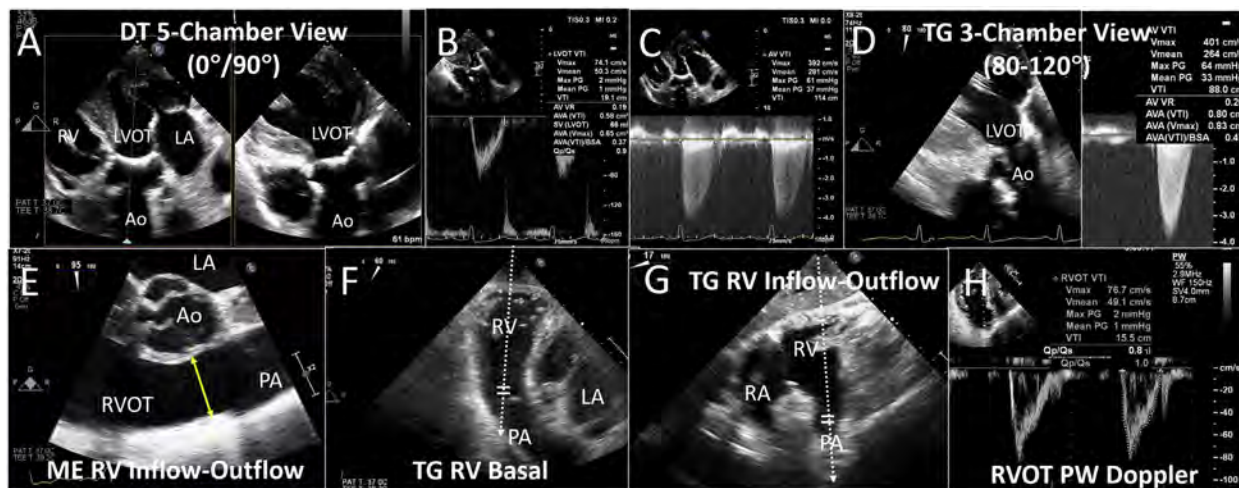


**Figure 9** Quantifying stroke volume (SV) and aortic valve area (AVA). The deep transgastric (DT) five-chamber view (**A**) aligns the transaortic flow with the ultrasound beam, allowing pulsed-wave (PW) Doppler acquisition of the left ventricular outflow tract (LVOT) spectral profile (**B**) and continuous wave (CW) Doppler acquisition across the AV (**C**). Doppler from the transgastric (TG) view at 80° to 120° (**D**) should also be attempted, as this imaging plane typically will align the insonation beam with jets that are directed more anteriorly or toward the right. Calculation of the right ventricular outflow tract (RVOT) SV may be necessary to quantify aortic regurgitation (AR) and requires measurement of the RVOT diameter, best imaged from the mid-esophageal (ME) level at 70° to 90° (**E**). Doppler of the RVOT should be obtained from the TG level by centering the RV in the sector and then anteflexing and mechanically rotating to about 60° (TG RV basal view; **F**). Alternatively, a TG RV inflow-outflow view is acquired by right flexion and anteflexion at about 0° to 20° (**G**) or an upper esophageal (UE) view (not shown) can be used if TG views are suboptimal. The PW Doppler sample volume should be at the annular level in systole (**H**) to acquire the spectral profile used in calculation of the RVOT SV. Ao, Aorta; BSA, body surface area; LA, left atrium; PG, pressure gradient; Qp/Qs, ratio of pulmonary flow to systemic flow; RV, right ventricle; Vmax, maximum velocity; Vmean, mean velocity; VR, velocity ratio; VTI, velocity-time integral.

identified. The more precise Carpentier classification system is strongly encouraged because it is superior to the simpler dichotomous primary versus secondary (functional) classification and is particularly helpful in transcatheter mitral procedures.

**Valve Morphology and Severity of Regurgitation.** Myxomatous degeneration and fibroelastic deficiency have different leaflet pathologies, each of which can be associated with severe degenerative MR. The former is typically associated with markedly thickened and redundant leaflets, frequently with bileaflet prolapse. The latter is associated with thinning and atrophy of the leaflet and chordal tissues, often with prolapse or flail of an isolated segment. For both morphologic types, it is important to localize the regurgitation site.

**Mitral Leaflets and Chordae.** Prolapse, by definition, is present when leaflet tissue extends  $\geq 2$  mm above the high points of the mitral annulus in systole. Imaging should clearly identify the timing, location (e.g., leaflet and scallop), and extent (e.g., end-systolic flail width and gap) of the abnormal leaflet motion. In addition, deep indentations/folds or clefts and their location relative to jet origin should be identified, as leaflet grasp may be difficult in the presence of these anatomic abnormalities. Three-dimensional en face imaging of the MV has increased our recognition of “gaps” in the leaflet tissue, but there is significant variability in the terminology used for these indentations. One study defined indentations that reach the annulus boundary as a cleft of the anterior leaflet but as a profound indentation of the posterior leaflet.<sup>60</sup> It is necessary to distinguish morphologically a cleft in an otherwise normally structured MV from the congenital cleft MV, often associated with the trifoliate left compo-

nent of a common atrioventricular valve in patients with an atrioventricular canal septal defect.<sup>61</sup>

The transcatheter edge-to-edge repair device has a class 2A recommendation for high-risk patients with appropriate valve morphology, and assessment of morphology and feasibility of both transcatheter and surgical repair using TEE imaging is a class 1A recommendation in current guidelines.<sup>4</sup> Morphology and feasibility of repair are comprehensively discussed in the updated expert consensus decision pathway document.<sup>62</sup>

**Mitral Annulus.** Although annular repair devices currently are limited to the treatment of secondary MR, transcatheter MV replacement has been performed in primary MR.<sup>63</sup> Thus, a full characterization of the annulus is important, including motion, the severity of calcification, dimensions (commissural and anteroposterior), and area using both 2D and 3D imaging. Mitral annular disjunction is a variant of degenerative MR in which a wide separation between the atrial-MV junction and the basal LV myocardium is noted. It is important to characterize this variant of myxomatous degeneration, as devices that rely on anchoring at the mitral annulus must redefine the most appropriate anchor zone (i.e., leaflet hinge or basal myocardium). Significant MAC at the site of device anchoring may also be a relative exclusion criterion for device placement.

**Additional Imaging Requirements.** As with MS, preprocedural planning for devices using a transeptal approach should include a comprehensive evaluation of the IAS for ideal transeptal puncture site, presence of an interatrial shunt, or other structural abnormalities (e.g., prominent Eustachian valve or Chiari network).

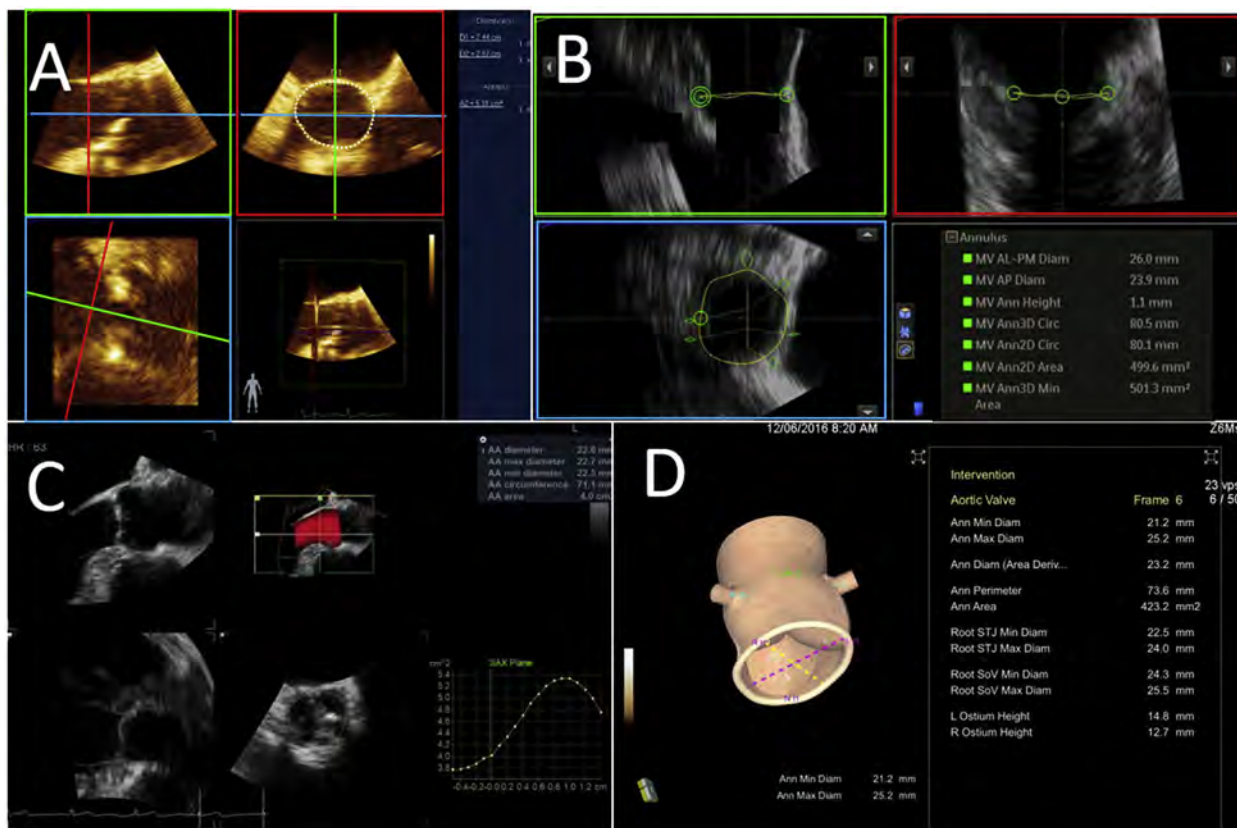


**Figure 10** Aortic annular (AA) measurements. A user-defined 3D zoom acquisition is acquired after optimizing the frame rate by limiting the size of the volume. Direct planimetry (**A**) is the most common method to measure annular area and perimeter, but acoustic noise or shadowing (typically from the calcified cusps) may result in inaccuracies. Indirect methods have been validated using CT (**B**), which allows the use of orthogonal long-axis planes to define the points around the annulus. Multiple automated software packages (**C**, **D**) have been developed but lack validation against other modalities. *AL*, Anterolateral; *Ann*, annular; *AP*, anteroposterior; *Circ*, circumference; *Diam*, diameter; *PM*, posteromedial; *SoV*, sinuses of Valsalva; *STJ*, sinotubular junction.

**6. Secondary (Functional) MR.** In contrast to primary MR, secondary MR is associated with intrinsically normal leaflets that fail to coapt in the setting of a remodeled and dysfunctional ventricle and/or atrium. Assessment of this entity entails imaging protocols that are similar to those of primary MR.

**Morphology and Severity of MR.** There are two distinct morphologic subtypes of functional MR: annular dilation with normal leaflet motion (type I) and the more common restricted systolic motion with LV remodeling or dysfunction (type IIIb; [Figure 19](#)). Type I disease typically occurs in the setting of atrial fibrillation or heart failure with preserved ejection fraction, and MR is due to isolated annular dilation, insufficient leaflet growth, and impaired annular dynamics.<sup>64,65</sup> The hallmark of type IIIb functional MR is apically tethered leaflets due to an imbalance between tethering and closure forces. Annular dilation may also be present.<sup>66</sup> The term *ischemic MR* is applied to functional MR when the underlying cause of LV abnormalities is coronary disease. The morphologic changes associated with ischemic and nonischemic functional MR are distinct, but both are associated with ventricular enlargement with lateral displacement of the papillary muscles.<sup>58,67</sup> This results in the point of leaflet contact (attempted coaptation) being displaced below the MV annulus. The chordal apparatus appears stretched, and individual chords may be under significant tension.

Preprocedural imaging for transcatheter repair compared with replacement in patients with functional MR varies depending on the device and its anchoring mechanism. The size of the coaptation gap and resulting MR jet ([Figure 20A](#)) from 2D imaging or 3D focused volumes ([Figure 20B](#)) are important. Especially in secondary MR, the routine assessment of a single 2D measurement (e.g., vena contracta width or PISA radius) may underestimate the severity of MR in the setting of an elliptical regurgitant orifice.<sup>6</sup> Quantitative Doppler methods require expertise and multiple measurements. The systematic quantification of baseline 3D vena contracta area is recommended ([Figure 20C](#)).<sup>68</sup>

**Additional Imaging Requirements for Transcatheter Annular Repair or MV Replacement.** Whether a transeptal or transapical approach is used, the intracardiac access site must be fully assessed. The site of anchoring may also generate specific imaging requirements. In addition to 3D annular size (perimeter, diameters, and areas; [Figure 20D](#)), any anatomic structure that may interfere with device placement (e.g., chordae or papillary muscles) or stability (e.g., annular calcification) should be noted. With most current devices, there is a risk for LVOT obstruction depending on the vertical dimensions of the device, and the interaction with the native anatomy (i.e., the intact MV apparatus, interventricular

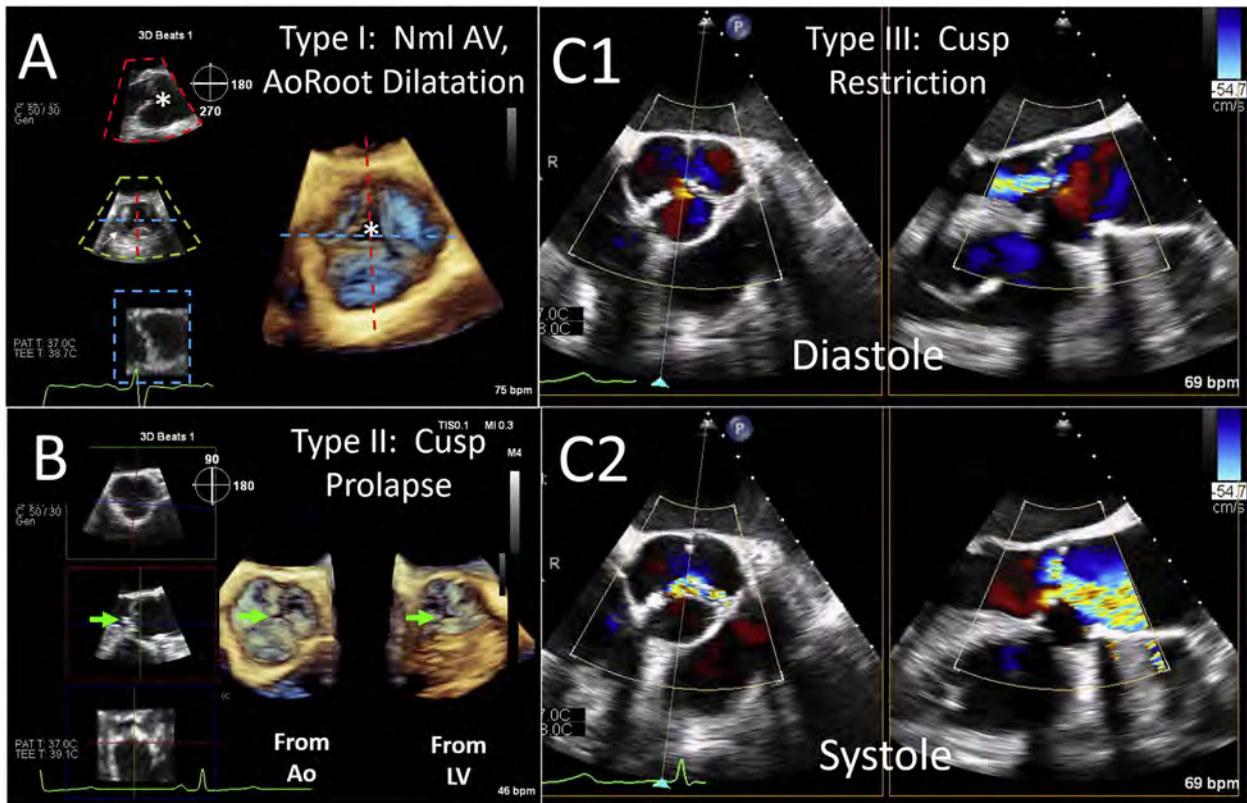


**Figure 11** AR valve morphology. AV/aortic root (AoRoot) structure and function with AR can be described as type I disease with normal (Nml) leaflet motion and dilatation of the aortic root (**A**, asterisk identifies the central leaflet malcoaptation); type II disease with excessive leaflet motion such as prolapse (**B**, green arrow indicates prolapse of the right coronary cusp); or type III disease due to leaflet restriction (**C1** and **C2**, leaflet restriction in both diastole and systole). Ao, Aorta; LV, left ventricle.

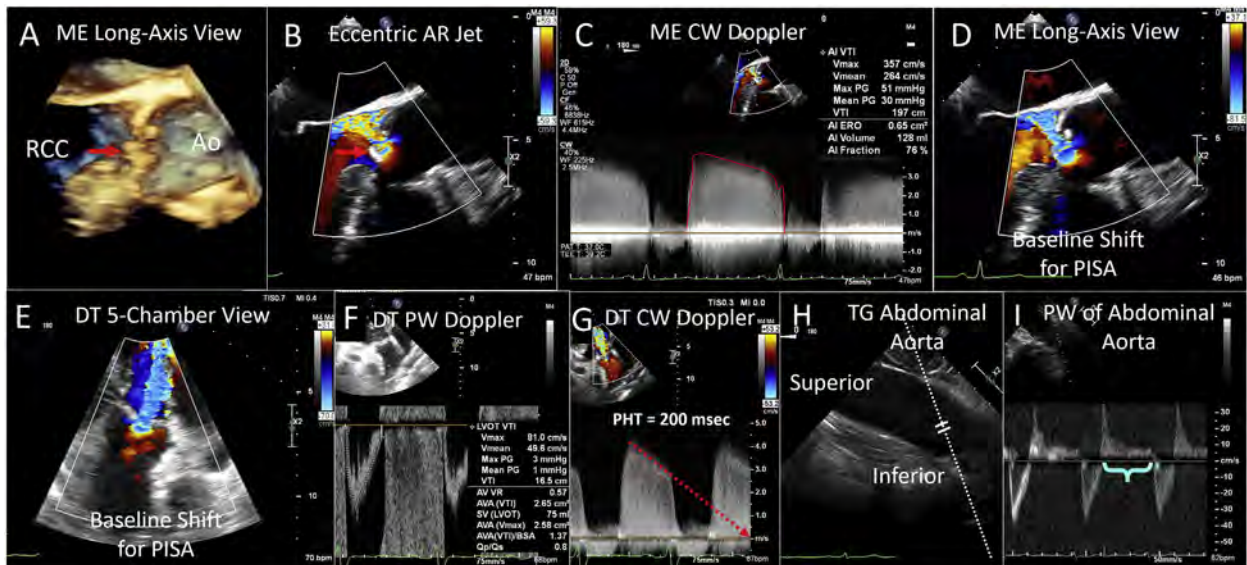


**Figure 12** AR quantification. Three-dimensional ME imaging (**A**) shows a flail right coronary cusp (red arrow), resulting in a posterior-directed regurgitant jet (**B**). Because the jet direction is aligned with the insonation beam, CW Doppler regurgitant spectral velocity-time integral (**C**) and PISA method for quantifying effective regurgitant orifice (ERO) area (**D**) is feasible. For more central regurgitant jets, TG views align the insonation beam with transaortic flow, and PISA (**E**), volumetric quantitation (**F**), and CW Doppler (**G**) can be performed. From the TG view, a counterclockwise turn of the TEE probe images the abdominal aorta, and with mild probe ante-flexion or retroflexion (**H**), flow is aligned for assessment of holodiastolic flow reversal with pulsed-wave Doppler (blue bracket, **I**). AI, Aortic insufficiency; Ao, aorta; AVA, AV area; BSA, body surface area; PG, pressure gradient; PHT, pressure half-time; Qp/Qs, ratio of pulmonary flow to systemic flow; RCC, right coronary cusp; SV, stroke volume; Vmax, maximum velocity; Vmean, mean velocity; VR, velocity ratio; VTI, velocity time integral.

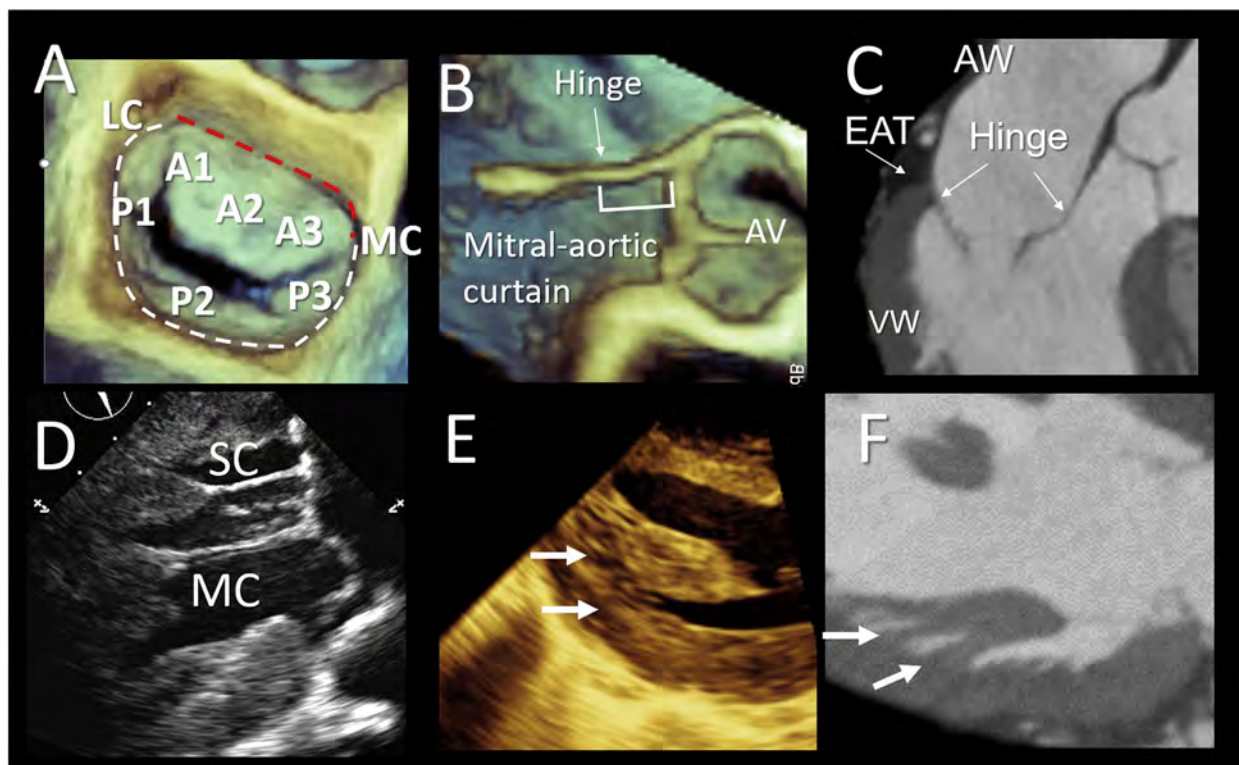


**Figure 13** Mitral annular anatomy. **(A)** Three-dimensional TEE image from the atrial perspective showing the hinge line of the posterior leaflet (*white dashed line*) and the hinge line of the anterior mitral leaflet (*red dashed line*). The scallops of the anterior (A1, A2, and A3) and posterior (P1, P2, and P3) leaflets are labeled, with the medial commissure (MC) and lateral commissure (LC). **(B)** Three-dimensional TEE long-axis view showing the mitral-aortic curtain (also known as the intervalvular fibrosa), a band of dense connective tissue between the hinge of the anterior mitral leaflet and the hinge of the aortic leaflet. **(C)** Computed tomographic image showing the hinge of anterior and posterior leaflets and the components of the posterior mitral annulus, namely, the ventricular wall (VW), the atrial wall (AW), the epicardial adipose tissue (EAT), and the hinge line of the posterior leaflet. **(D)** Two-dimensional TEE TG view, showing the strut chorda (SC) and the marginal chorda (MC). Panels **E** (3D TEE imaging) and **F** (CT) show the papillary muscles arising from a network of trabeculations (*white arrows*).

septum, and LVOT). To analyze the risk for LVOT obstruction with a transcatheter MV replacement, the length of the anterior leaflet (Figure 20E) and relationship between the LVOT and subvalvular or valvular structures (Figure 20F) should be evaluated in both diastole and systole.

**Assessment of MR.** Table 4 shows the components of a comprehensive TEE examination for MR quantitation; however, a comprehensive discussion of methods is in the ASE guideline for assessment of valvular regurgitation.<sup>6</sup> Use of each method must be guided by the anatomy of the regurgitant orifice: elliptical orifices typically seen with functional MR may lead to effective regurgitant orifice area underestimation by PISA, whereas other methods that assume holosystolic MR (vena contracta, color Doppler jet area, effective regurgitant orifice area by PISA) may overestimate the severity of MR in the setting of a late systolic regurgitant jet. An attempt should be made to interrogate all four pulmonary veins with pulsed-wave Doppler, with systolic flow reversal in at least one pulmonary vein being supportive of hemodynamically significant MR.

## E. Assessment of the PV

The PV is the most anteriorly and superiorly located valve, thus is challenging to visualize on TEE imaging because of interference from other structures (bronchus), patient intolerance of the TEE UE position, and its far-field location. Consequently, detailed imaging of the PV is most readily performed in sedated patients.<sup>1</sup> Intracardiac echocardiography may be an alternative imaging approach.

**1. Anatomy of the PV.** The PV is a trileaflet semilunar valve with thinner cusps and slightly larger diameter than the AV. It sits atop the muscular conus, which prevents fibrous continuity with the remaining cardiac valves. The leaflets are named for their anatomic position in space and in relation to the AV: right, left, and anterior or “opposite” (Figure 21). Notably, the PV is orthogonal to the plane of the AV when in its normal position, such that when one semilunar valve is visualized in cross-section, the other is in long axis.

Pathology in the form of pulmonic stenosis (PS) and/or pulmonic regurgitation (PR) is most commonly due to a congenital lesion and/or residual postoperative valve pathology. Less common causes are functional valve disease due to pulmonary hypertension or valve

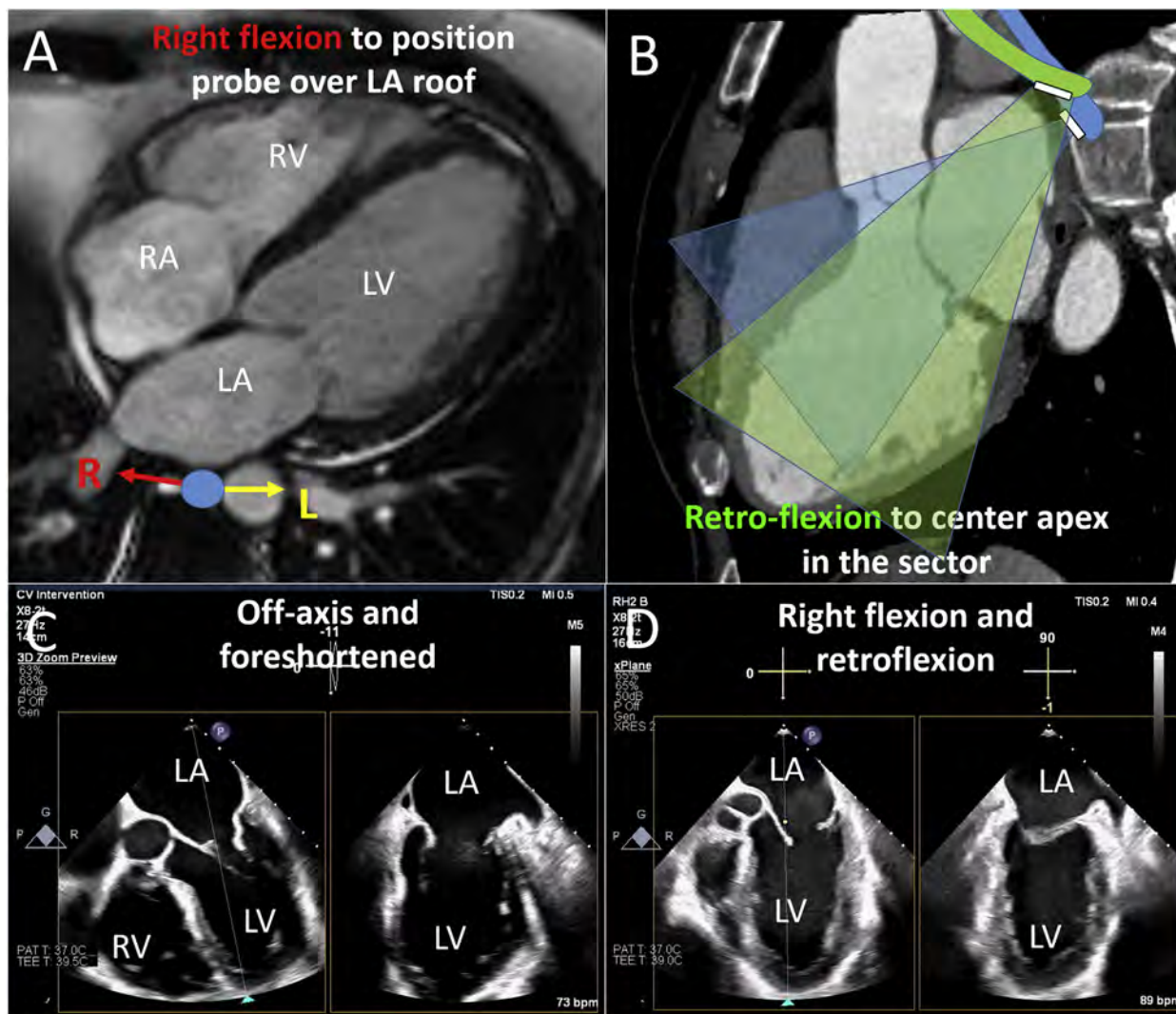


**Figure 14** Optimizing MV imaging. (A, B) Computed tomographic images of the heart to depict the location of the esophagus (blue dot) in relation to the cardiac structures. Because the heart is slightly horizontal in the chest, the esophagus is naturally closer to the lateral wall of the left atrium (LA), and thus to position the probe over the dome of the LA with the mitral annulus perpendicular to the insonation beam, one must use right flexion (A). To align the initial imaging plane (blue sector) with the left ventricular apex, retroflexion (green sector) is typically required (B). With these maneuvers, the tangential and foreshortened imaging of the MV and left ventricle (LV) at a 0° ME biplane view (C) can be corrected such that the annulus is perpendicular to the ultrasound beam, and the apex is centered in the far field (D) facilitating on-axis simultaneous multiplane imaging of the entire annular plane. RA, Right atrium; RV, right ventricle.

degeneration due to carcinoid heart disease, rheumatic or postinflammatory changes, drug or radiation exposure, and infective endocarditis.<sup>69</sup>

**2. General Imaging Protocol for the PV (Table 5). ME Views.** The ME RV inflow-outflow view (45°–60°) images the long axis of the RVOT and PV, anterior to the AV (Figure 21). From this view, the subpulmonary region is assessed for prominent muscle bundles or narrowing at the infundibular outlet septum suggestive of double-chambered RV (Figures 22A and 22B). Color Doppler turbulence may be present, but the ultrasound beam angle is suboptimal to obtain a reliable peak Doppler gradient for subvalvular or valvular stenosis.

**UE Views.** Withdrawing the probe may optimize imaging of the main and proximal branch PA, as there are no intervening left heart structures

(Figures 22C–22H). Focal narrowing at or above the sinotubular junction is consistent with supralvalvular stenosis. Doppler assessment of systolic and diastolic velocities for valvular and supralvalvular PS and PR is ideal from this position. However, “sufficient” or “excellent” imaging of the PV may be feasible only 50% of the time and is usually achieved with probe positions that are particularly uncomfortable for patients.<sup>70</sup>

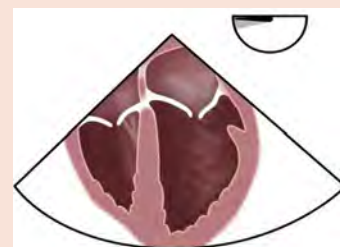
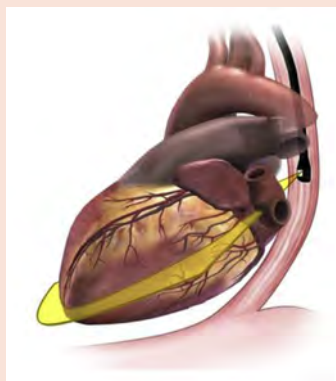
**TG Views.** At 0° to 20° with both right and anteflexion, a TG inflow-outflow view can be obtained (Figure 9G). Alternatively, at 40° to 60° with anteflexion and counterclockwise rotation from the LVOT view, a long-axis view of the entire RVOT is imaged in most patients (Figure 9F). This is the best opportunity to visualize the contribution of the infundibulum and moderator band for any dynamic subpulmonic stenosis. If the TG views fail to align the ultrasound beam

**Table 4** MV imaging protocol

**Imaging level: ME view 0°-20°**

**Acquisition protocol:**

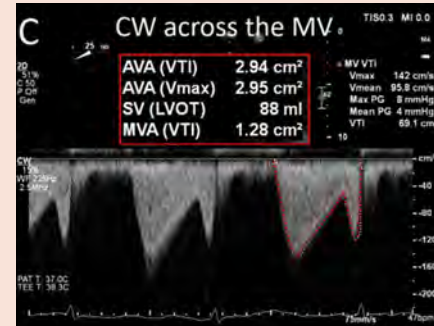
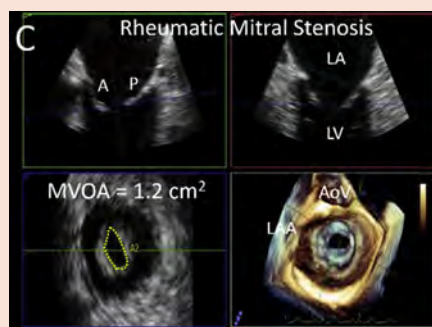
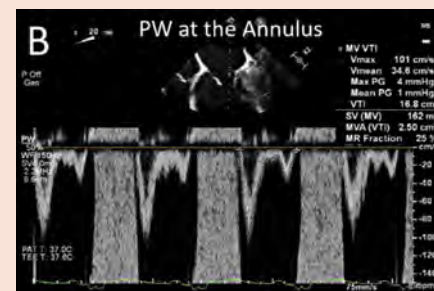
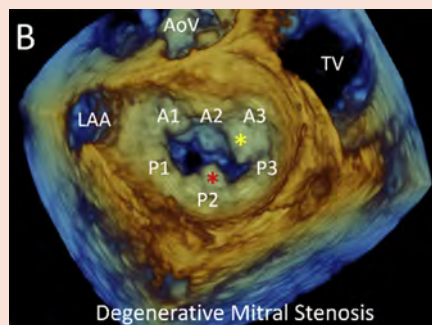
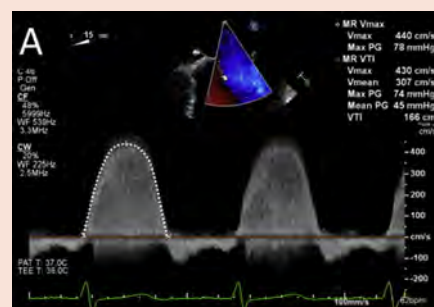
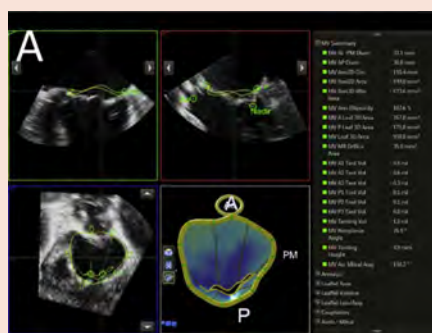
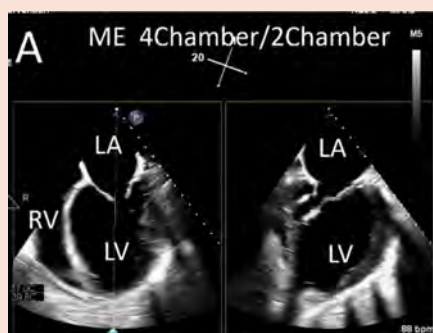
- From the ME 4Ch view focused on the MV (0°-20° multiplane angle may be necessary to eliminate the AV and the LVOT).
- To better align the MV, slight probe retroflexion may be necessary. Use tilt plane to illustrate simultaneous biplane image.



**Planar imaging**

**Volumetric imaging**

**Functional imaging**



A. Biplane imaging (4Ch/2Ch views) of a patient with a dilated cardiomyopathy. At this increased depth of field, ventricular size and function can be assessed in addition to leaflet motion, in this case, restricted in systole with marked leaflet tethering.

A. From a 3D volume, the mitral annulus can be measured using dedicated software (shown) or direct planimetry using multiplanar reconstruction.  
 B. Three-dimensional en face view from the degenerative MS case in planar image B shows the mitral annular calcium on the base of the A3

A. CW Doppler of the mitral regurgitant jet is required for quantitation; peak velocity is used for PISA effective orifice area calculation, and the MR VTI is used to quantify regurgitant volume.  
 B. PW Doppler at the MV annulus is used to quantify diastolic SV, in this case, 162 mL/beat.  
 C. CW Doppler of transmitral diastolic flow allows quantitation of peak/mean gradient,

(Continued)

**Table 4** (Continued)

**Imaging level: ME view 0°–20°**

B. Four-chamber view of degenerative MS with mitral annular calcium on the base of the anterior leaflet (*yellow asterisk*) and posterior leaflet (*red asterisk*) with the latter protruding into the MV orifice.

scallop (*yellow asterisk*) and P2 scallop (*red asterisk*).  
C. Three-dimensional multiplanar reconstruction of a rheumatic MS patient, used to planimeter the MV orifice area.

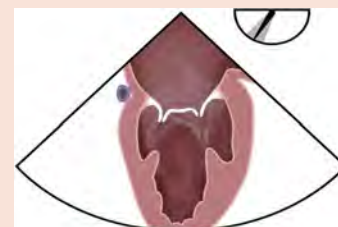
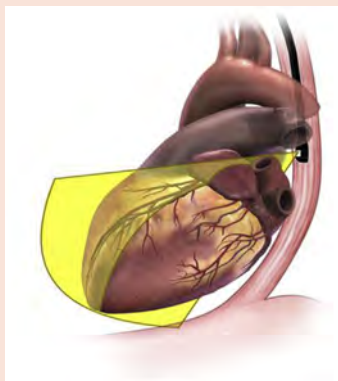
pressure half-time, and VTI. In this example from a patient with rheumatic MS, the VTI was used in the continuity equation to calculate a MV area of 1.28 cm<sup>2</sup>.

Note: Although not shown for every level of imaging, PW and CW Doppler as well as color Doppler assessment could be performed from any imaging plane of the MV that aligns the ultrasound beam with flow. These imaging planes will typically result in the most accurate Doppler spectral profiles.

**Imaging level: ME mitral commissural view 50°–70°**

**Acquisition protocol:**

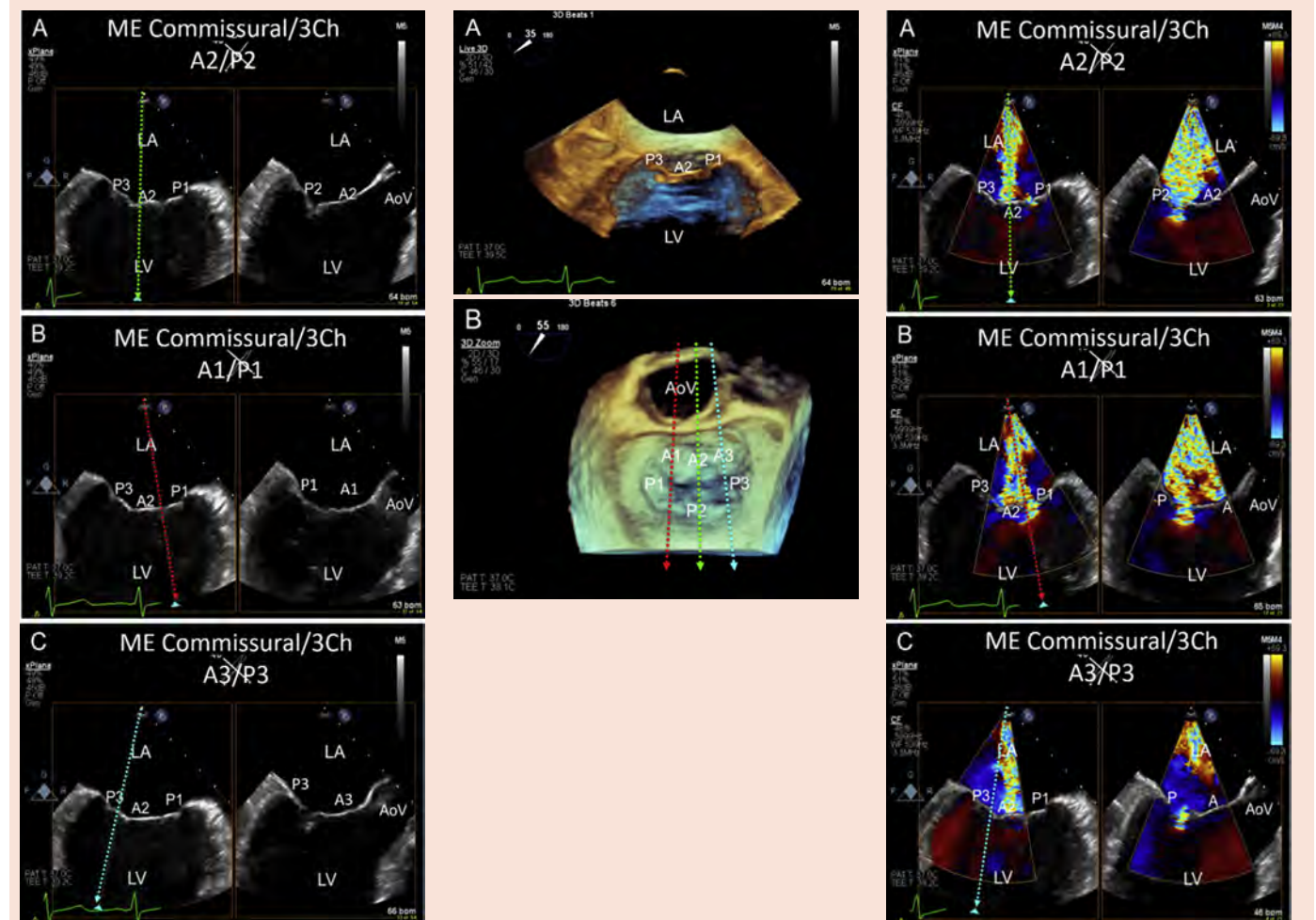
- Identify the mitral commissural view anatomically optimized to the MV plane (~50°–70°).
- Systematic biplane through MV leaflets permits sweeping interrogation of MV coaptation (central, lateral, and medial tilts) with 2D color Doppler by maintaining the biplane tilt angle.



**Planar imaging**

**Volumetric imaging**

**Functional imaging**



(Continued)

**Table 4** (Continued)

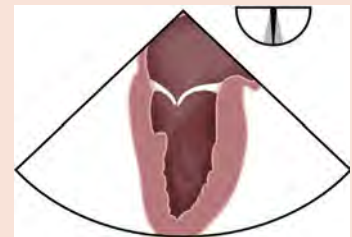
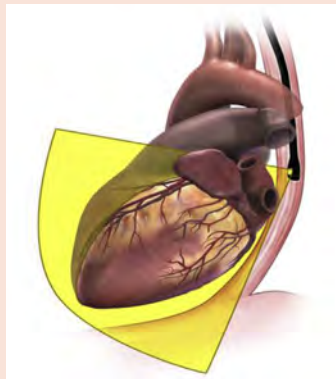
**Imaging level: ME mitral commissural view 50°–70°**

- |  |   |  |
|--|---|--|
| <p>A. Mitral commissural view images the anterior leaflet in the center (A2) and the posterior leaflet on either side (P3 left/medial and P1 right/lateral). Simultaneous biplane image shows MV long-axis view with anterior (A2) and posterior (P2) leaflets.</p> <p>B. Mitral commissural view with the simultaneous biplane tilt through lateral portion of the MV leaflets (A1/P1 coaptation zone).</p> <p>C. Mitral commissural view with the simultaneous biplane tilt through medial portion of the MV leaflets (A3/P3 coaptation zone).</p> | <p>A. Three-dimensional live imaging (narrow volume) may be particularly useful to verify appropriate multiplane angle for commissural view.</p> <p>B. Three-dimensional en face view of the MV during systole with the AV at 12 o'clock. The imaging planes of the lateral scallops (A1/P1, red line), midline scallops (A2/P2, green line) and medial scallops (A3/P3, blue line) are shown. In this patient the AV may be seen from all three commissural imaging planes (see planar imaging views) given the size/orientation of the aorta in this patient.</p> | <p>A. Mitral commissural view with 2D color Doppler illustrating the broad-based MR jet in the simultaneous biplane images. Central tilt plane denotes cutting plane through anterior and posterior leaflets (A2/P2).</p> <p>B. Mitral commissural view with 2D color Doppler and lateral tilt plane that denotes cutting plane through anterior and posterior leaflets (A1/P1).</p> <p>C. Simultaneous biplane imaging based on mitral commissural view with the tilt plane moved medially denotes cutting plane through anterior and posterior leaflets (A3/P3).</p> |
|--|---|--|

**Imaging level: ME mitral view 80°–100°**

**Acquisition protocol:**

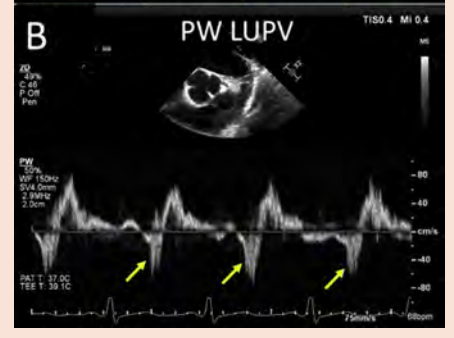
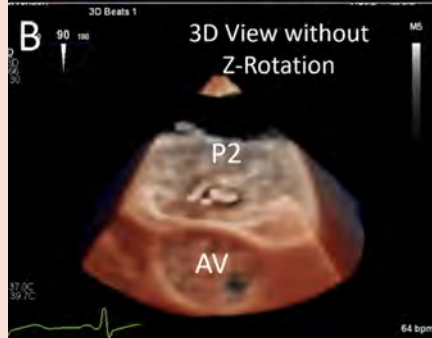
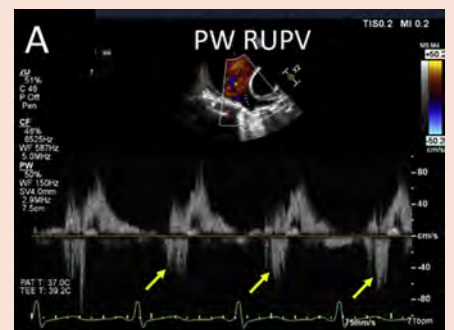
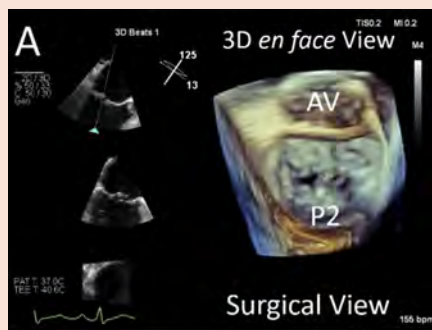
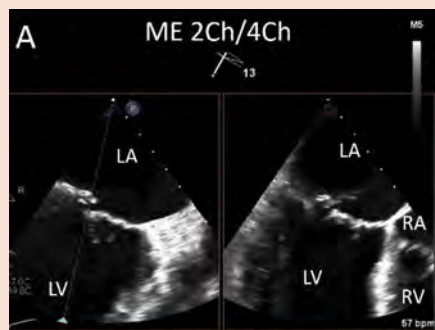
- From the ME 2Ch view focused on the MV. To better align the MV, slight probe retroflexion may be necessary. Use tilt plane to illustrate simultaneous biplane image.
- Three-dimensional acquisitions with and without color benefit from multibeat acquisition (improved temporal resolution).



**Planar imaging**

**Volumetric imaging**

**Functional imaging**



(Continued)

**Table 4** (Continued)

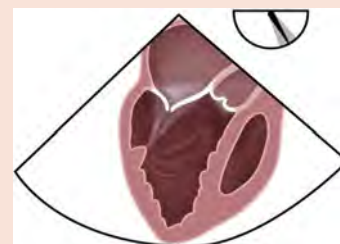
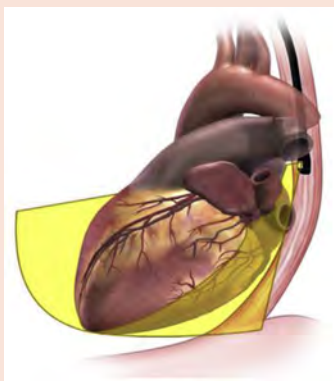
**Imaging level: ME mitral view 80°–100°**

- |   |  |   |
|---|--|---|
| <p>A. Biplane imaging from the ME 2Ch view with orthogonal inverted 4Ch view.</p> | <p>A. Three-dimensional rendering of the MV from the standard surgical en face view with the AV at 12 o'clock. The anterior leaflet is on <i>top</i>, posterior leaflet at the <i>bottom</i>.</p> <p>B. Three-dimensional rendering of the MV from a nonstandard view, obtained without z rotation. The AV is at 6 o'clock and the posterior leaflet is on <i>top</i>. This view may improve imaging of posterior leaflet pathology.</p> | <p>A. Reversal of flow in the pulmonary veins is a specific sign for hemodynamically significant MR. Flow in all four pulmonary veins can be assessed by PW Doppler. This is an example of late systolic flow reversal (<i>yellow arrows</i>) in the RUPV in the patient with flail P2 scallop.</p> <p>B. Late systolic reversal of flow (<i>yellow arrows</i>) is also seen in the LUPV.</p> |
|---|--|---|

**Imaging level: ME mitral view 120°–140°**

**Acquisition protocol:**

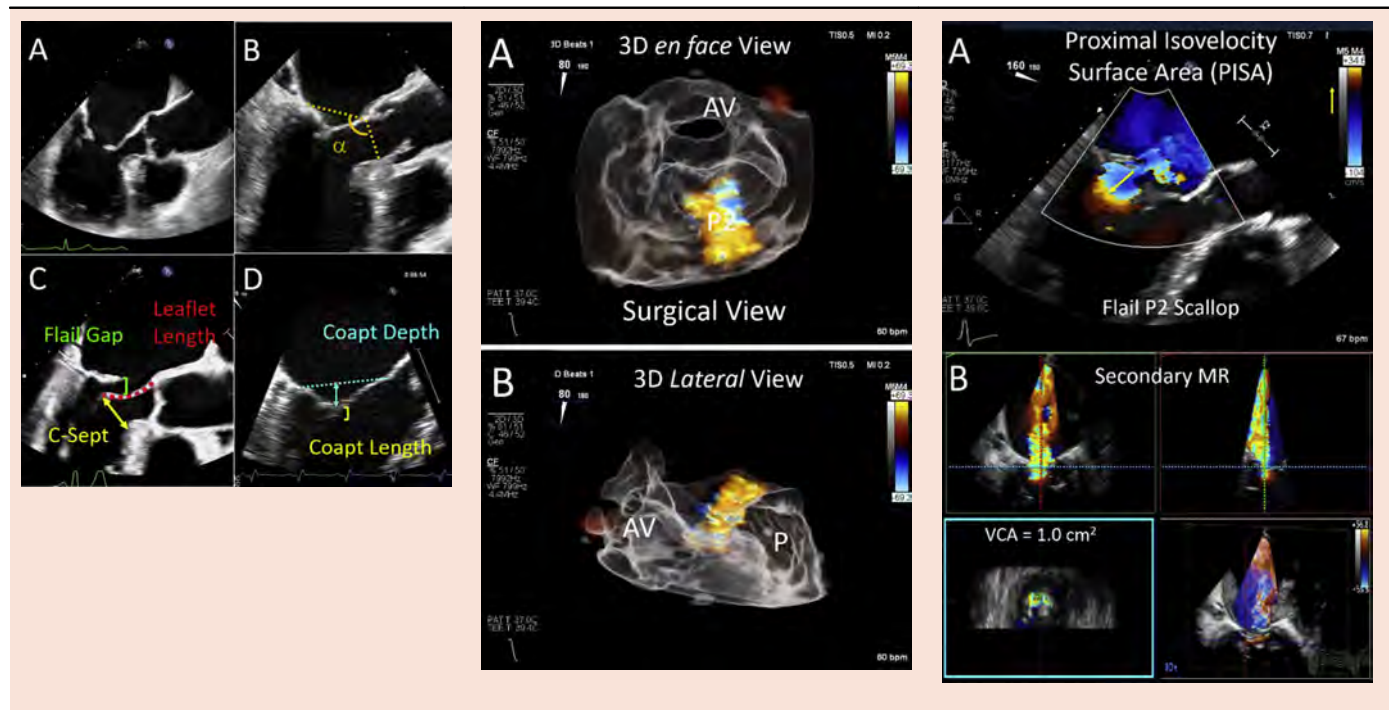
- From the ME long-axis view focused on the MV. To better align the MV, slight probe rotation, clockwise or counterclockwise, may be necessary. Use tilt plane to illustrate simultaneous biplane image.



**Planar imaging**

**Volumetric imaging**

**Functional imaging**



- |  |   |   |
|--|---|---|
| <p>A. The long-axis view, which usually images the anterior leaflet (A2) and posterior leaflet (P2), is useful for imaging leaflet morphology (rheumatic doming in this example) but also the LVOT and AV.</p> | <p>A. New 3D rendering modes may allow more rapid assessment of valve morphology and function. In this example of a transparency rendering of 3D color Doppler, the origin of the wide regurgitant jet of functional MR is easily seen.</p> | <p>A. To calculate the EROA by PISA method, the color Doppler baseline is shifted in the direction of regurgitant flow, and the radius of the PISA shell is measured from the vena contracta to the color shift from (in this case) yellow to blue (<i>yellow arrow</i>).</p> |
|--|---|---|

(Continued)

**Table 4 (Continued)**

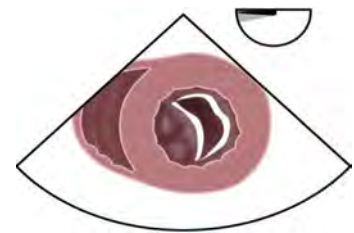
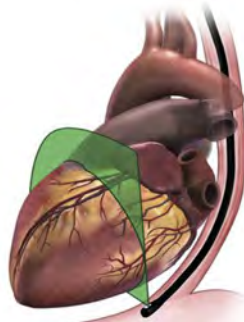
**Imaging level: ME mitral view 120°–140°**

- B. The systolic mitral-aortic annular angle ( $\alpha$ ), which is used to assess the risk of LVOT obstruction.
  - C. Degenerative MV leaflet measurements include flail gap, anterior leaflet length, and the C-sept distance.
  - D. Measurements of tethered leaflets include coaptation length and depth.
- B. The same patient's 3D color Doppler volume is imaged from a lateral aspect, with the anterior annulus to the left (AV, aortic valve) and posterior annulus (P) to the right. From this aspect, the regurgitant jet is posteriorly directed.
- B. Three-dimensional color Doppler multiplanar reconstruction is used to identify the vena contracta in SAX (blue plane) allowing planimetry of the VCA.

**Imaging level: TG views**

**Acquisition protocol:**

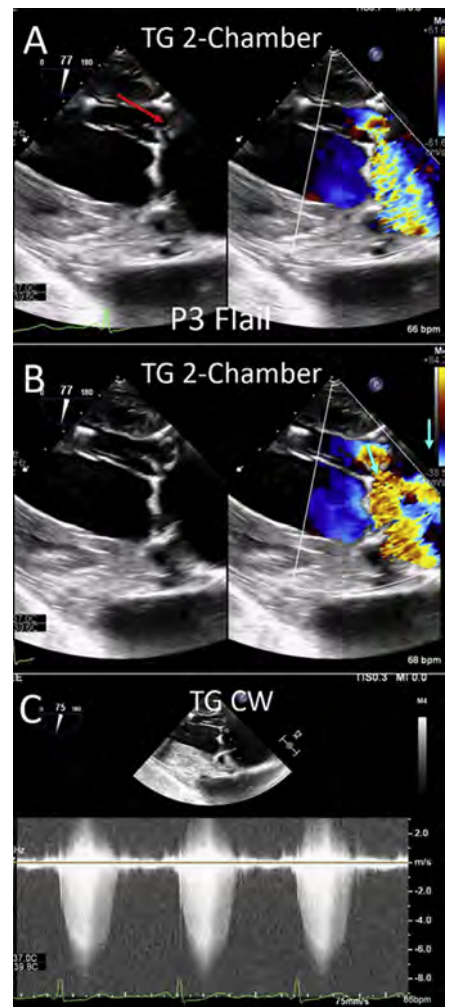
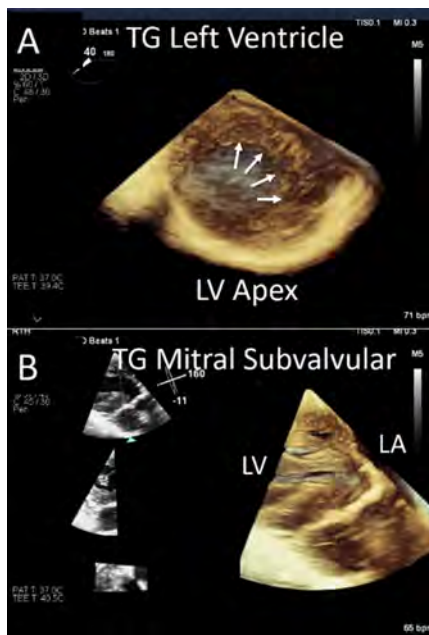
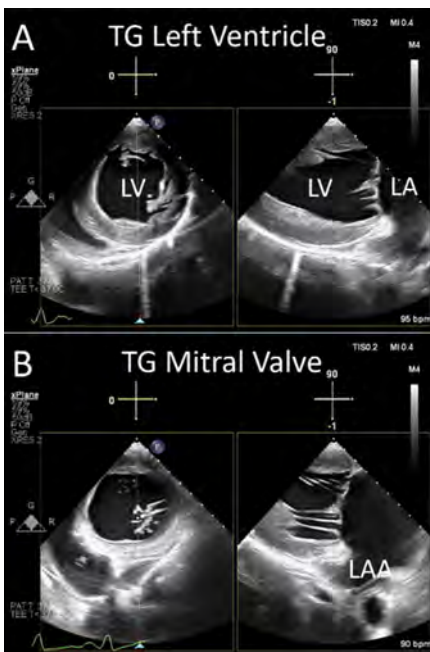
- Following insertion of the probe past the lower esophageal sphincter into the stomach, antelexion results in imaging of the left ventricle.
- Further antelexion from a midventricular view brings the imaging plane to the base of the left ventricle and images the MV.
- Further retroflexion from the midventricular view images the LV apex.



**Planar imaging**

**Volumetric imaging**

**Functional imaging**



(Continued)

Table 4 (Continued)

## Imaging level: TG views

<p>A. TG SAX view of the mid left ventricle with simultaneous biplane long axis should be performed to assess LV size and function.</p> <p>B. TG SAX view at the level of the MV with simultaneous biplane long axis should be performed to assess leaflets as well as subvalvular structures.</p>	<p>A. Three-dimensional volume acquisition from the TG view shows the marked trabeculations of the lateral LV apex, consistent with noncompaction.</p> <p>B. Three-dimensional volume of the MV from TG views can be used to evaluate the subvalvular apparatus.</p>	<p>A. Eccentric MR jets may be aligned with the ultrasound beam from TG views. In this example of a P3 (medial) flail, the regurgitant jet is best aligned with the ultrasound beam from this TG view.</p> <p>B. When optimally aligned with the ultrasound beam, color Doppler baseline shift in the direction of regurgitant flow (<i>blue arrow</i>) allows measurement of the PISA radius.</p> <p>C. CW Doppler should be performed from any view where the regurgitant jet is aligned with the ultrasound beam.</p>
--	--	--

To quantify mitral regurgitant volume, a comprehensive examination should include the 2D/Doppler quantitation of forward SV (i.e., left ventricular or right ventricular stroke volume) with Doppler performed from the TG views.

2Ch, Two-chamber; 3Ch, three-chamber; 4Ch, four-chamber; A, anterior leaflet; AoV, aortic valve; AVA, AV area; Coapt, coaptation; C-sept, Coaptation-to-septal; EROA, effective regurgitant orifice area; LA, left atrium; LUPV, left upper pulmonary vein; LV, left ventricle; MVA, MV area; MVOA, MV orifice area; P, posterior leaflet; PG, pressure gradient; PM, posteromedial; PW, pulsed wave; RA, right atrium; RUPV, right upper pulmonary vein; RV, right ventricle; SV, stroke volume; VCA, vena contracta area; Vmax, maximum velocity; Vmean, mean velocity; VTI, velocity-time integral.

parallel to flow for Doppler assessment of PV function, DT views with maximum anteflexion can be attempted.

**Three-Dimensional Imaging.** The PV remains in the far field at all imaging levels; thus 3D rendering of the valve is challenging. The UE view typically yields the best imaging of the leaflets to optimize 3D acquisition, as the annular plane is more perpendicular to the ultrasound beam (Figures 22G and 22H).

**3. PV Stenosis.** Valvular PS is the second most common congenital heart defect, occurring in 10% of children with congenital heart disease but not infrequently first diagnosed in adulthood.<sup>71</sup> Fusion of the commissures results in a dome-shaped valve with a narrowed effective orifice that often is accompanied by poststenotic dilatation of the main PA. Mild PS, defined as a peak Doppler gradient < 36 mm Hg, does not require intervention and rarely progresses. Moderate or severe disease, with a peak Doppler gradient > 36 mm Hg accompanied by otherwise unexplained symptoms of heart failure, may require treatment with balloon valvuloplasty or surgical valvotomy<sup>72</sup> ranging from commissurotomy to subtotal leaflet

resection, with low procedural risk and low rate of recurrence.<sup>73</sup> The “dysplastic” type of valvular PS, most commonly seen in patients with Noonan syndrome, responds less favorably to percutaneous intervention due to myxomatous, thickened leaflets, and associated annular hypoplasia or narrowing of the supra-annular region. PS can be associated with numerous other congenital defects including atrial septal defect (ASD), ventricular septal defect (VSD), patent ductus arteriosus, and other complex congenital heart diseases such as tetralogy of Fallot, which is defined by RVOT obstruction. Acquired PS is rare, constituting only 5% of patients presenting in adulthood. Causes of acquired PS include carcinoid and rheumatic heart disease.

Subvalvular PS is rare and may present below the infundibulum, as in double-chambered right ventricle, which occurs at the infundibular os, or even more rarely immediately below the PV. There are multiple other causes, but none is amenable to catheter-based intervention.

Supra-annular PS can variably involve the main and/or branch pulmonary arteries. Congenital cases are associated with various genetic and congenital syndromes and may be acquired because of postoperative suture lines, vessel distortion, or external compression.

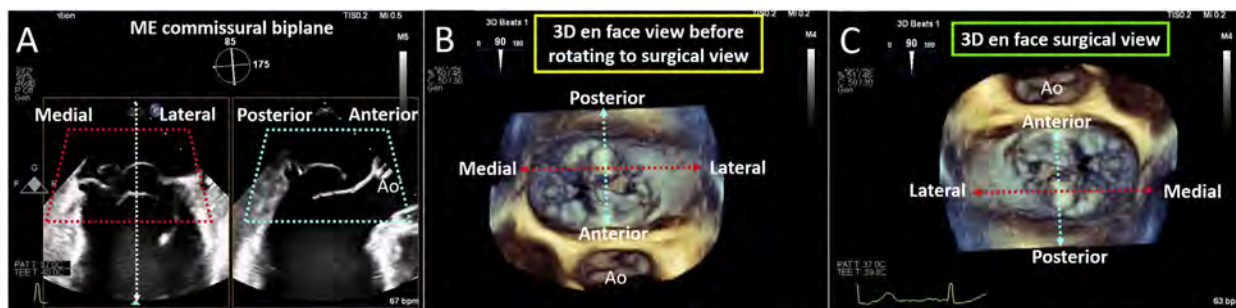


**Figure 15** Two-dimensional and 3D imaging of the MV. In this example of a large flail P2 scallop, the use of biplane imaging allows simultaneous display of the commissural view (*left-hand image in A*) and the orthogonal midline (A2-P2 commissure) long-axis view (*right-hand image in A*). The user-defined images that generate the 3D volume in panel **B** are shown: lateral (*red box*) and elevational (*blue box*). The 3D-rendered image in panel **B** is the initial en face MV view from the atrial perspective; medial to the left, lateral to the right, anterior at the bottom, and posterior at the top of the echocardiographic image with the aorta (Ao) at 6 o'clock. To generate the surgeon's en face view, the image in panel **B** is then rotated 180° in the z axis (**C**) so that the Ao is now at 12 o'clock.

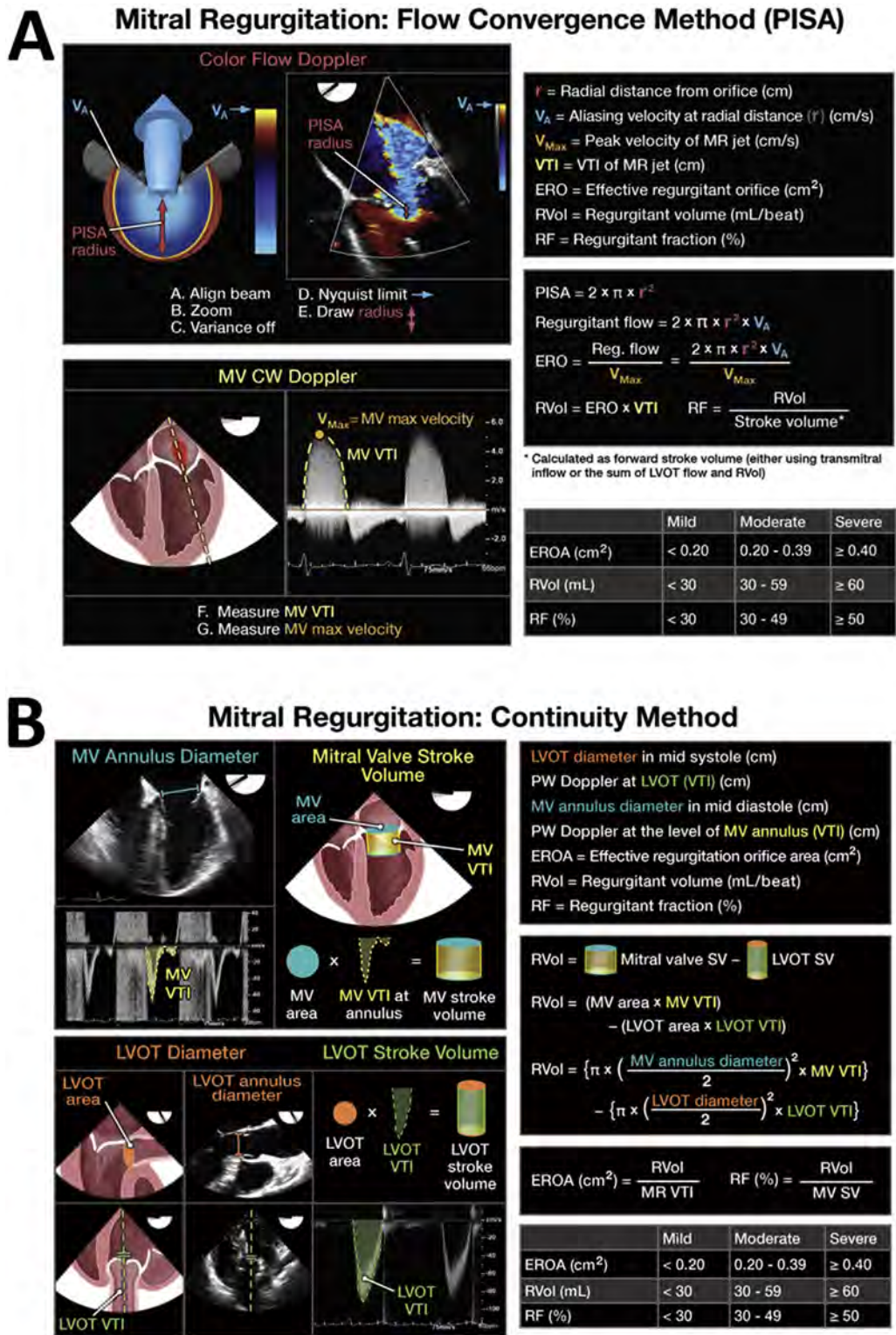


**Figure 16** Quantitation of MR. Quantitation of MR should be performed whenever there is a question about disease severity and clinical status. Panel **A** shows the images required to perform a PISA measurement of effective regurgitant orifice area (EROA), including (1) color Doppler with baseline shift in the direction of the regurgitant jet with PISA radius measured and (2) CW Doppler spectral profile. The calculation of EROA as shown can then be used to quantify the regurgitant volume. Panel **B** shows the images required to perform the quantitative Doppler method of calculation of the regurgitant volume, including four-chamber mitral annular diastolic diameter, pulsed-wave (PW) Doppler at the mitral annular plane, aortic annular systolic diameter, PW Doppler at the aortic annular plane, and CW Doppler of the transmitral systolic velocity profile. Subtracting the forward stroke volume (i.e., across the AV) from the diastolic stroke volume (across the MV) results in the regurgitant volume. EROA is then derived by dividing the regurgitant volume by the CW Doppler transmitral velocity-time integral (VTI). *ERO*, Effective regurgitant orifice; *r*, PISA radius; *Reg. flow*, regurgitant flow; *RF*, regurgitant fraction; *RVol*, regurgitant volume; *V<sub>A</sub>*, aliasing velocity; *V<sub>Max</sub>*, peak velocity.

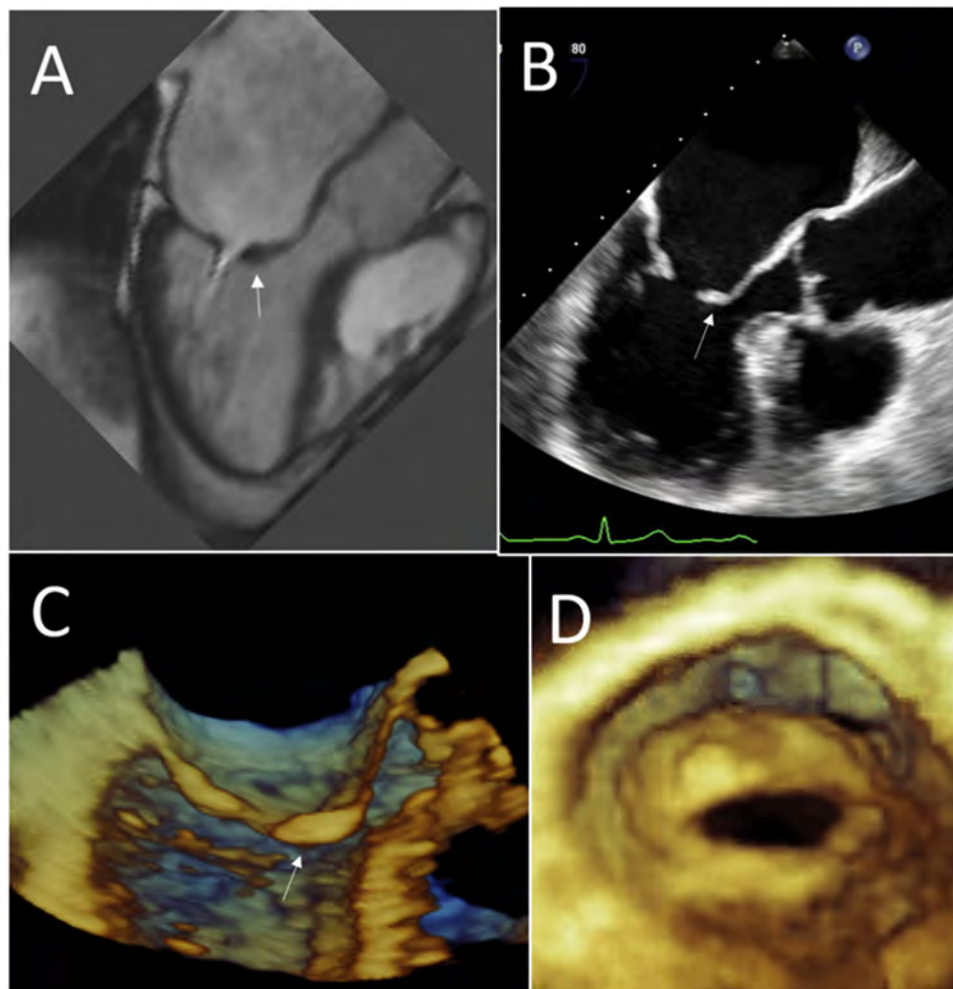


**Figure 17** Characteristic features of rheumatic MS. Doming of the anterior mitral leaflet can be seen on cardiac magnetic resonance (arrow, **A**), 2D TEE imaging (**B**), and 3D TEE imaging (**C**). Three-dimensional en face imaging (LV perspective) shows the “fish mouth” appearance of the MV (**D**).

Supravalvular stenosis adjacent to the PV is not amenable to percutaneous intervention without sacrificing the valve, so if echocardiography suggests narrowing in this area, additional imaging may be required to direct the patient to surgical repair.

In summary, when considering PS, pathology can occur anywhere along the RVOT. As percutaneous options are only available for isolated valvular pathology, recognition of narrowing above and below the valve is crucial, as are identification and assessment for commonly associated additional lesions that may require intervention.<sup>74</sup>

**4. PV Regurgitation.** Isolated PR is rarely a native lesion but rather a consequence of prior valvotomy or following replacement performed for valvular PS. One rare exception is a severe variant of tetralogy of Fallot with absent PV syndrome. As the name implies, the leaflets are usually completely absent, although occasionally vestigial remnants of thickened, cauliflower-like tissue may be seen. The condition is invariably accompanied by severely dilated main and bilateral branch pulmonary arteries, creating severe respiratory symptoms that traditionally present in infancy, at which time they are surgically addressed. Noncongenital PR, secondary to degeneration of the PV, typically presents with combined regurgitation and stenosis, as in carcinoid heart disease.<sup>75</sup> For the rare case with predominant stenosis

and mild or less regurgitation, balloon valvuloplasty may be adequate, but most will require replacement. A color Doppler PR jet width >50% to 65% of the RVOT, rapid flow deceleration with early termination of diastolic flow, and diastolic flow reversal in the branch pulmonary arteries are consistent with significant PR.<sup>76,77</sup>

#### **5. PV Disease in Postoperative Congenital Heart Disease.**

Both PS and PR can result after intervention for numerous congenital heart defects, most notably tetralogy of Fallot. The postoperative RVOT has remarkable heterogeneity, in part because of a broad range of interventions that may have been initially performed, including subtotal or total leaflet resection, implanted surgical valves, and conduits.<sup>78</sup> Surgical PV repair is rarely performed<sup>79</sup>; rather the majority of interventions for regurgitation or combined disease are replacements, with transcatheter replacement now possible in greater numbers of patients since the first description in 2000.<sup>80</sup> Transcatheter device selection is based on the outflow tract, rather than leaflet morphology, best evaluated on magnetic resonance imaging or CT. Chronic, severe PR causes progressive RV dilatation and ultimately dysfunction. Magnetic resonance imaging is the gold standard for quantitation of PR and RV size and function, although CT is an alternative in patients with contraindications to magnetic resonance imaging. Criteria for PV replacement are derived from

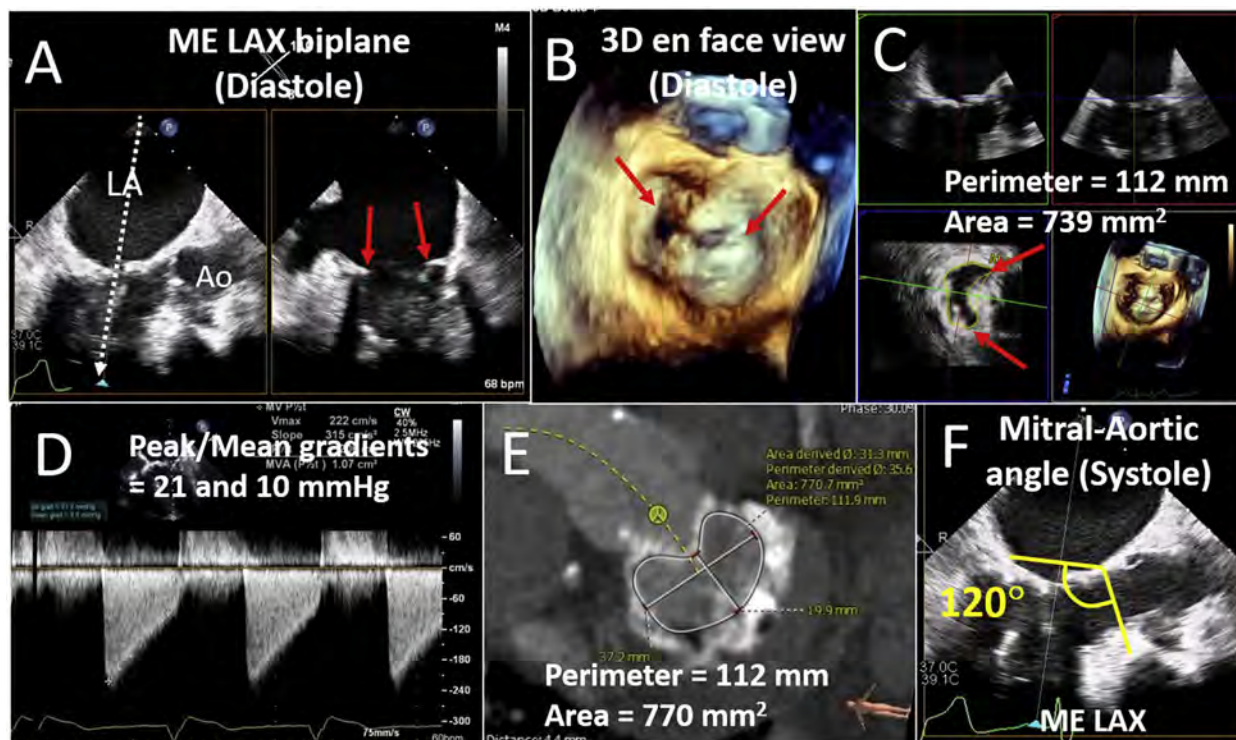


**Figure 18** Degenerative mitral stenosis (MS). Mitral annular calcium (MAC) can variably extend onto the leaflets, but the greatest restriction to flow typically occurs at the annulus. Biplane imaging from the mid esophageal (ME) view (**A**, the *white arrow* indicates the location of the orthogonal image) and 3D en face view (**B**) show the location of the annular calcium (*red arrows*). Using 3D multiplanar reconstruction (**C**), the annular area by planimetry is 0.74 cm<sup>2</sup>, consistent with severe MS due to increased rigidity of the annulus and leaflets without commissural fusion (*red arrows* in **A–C**). CW Doppler (**D**) shows peak and mean gradients of 21 and 10 mmHg, respectively. The severity and extent of calcium is frequently more accurately assessed by computed tomographic (CT) imaging (**E**), which can also be used to assess the severity of stenosis. The risk for left ventricular outflow obstruction following transcatheter mitral valve replacement can be predicted by the baseline acuity of the mitral-aortic angle (**F**). Ao, Aorta; LA, left atrium; LAX, long-axis.

these multimodality imaging parameters and a host of clinical criteria that continue to evolve.

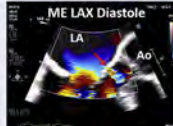
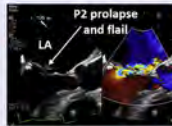
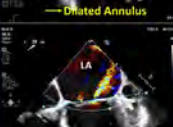
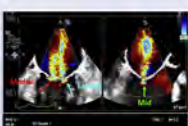
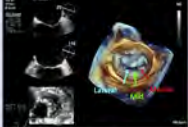
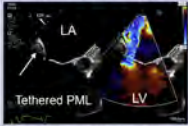
## F. Assessment of the TV

Interest in the TV has grown, given the prevalence of significant TR and its association with adverse prognosis,<sup>81</sup> as well as the symptom burden resulting from progressive right heart failure.<sup>82</sup> In the setting of high in-hospital mortality associated with isolated TV surgery,<sup>83</sup> transcatheter devices continue to evolve.<sup>84</sup> Imaging the TV with TEE is challenging for a number of reasons. First, it is the most anteriorly and inferiorly positioned cardiac valve, with a normal orifice area between 7 and 9 cm<sup>2</sup>,<sup>85</sup> thus requiring a large field of view when imaged in the far field from ME views. Second, the tricuspid leaflets are much thinner than those of the MV, making them more difficult to image.<sup>86</sup> Finally, the annular plane cannot be aligned perpendicular to the ultrasound beam, increasing the reliance on lateral resolution, which is inferior to axial resolution. The TV, however, is positioned immediately superior to the diaphragm and is therefore very close to the TEE probe in the DE as well as TG views. Thus, a new imaging level, the DE imaging plane, is required (*Table 1*). These views have become integral to preprocedural assessment of the TV.

**1. Anatomy of the TV. Tricuspid Annulus.** The normal tricuspid annulus has a complex elliptical nonplanar shape, with the anteroseptal portion being the highest, close to the RVOT and AV, and the posterolateral portion being the lowest (toward the right ventricle). It is about 20% larger and less symmetric than the “saddled-shaped” mitral annulus

and can be divided into two segments: mural and septal (*Figure 23A*). Like the MV, the mural or free wall portion of the TV annulus consists of four components: the atrial myocardium, the ventricular myocardium, the hinge line of the tricuspid leaflets, and the epicardial adipose tissue (*Figures 23B* and *23C*). Tricuspid annular dilatation and leaflet tethering are the primary mechanisms leading to functional TR.<sup>86</sup> The mural annulus follows the contraction of the right ventricle and may be subjected to dilatation when the right atrium and/or RV enlarge, while the septal annulus is spared from annular dilatation.<sup>87</sup> Recent 3D echocardiographic studies have demonstrated annular expansion primarily along the posterior border in TR associated with atrial fibrillation, whereas the annulus expands mostly along the anterolateral border in patients with left heart disease in sinus rhythm.<sup>88</sup>

**Tricuspid Leaflets.** The TV classically consists of three unequally sized leaflets called anterior (the largest, with a quadrangular shape), septal (long circumferentially but short radially, semicircular in shape), and posterior (intermediate in size, with a triangular shape and scalloped indentations; *Figures 23D–23F*). Autopsy studies, however, have reported large variability in the number of TV leaflets in up to 38% of patients.<sup>87</sup> A recent TEE study of 579 patients confirmed these finding, with three leaflets seen in just over 50% of patients and four or more leaflets seen in 39% of patients.<sup>89</sup> A majority of quadricuspid valves (32% of the entire cohort) had two posterior leaflets (*Table 6*). Identification of TV leaflet morphology relies on the TG SAX view (or 3D volume-rendered short axis from any imaging level), using leaflet edge motion and color Doppler (when malcoaptation is present) during the cardiac cycle to identify (1)

Morphologic Classification	Carpentier Type I	Carpentier Type II	Carpentier Type IIIa	Carpentier Type IIIb	
	Normal leaflet motion	Excess leaflet motion	Restrictive leaflet motion (systole & diastole)	Restrictive leaflet motion (systole only)	
<b>PRIMARY</b>					
<ul style="list-style-type: none"> <li>Mitral valve prolapse               <ul style="list-style-type: none"> <li>Barlow's Disease</li> <li>Fibroelastic deficiency ± Flail</li> </ul> </li> <li>Papillary Muscle Rupture</li> <li>Trauma/Endocarditis</li> <li>Rheumatic</li> <li>Collagen Vascular</li> <li>Radiation</li> <li>Drugs</li> <li>Mitral Annular Calcium</li> </ul>	  Leaflet perforation	  Mitral valve prolapse	  Rheumatic valve disease		
<b>SECONDARY</b>					
<ul style="list-style-type: none"> <li>Atrial Functional               <ul style="list-style-type: none"> <li>Dilated Annulus</li> </ul> </li> <li>Ventricular Functional               <ul style="list-style-type: none"> <li>Non-ischemic cardiomyopathy</li> <li>Ischemic cardiomyopathy</li> </ul> </li> </ul>	  Dilated mitral annulus (Atrial functional)			  Non-Ischemic cardiomyopathy	 Ischemic cardiomyopathy

**Figure 19** Classification of the mechanism of mitral regurgitation (MR). Mitral regurgitation can be divided into primary and secondary disease; a number of different leaflet motions may be seen within each of these categories. Primary MR is defined by pathology of mitral apparatus including the leaflet, chordae, or papillary muscles. Thus, primary MR may have: normal leaflet motion (Carpentier type I) in the setting of leaflet perforation/destruction; excess leaflet motion (Carpentier type II) in the setting of degenerative disease (i.e., Barlow's disease or fibroelastic deficiency) and flail leaflets (i.e., with chordal rupture); or restricted motion (Carpentier type IIIa) in the setting of rheumatic or calcific disease. In secondary MR, the mitral apparatus is normal, however, dilatation of the left atrium (LA) or left ventricle (LV) may result in malcoaptation of the leaflets. In atrial functional MR, the annulus is dilated with inadequate leaflet length to cover the annular area, however, leaflet motion is normal (Carpentier class I) with leaflets closing at or near the annular plane. In ventricular function MR, dilatation of the ventricle and displacement of the papillary muscles toward the apex result in leaflet tethering (i.e., location of leaflet coaptation apical to the annulus) with restriction of leaflet closure but normal diastolic excursion (Carpentier class IIIb). Systolic leaflet excursion may be symmetric (typical of non-ischemic cardiomyopathies) or more localized (typical of ischemic cardiomyopathy with regional wall motion abnormalities). Ao, Aorta; LAA, left atrial appendage; LAX, long-axis view; LV, left ventricle; MAC, mitral annular calcification; ME, mid esophageal; PML, posterior mitral leaflet.

independent motion from the adjacent leaflet and (2) color Doppler systolic flow extending into the region around the leaflet. A few important anatomic clues can be used to identify the leaflets. First, the septal leaflet is associated with the interventricular and/or IAS. The commissure between the septal and anterior leaflets is typically adjacent to the most posterior border of the noncoronary aortic sinus. The posterior leaflet, which is often scalloped, extends from the region of the anterior papillary muscle (along the lateral RV free wall) to the posterior wall of the right ventricle. The commissure between the septal and posterior leaflets is typically near the inflow of the coronary sinus. Because functional TR is associated with lateral dilatation of the annulus, malcoaptation of the leaflets frequently occurs along the septal coaptation line, and thus the TR regurgitant orifice is often crescent shaped or elliptical.

**Papillary Muscles.** There are two distinct papillary muscles (anterior and posterior) and a third variable papillary muscle (septal). The largest is typically the anterior papillary muscle, which may be continuous with the moderator band, supplying chordal support to both the anterior and posterior leaflets. The posterior papillary muscle, which is

often bifid or trifid, lends chordal support to the posterior and septal leaflets. The septal papillary muscle is absent or small in up to 20% of normal patients, and frequently there are multiple direct chordal attachments from the septum to the septal tricuspid leaflet. The commissure between the septal and anterior leaflets tends to be the longest.

## 2. General Imaging Protocol for the TV (Table 6). ME Views.

There are two standard imaging planes from the ME level, although comprehensive imaging using mechanical rotation from 0 to 150° should be considered. Imaging with the ME four-chamber view at about 0° and the ME RV inflow-outflow view at about 60° is described in Figure 24A and Table 6. From a ME four-chamber view of the heart at 0°, clockwise rotation of the probe to image the right heart usually images the septal leaflet (arising from the septum); the opposing leaflet is usually the anterior leaflet given its larger size compared with the posterior leaflet. However, retroflexion of the probe may image the posterior leaflet, and simultaneous biplane imaging may help clarify which leaflet is imaged, as the anterior leaflet is typically seen adjacent to the aorta and the posterior

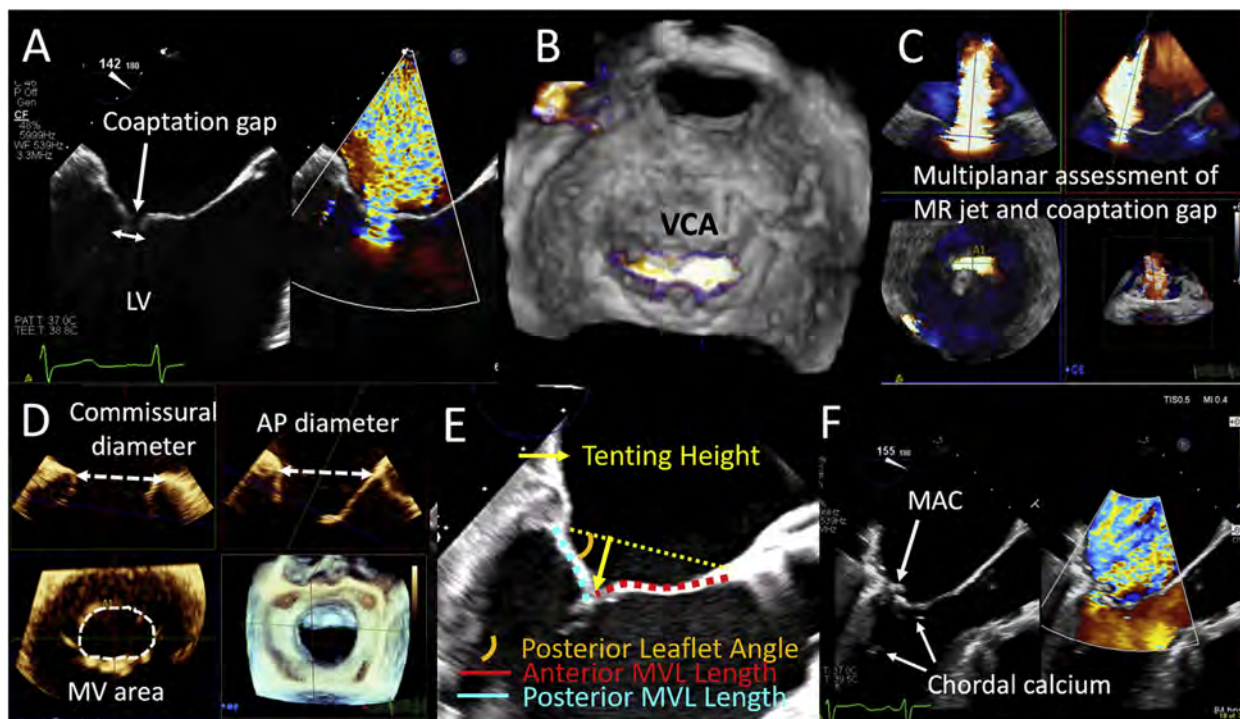


**Figure 20** Functional MR. Important imaging requirements for functional MR include determining the size of the coaptation gap and resulting MR jet vena contracta diameter (**A**). Three-dimensional color Doppler allows a rapid assessment of the shape of the vena contracta orifice and planimetry of the vena contracta area (VCA), which is frequently elliptical (**B**), and measurement of VCA (**C**). Three-dimensional imaging is also essential to assess the annular dimensions and area (**D**) not only to quantify regurgitant severity but also to assess suitability for transcatheter devices. Analysis of reparability as well as assessment of LVOT obstruction risk requires measurement of tenting angle, leaflet lengths, and tenting height (**E**). The relationship between the LVOT and subvalvular or valvular structures should be evaluated in both diastole and systole (**F**). AP, Anteroposterior; LV, left ventricle; MAC, mitral annular calcium; MVL, MV leaflet.

leaflet is adjacent to the posterolateral RV wall (**Figure 24B**). The right atrium and RV can also be evaluated for both size and function.

The second standard ME imaging plane is the RV inflow-outflow view at 60° (**Figures 24C–24F, Table 6**). On single-plane imaging, the anterior leaflet is adjacent to the aorta and the posterior leaflet is opposite, attached to the posterolateral wall of the right ventricle (**Figure 24C**). The septal leaflet is behind the plane of imaging, which can be appreciated from the real-time narrow-sector 3D volume (**Figure 24D**). Using simultaneous biplane imaging, scanning from the aortic side (anterior annulus) to the opposite side of the valve (posterior annulus) will permit imaging of the entire commissure between the septal and anterior leaflets (**Figure 24E**) and septal and posterior leaflets (**Figure 24F**).

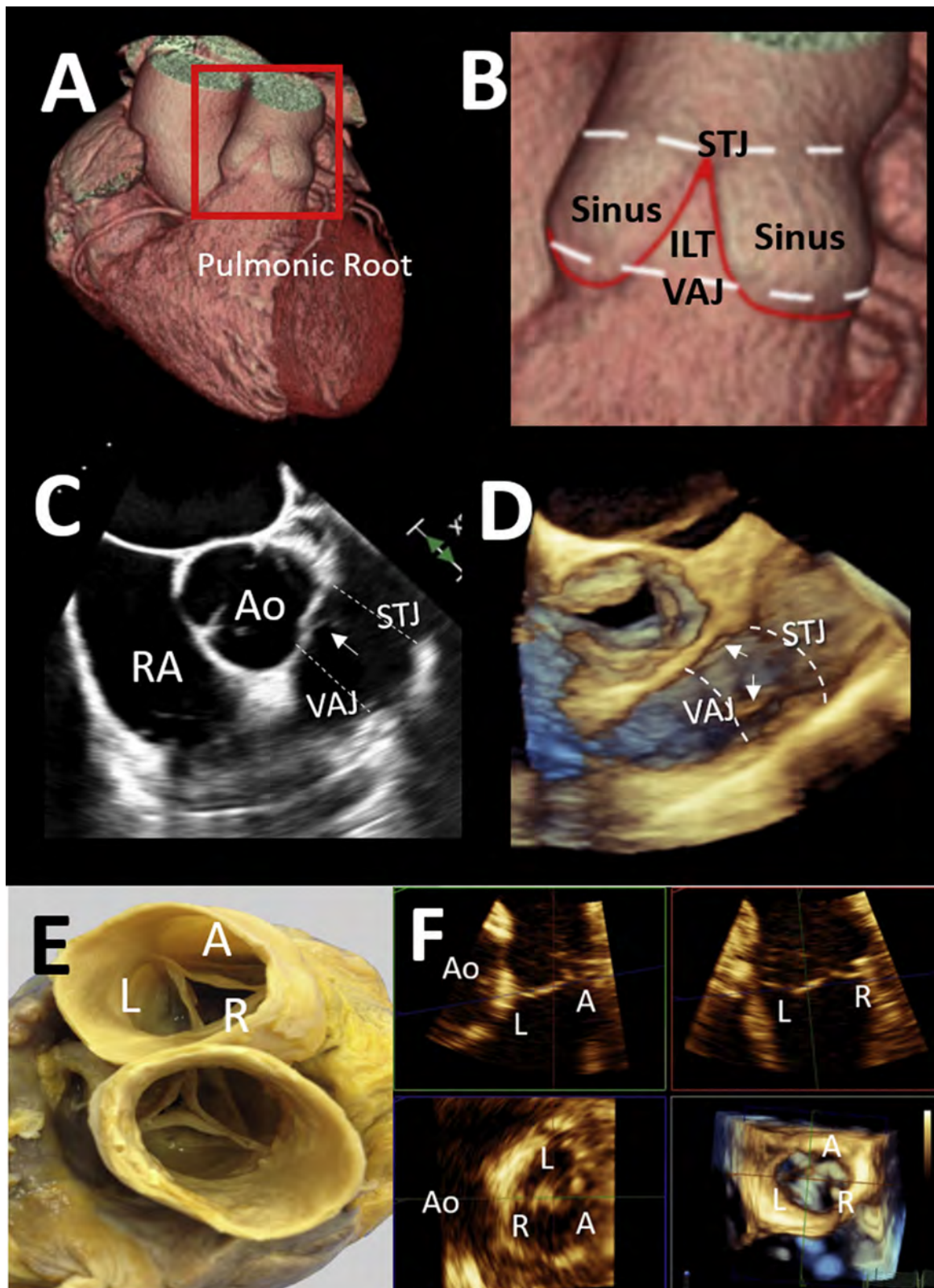
**DE Views.** Because the lower right heart border is close to the diaphragm, careful insertion of the TEE probe into the distal esophagus brings the probe closer to the tricuspid annulus (**Figure 25A**). From the DE level, the 0° view may image the septal leaflet or the posterior leaflet, with the opposing anterior leaflet; 3D imaging (**Figure 25B**) may be required to identify the leaflets. A dedicated DE RV inflow-outflow view (at 60°–90°) should also be performed (**Figure 25C**) and a sweep of the TV annulus performed as described for ME-level imaging. The DE level may allow alignment of the Doppler beam with the regurgitant jet and permit a comprehensive evaluation of TV function.

**TG Views.** Because of the proximity of the TV to the TEE probe from TG views, this imaging level is ideal for identifying leaflet and subvalvular morphology. The TG RV inflow-outflow view is obtained at 0° by advancing the probe into the stomach, rotating clockwise to center the TV in the imaging plane, and using both right and anteflex-

ion (**Figure 25D**). The orthogonal biplane view positioned at the leaflet tips can be used to identify the complex leaflet anatomy,<sup>89</sup> or alternatively, a single-plane SAX view can be obtained between 20° and 60° (**Figure 25E**).<sup>90</sup> This view may be particularly useful to image the coaptation zone at the tips of the leaflets and the origin of the TR jet on color Doppler. If imaging at the tips of the leaflets cannot be obtained with a single-plane image at 20° and 60°, then it is helpful to rotate to about 90° to 120° and obtain the two-chamber RV view, where the orthogonal biplane cursor can be positioned at the leaflet tips in systole. The TG view is one of the essential preprocedural planning views, particularly for transcatheter edge-to-edge repair, as the coaptation gaps of the leaflet tips can be measured and the location of the regurgitant orifice can be confirmed. Three-dimensional imaging can also be used to identify leaflets and the location of the papillary muscles (**Figure 25F**).

**DT Views.** Advancing the TEE probe further into the stomach along with rightward anterior flexion produces a DT view of the TV (**Figure 25G**), which may also align the ultrasound beam with flow across the TV and thus permit accurate Doppler interrogation (**Figure 25H**).

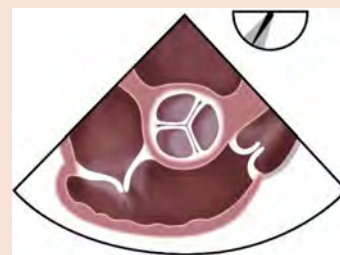
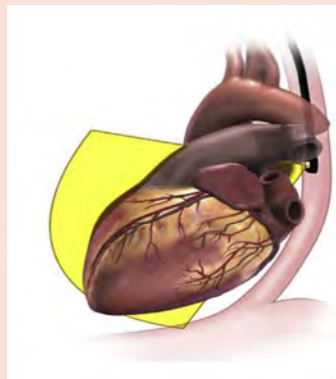
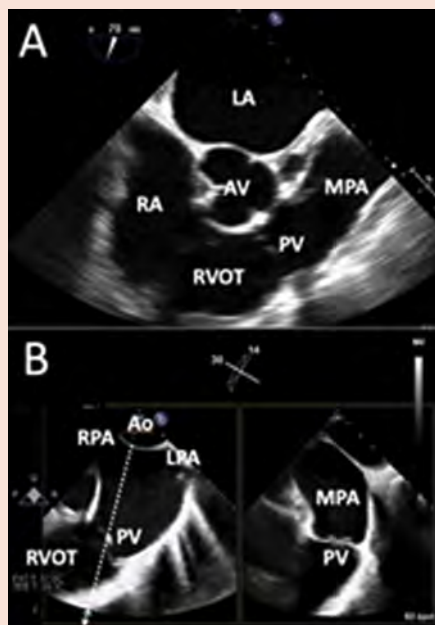
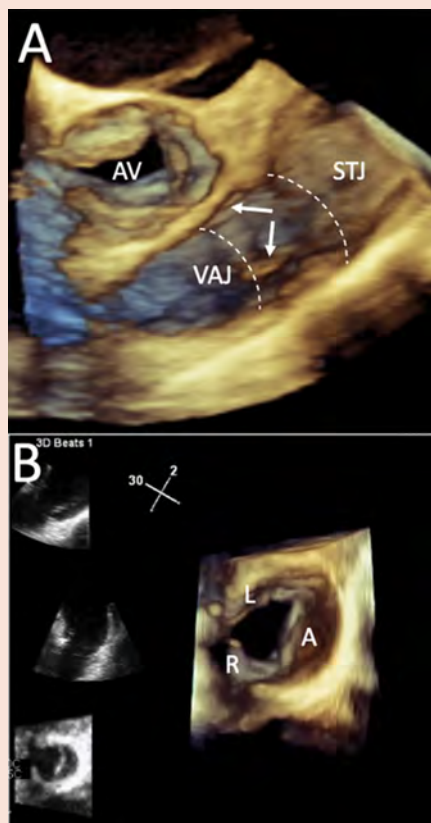
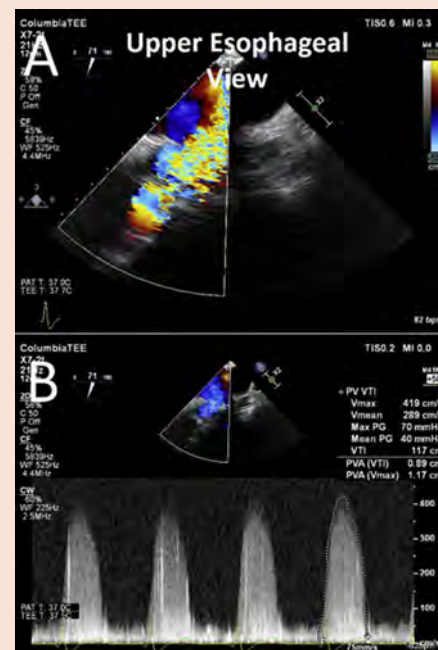
**Three-Dimensional Echocardiography.** Because the TV and tensor apparatus anatomy is highly variable,<sup>86,91,92</sup> understanding the complex anatomy has been significantly advanced using 3D imaging.<sup>93–96</sup> Three-dimensional echocardiography has improved imaging accuracy and identification of the number and location of the tricuspid leaflets<sup>89</sup> and associated anatomic components of the TV complex, thus obviating the need for mental reconstruction of multiple 2D planes.<sup>12</sup> Lang *et al.*<sup>11</sup> suggested a standardized imaging display



**Figure 21** Anatomy of the PV. **(A)** Pulmonic root (red box) complex on CT with magnified image **(B)**, pulmonic root between the white dashed lines. **(B)** Sinotubular junction (STJ), pulmonary sinuses, PV leaflets, crown-shaped annulus (red lines), interleaflet triangles (ILT), and ventriculoarterial junction (VAJ). An ME RV inflow-outflow imaging plane is shown in panel **C** with associated 3D volume in panel **D**. Gross anatomy of the PV with left, right, and anterior leaflets **(E)** can be correlated with the 3D multiplanar view of the PV in panel **F**. A, Anterior; Ao, aorta; RA, right atrium.

**Table 5** PV imaging protocol**Imaging level: ME/UE view 45°–60°****Acquisition protocol:**

- ME RV inflow-outflow view (with AV en face) should show tricuspid inflow extending to the infundibular outlet septum and RVOT. Both the TV and PV are seen.
- Withdrawal of the probe to the UE view while maintaining good contact with the esophagus demonstrates the supra-avalvular region, branch PAs, and may improve leaflet visualization.

**Planar imaging****Volumetric imaging****Functional imaging**

- A. From the ME imaging plane the subpulmonary region is best demonstrated. The valve leaflets may also be seen and the RVOT is measured for calculation of right ventricular stroke volume.
- B. The high esophageal position will demonstrate the valve, supra-avalvular region, main, and oftentimes branch PAs.

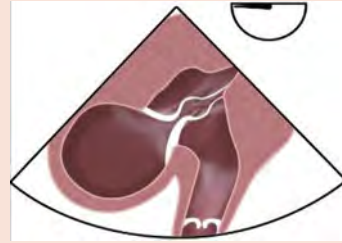
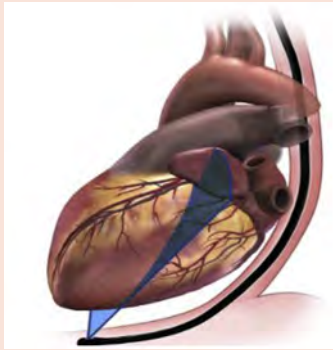
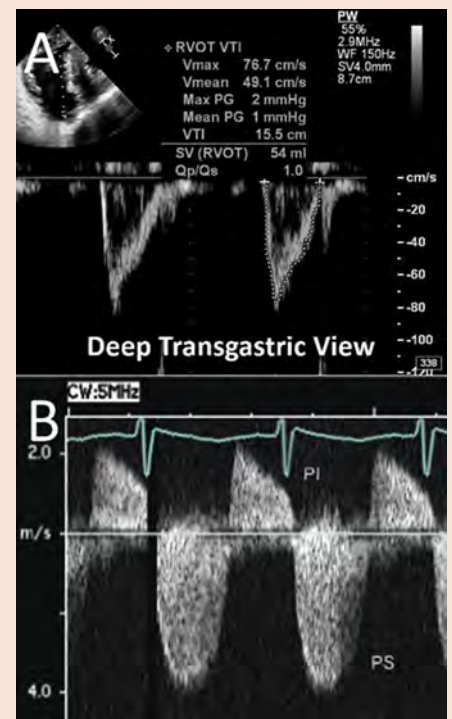
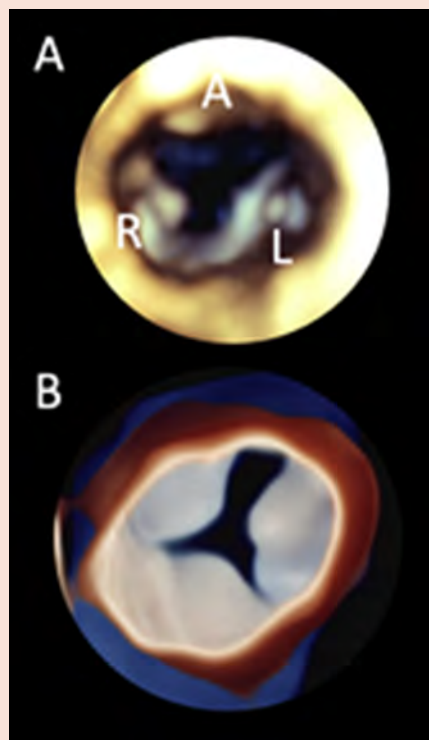
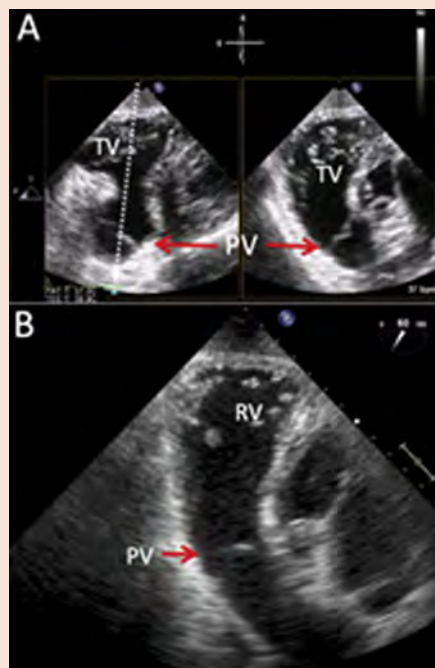
- A. Three-dimensional imaging is best achieved from the ME or higher position that optimizes visualization of the PV complex including leaflets (arrows), VAJ, and STJ.
- B. Three-dimensional en face imaging best demonstrates leaflet morphology and configuration.

- A. UE color Doppler imaging is useful for assessing both stenotic and regurgitant PV lesions. In this case of prosthetic PS, turbulent systolic color flow is easily imaged.
- B. UE views may align the ultrasound beam with flow, and CW Doppler can be performed.

*(Continued)*

**Table 5** (Continued)**Imaging level: TG 0-60°****Acquisition protocol:**

- If the LVOT is visualized, leftward rotation of the probe will display the RVOT.
- The inflow and outflow of the right ventricle are demonstrated.

**Planar imaging****Volumetric imaging****Functional imaging**

- A. Biplane imaging at 0°–20° shows a well-expanded subpulmonary region. The leaflets are frequently difficult to visualize.
- B. Imaging at 40°–60° demonstrates the entirety of the RVOT. Both of these positions provide ideal angulation for spectral Doppler interrogation.

- A. When TG images show the valve clearly, 3D imaging can be performed. However, volumetric imaging is often hindered by the far-field location of the RVOT and PV.

- A. PW Doppler at the level of the PV annulus from TG views can be used for calculation of the RVOT stroke volume.
- B. If the ultrasound beam is well aligned with flow, CW Doppler should be performed to image the systolic flow and, when present, the diastolic (regurgitant) flow.

A, Anterior leaflet; Ao, aorta; L, left leaflet; LA, left atrium; LPA, left PA; MPA, main PA; PG, pressure gradient; PVA, PV area; PW, pulsed-wave; Qp/Qs, ratio of pulmonary flow to systemic flow; R, right leaflet; RA, right atrium; RPA, right PA; RV, right ventricle; STJ, sinotubular junction; SV, stroke volume; VAJ, ventriculoarterial junction; Vmax, maximum velocity; Vmean, mean velocity; VTI, velocity-time integral.

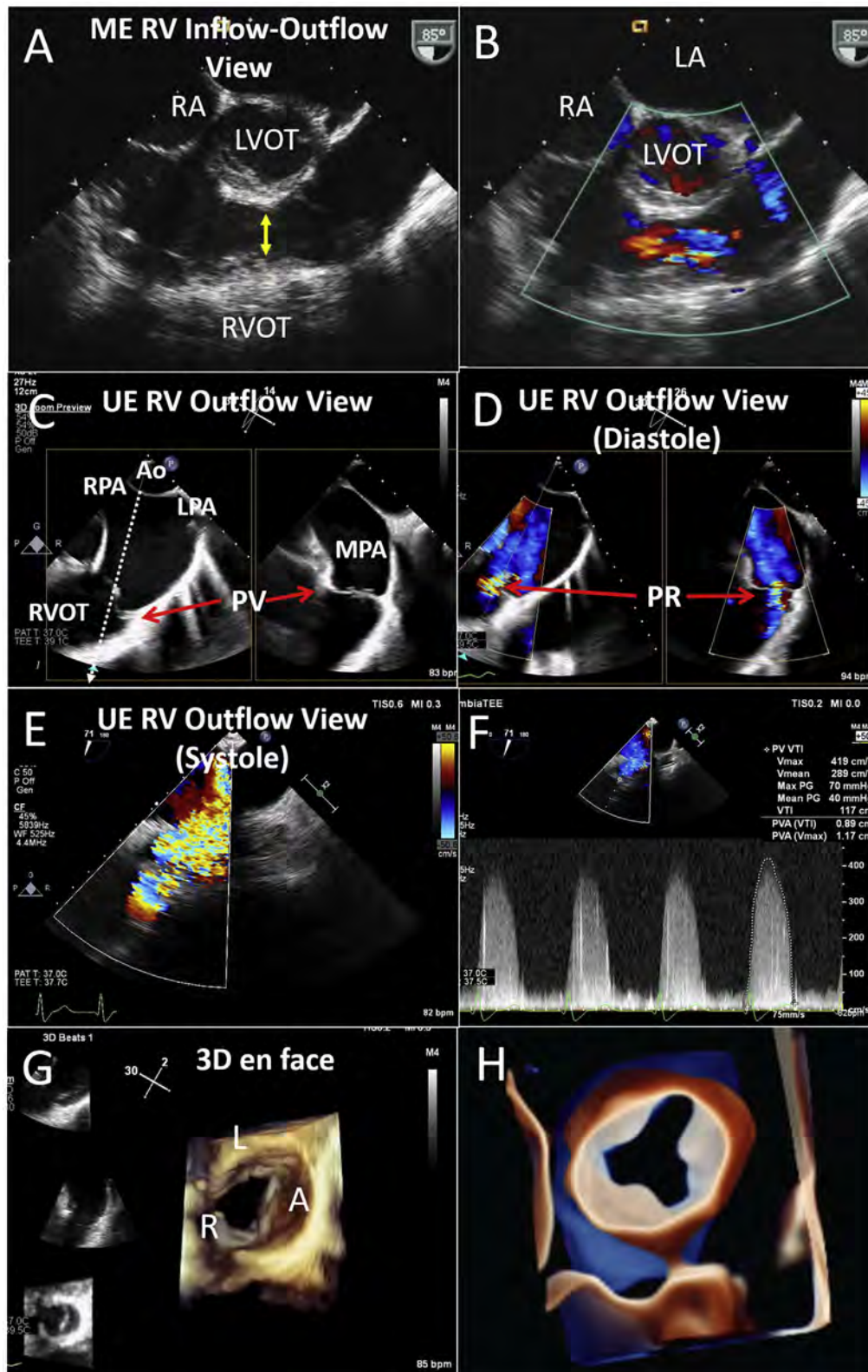


**Figure 22** PV imaging. The PV can be imaged from both ME and UE levels. From the ME RV inflow-outflow view, the RVOT is well imaged and in this case exhibited dynamic subpulmonic obstruction (yellow double arrow, **A**) with turbulent flow on color Doppler (**B**). From the UE RV outflow view at a transducer angle of 45° to 60°, the PV (red arrows, **C**) is imaged without intervening left or right heart structures. Given the alignment of the insonation beam, Doppler for PR (red arrows, **D**) or PS (**E**, **F**) can be performed. This level of imaging may provide optimal imaging windows for 3D rendering of the PV (**G**, **H**). A, Anterior cusp; Ao, aorta; L, left cusp; LA, left atrium; LPA, left PA; MPA, main PA; P, posterior cusp; PG, pressure gradient; PVA, PV area; R, right cusp; RA, right atrium; RPA, right PA; RV, right ventricle; S, septal leaflet; Vmax, maximum velocity; Vmean, mean velocity; VR, velocity ratio; VTI, velocity-time integral.

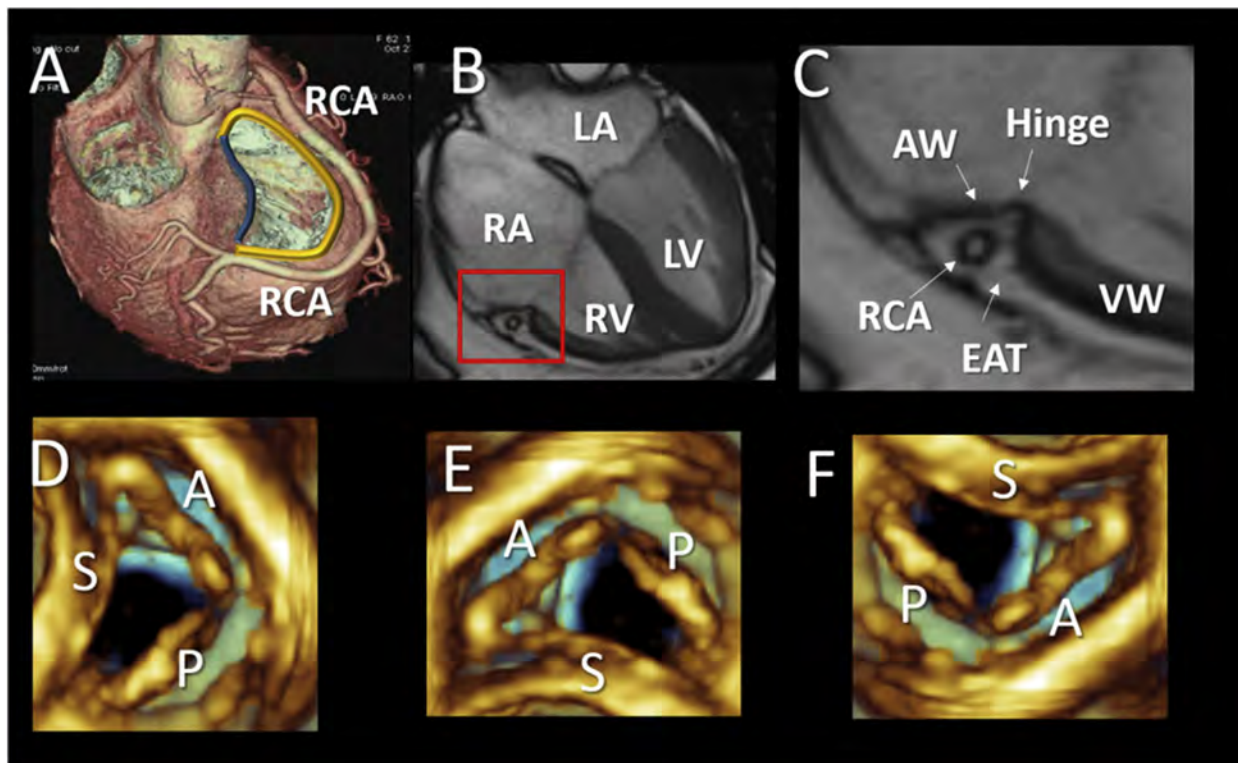


**Figure 23** TV anatomy. **(A)** Computed tomographic volume rendering showing the mural (yellow band) and septal (blue band) segments of the tricuspid annulus. The right coronary artery (RCA) encircles the entire mural segment. On cardiac magnetic resonance imaging **(B)** the atrioventricular groove (red box) is magnified in panel **C**, allowing visualization of all the components of the tricuspid annulus: the hinge, the atrial wall (AW), the ventricular wall (VW), and the epicardial adipose tissue (EAT). Three-dimensional trans-thoracic echocardiographic images of tricuspid leaflets from the right ventricular perspective are shown in the anatomic **(D)**, surgeon's **(E)**, and bicaval **(F)** orientations. A, Anterior leaflet; LA, left atrium; LV, left ventricle; P, posterior leaflet; RA, right atrium; RV, right ventricle; S, septal leaflet.

for the en face view of the TV with the IAS placed inferiorly (at the 6 o'clock position) regardless of the atrial or ventricular orientation (Figure 25B). From all imaging levels and views, this orientation requires an additional z-plane rotation of the image and could lead to significant confusion in the setting of marked leaflet variability. Many interventional echocardiographers do not perform the final rotation, with the resulting TV en face view mimicking the leaflet orientation of a SAX TG view (Figure 25F), with the interventricular septum on the right side of the screen and the aorta located at the 5 o'clock position.<sup>90</sup> In either situation, using the adjacent anatomy to identify leaflets allows consistent identification of the leaflets with the aorta adjacent to the anteroseptal commissure and the coronary sinus adjacent to the posteroseptal commissure.

If 3D imaging is adequate to see the leaflet tips, measurement of leaflet lengths, coaptation gaps, and color Doppler vena contracta width or area at the site of malcoaptation can be performed using 3D multiplanar reconstruction (either real time or offline). Annular measurements (linear dimensions, area, or perimeter) for device sizing or quantitation of diastolic stroke volume are also performed on multiplanar reconstruction. Of note, when calculating the diastolic stroke volume, a planar annular measurement should be used<sup>97</sup> because quantifying the volume of a column of blood is performed. The TV annulus in normal patients is nonplanar with dynamic variability during the cardiac cycle, and measurement of this complex shape may require special software or offline use of the MV quantitation software packages.<sup>96,98</sup>

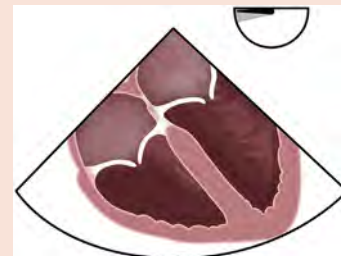
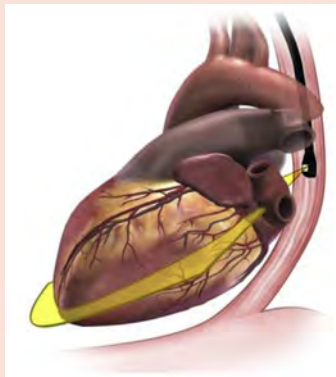
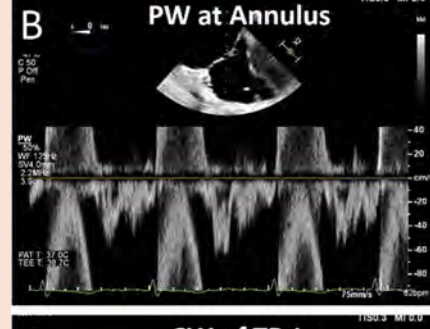
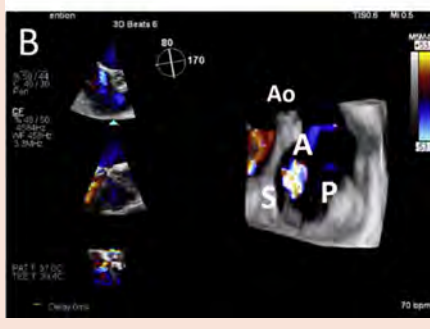
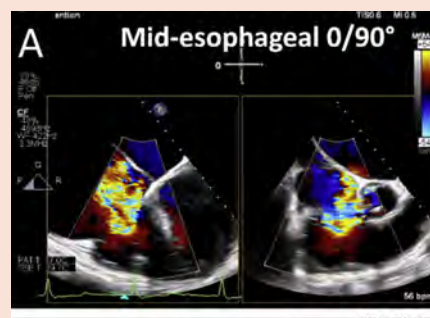
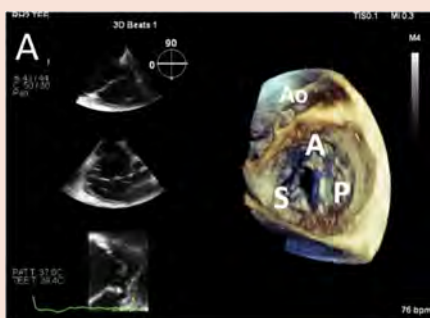
**Grading the Severity of TR.** Grading the severity of TR has been described in the ASE guidelines<sup>6</sup> as well as the European Association of Echocardiography guidelines and focuses on assessment by TTE.<sup>99</sup> Nonetheless, TEE imaging can be used to assess many of the parameters (Figure 25H). It is essential to use a multiparametric method for determining severity, as no single parameter has adequate specificity. Multiple investigators are attempting to refine<sup>85,100,101</sup> and validate<sup>102-106</sup> newer methods and criteria for quantitation of TR.

**3. TV Stenosis.** The most common etiologies of tricuspid stenosis are rheumatic disease, congenital abnormalities, metabolic or enzymatic abnormalities (e.g., carcinoid syndrome), and active infective endocarditis.<sup>107</sup> Rheumatic involvement of the TV does not typically occur without involvement of left-sided valves.<sup>69</sup> Similar to rheumatic MV disease, there is fibrous thickening of valve leaflets with fusion of commissures and thickening, shortening, and fusion of the chordae tendineae. TV stenosis can develop secondary to implantable cardiac electronic devices when endocardial leads cause injury to the valve, initiating a cascade of inflammatory response and fibrosis.<sup>108</sup> Percutaneous balloon valvuloplasty for native TV stenosis has been reported, but surgery is the preferred intervention.

**4. Primary TR.** A recent prospective cohort study showed that primary TR accounted for 7.4% of cases ( $n = 157$ ), whereas secondary TR accounted for 92.6% of cases ( $n = 1,964$ ). In the group with

**Table 6** TV imaging protocol**Imaging level: ME view 0°****Acquisition protocol:**

- From the ME four-chamber view focused on the MV (0° mechanical rotation), rotating the probe clockwise will center the TV in the imaging plane.
- Using right flexion may help center the TV and reduce interference from left heart structures.

**Planar imaging****Volumetric imaging****Functional imaging**

- A. Four-chamber view, which usually images the septal leaflet (arising from the septum) and typically the anterior leaflet (adjacent to the right atrial appendage).
- B. Simultaneous biplane imaging with the orthogonal inflow-outflow view.

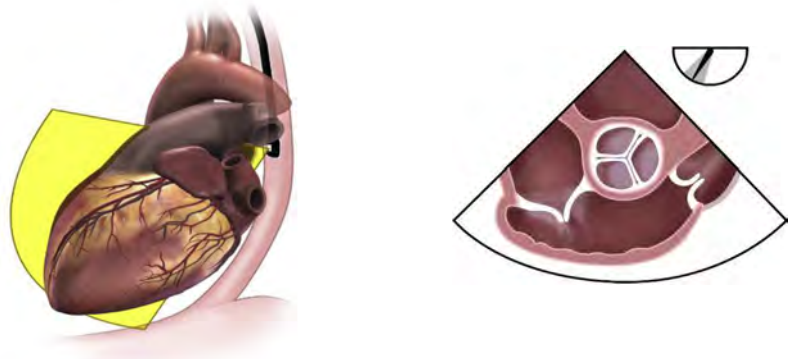
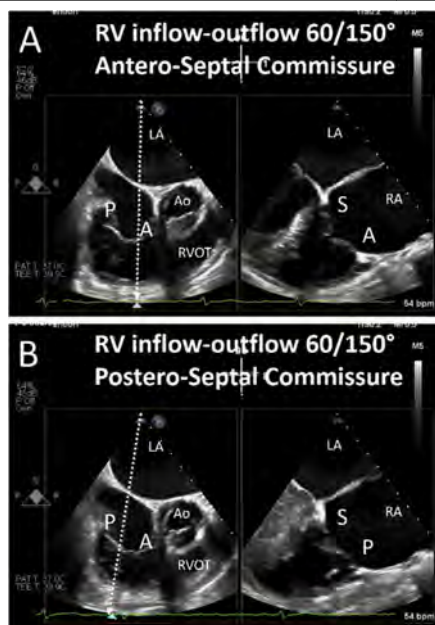
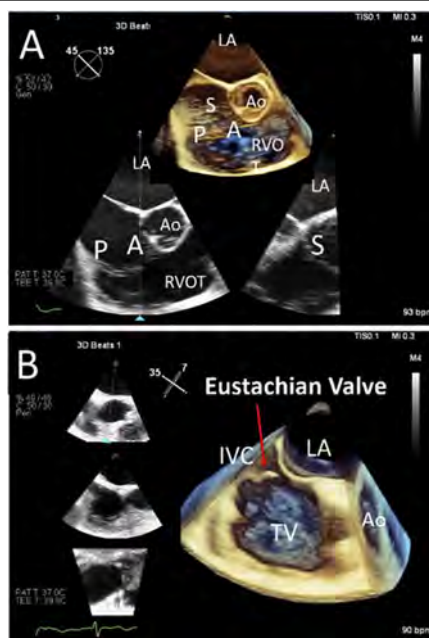
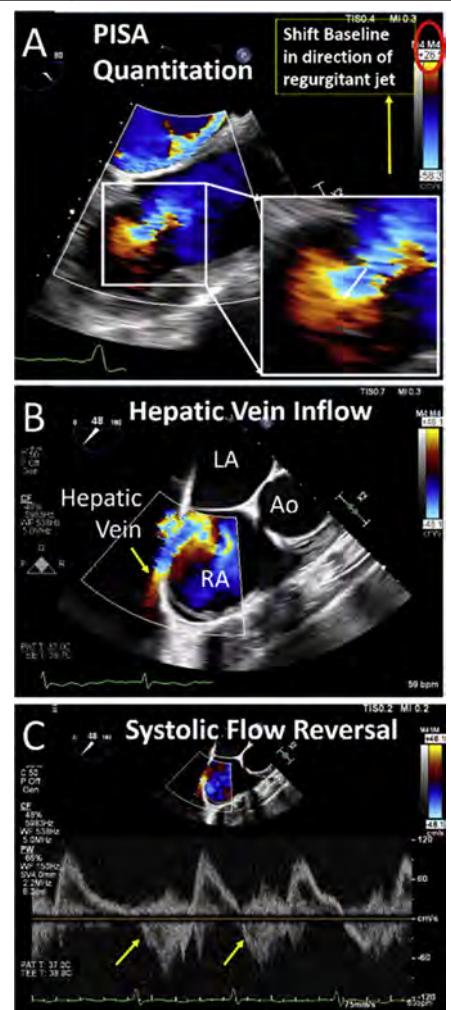
- A. Three-dimensional en face imaging can be performed using a user-defined volume, from any 2D imaging plane that optimizes visualization of the TV.
- B. Three-dimensional color Doppler (multibeam acquisition) can be performed to improve temporal and spatial resolution.

- A. Color Doppler biplane helps define the shape of the regurgitant orifice.
- B. PW Doppler at the annulus is used to quantify TR.
- C. CW Doppler is important to assess TR severity and PA pressures.

(Continued)

**Table 6** (Continued)**Imaging level: right ventricular inflow-outflow view 60°****Acquisition protocol:**

- Keeping the TV in the center of the imaging sector, forward mechanical rotation to  $\sim 60^\circ$  results in the right ventricular inflow-outflow view, also known as the TV commissural view.

**Planar imaging****Volumetric imaging****Functional imaging**

- A. Biplane image adjacent to the aorta and thus imaging the anterior and septal leaflet in the orthogonal plane.  
B. Biplane image adjacent to the posterolateral wall and thus imaging the posterior and septal leaflet in the orthogonal plane.

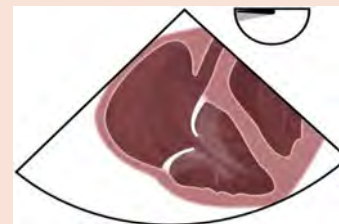
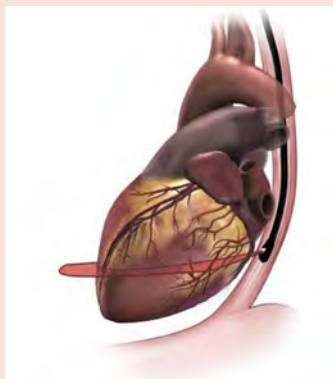
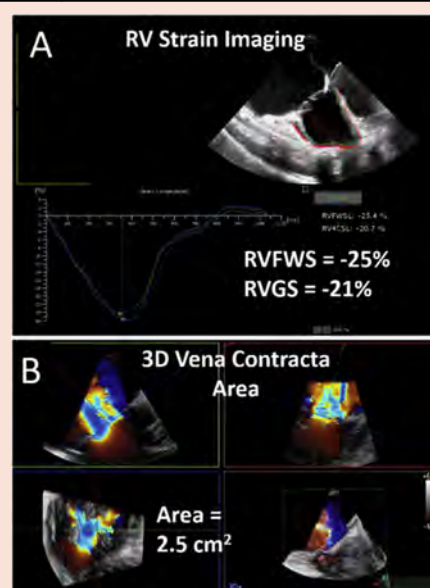
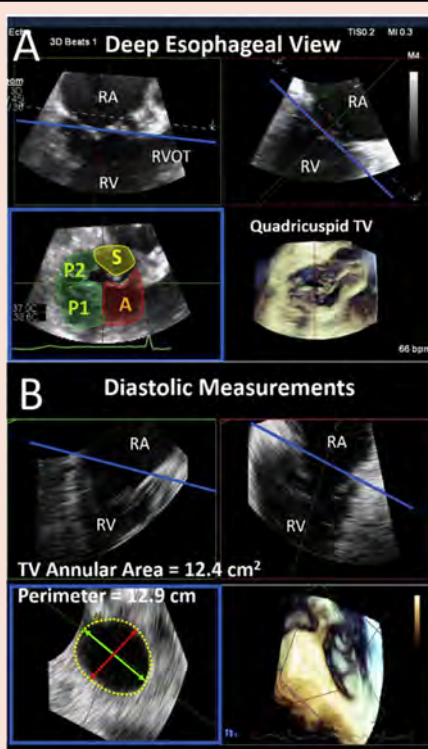
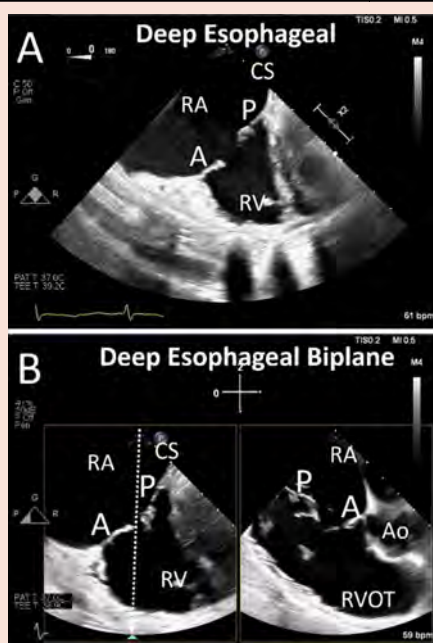
- A. Three-dimensional live imaging (narrow volume) may be particularly useful to assess anatomy with high temporal resolution.  
B. Zoom 3D from a bicaval view allows imaging of the IVC inflow and a prominent eustachian valve (which can obstruct catheter manipulation).

- A. Shift the color Doppler baseline in the direction of flow to obtain a PISA shell and measure the PISA radius.  
B. Color Doppler of the hepatic vein should allow alignment of the ultrasound beam for more accurate assessment of reversal of hepatic vein systolic flow.  
C. PW Doppler of the hepatic vein shows holosystolic flow reversal.

(Continued)

**Table 6** (Continued)**Imaging level: DE views****Acquisition protocol:**

- Careful insertion of the TEE probe into the distal esophagus brings the probe closer to the tricuspid annulus; frequently there is no LA seen, and only the RA and coronary sinus with the orthogonal view imaging the RVOT.

**Planar imaging****Volumetric imaging****Functional imaging**

- A. From DE imaging planes (near the diaphragm), left heart structures may be avoided; because imaging is near the diaphragm often the anterior and posterior leaflets are seen.
- B. Biplane imaging shows the DE inflow/outflow view in the orthogonal plane.

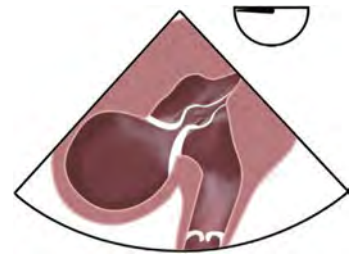
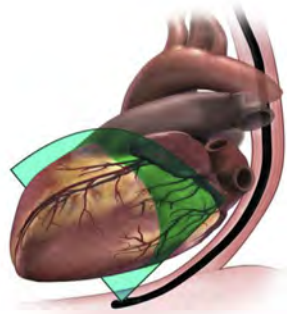
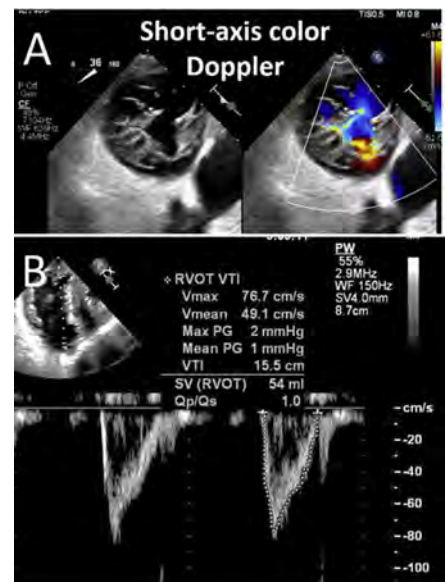
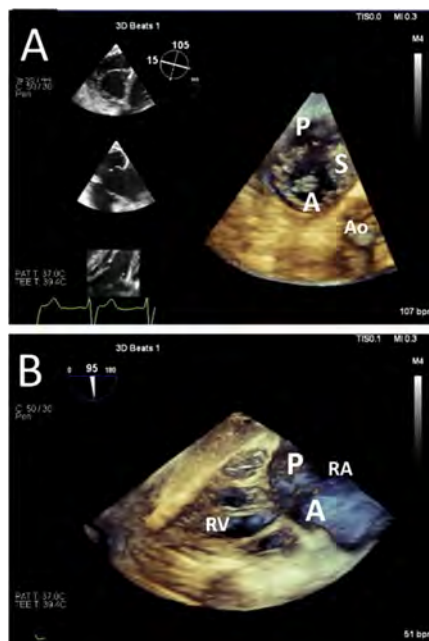
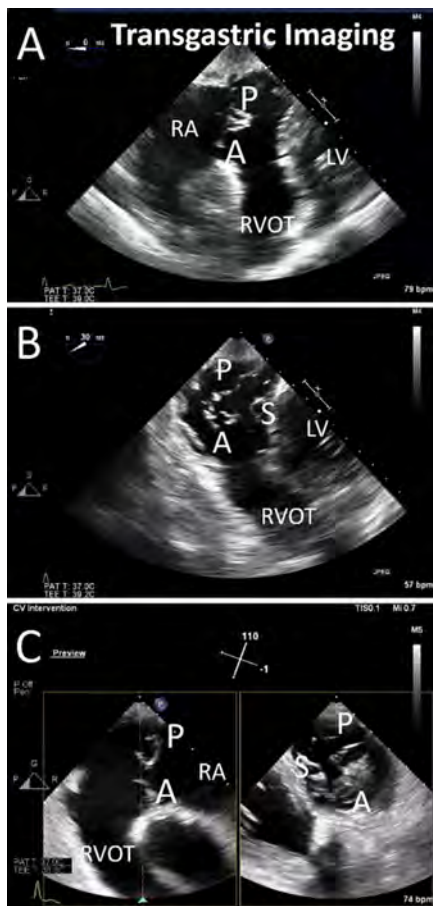
- A. Real-time multiplanar reconstruction allows rapid reorientation of the two orthogonal long-axis views (*top right and top left*), resulting in a SAX view of this quadricuspid valve (*lower left*) and a 3D en face view for orientation. According to a proposed nomenclature, the anterior papillary muscle is used to identify the anterior leaflet (A) and posterior leaflets (P1 and P2). The septal leaflet (S) attaches to the interventricular septum.
- B. Offline MPR can be used to measure the tricuspid annulus area, perimeter or dimensions (*blue plane*) at any point in the cardiac cycle.

- A. Right ventricular function should be assessed by the guideline-recommended methods (e.g., TAPSE, fractional area change) or newer methods (strain imaging).
- B. Quantitative Doppler and 3D vena contracta area should be performed.

(Continued)

**Table 6** (Continued)**Imaging level: TG****Acquisition protocol:**

- With both right and anteflexion and rotating the probe clockwise and rotating the TV in the imaging plane, a two-chamber inflow-outflow view of the right heart is obtained.

**Planar imaging****Volumetric imaging****Functional imaging**

- A. From the TG level at 0° mechanical rotation, with right and anteflexion, the inflow-outflow view of the right heart can be imaged. Biplane imaging aligning the orthogonal plane at the tips of the leaflet can be performed.
- B. At 20°–60° mechanical rotation, typically without right flexion and only mild anteflexion (to visualize the tips of the leaflets), a single-plane SAX view is obtained.
- C. At a mechanical rotation of 90°–120°, the reverse inflow-outflow right ventricular view is obtained; here biplane imaging allows SAX imaging of the leaflet tips.

- A. Because the TV is imaged in the near field, 3D user-defined volumes can be obtained with adequate temporal resolution (in this example 12 Hz) with multibeat spliced images.
- B. Imaging the complex and highly variable subvalvular apparatus may require 3D imaging.

- A. Color Doppler imaging of the regurgitant orifice (at the leaflet tips) identifies the location and shape of the regurgitant orifice.
- B. PW Doppler of the RVOT (or LVOT, when adequate RVOT views cannot be obtained) should be performed to calculate forward stroke volume.

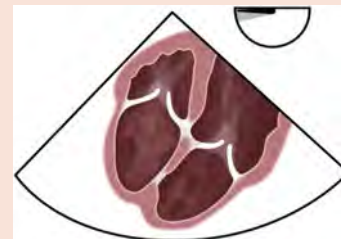
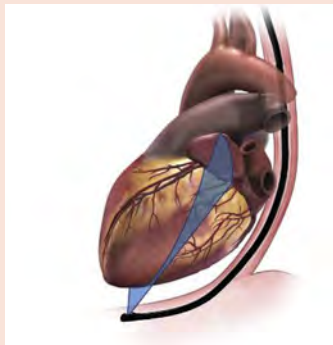
(Continued)

Table 6 (Continued)

## Imaging level: DT

## Acquisition protocol:

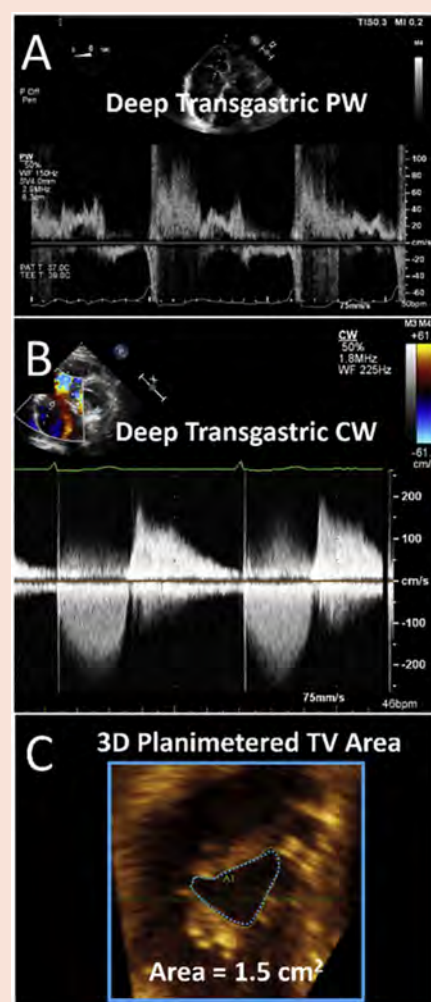
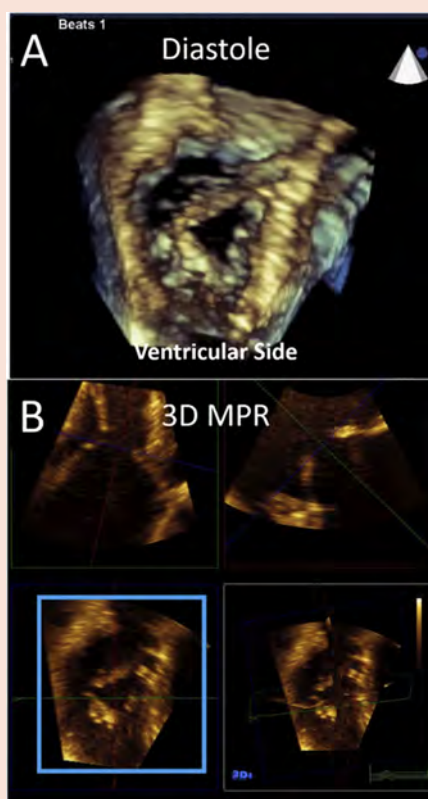
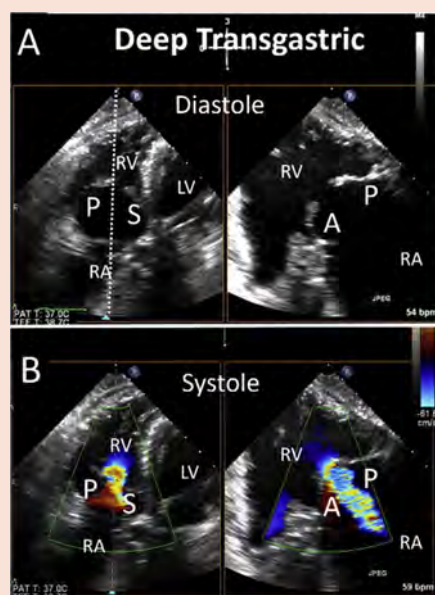
- Advancing the TEE probe further into the stomach along with rightward anterior flexion produces a DT view of the TV, which frequently can be used to assess TV function using Doppler parameters.



## Planar imaging

## Volumetric imaging

## Functional imaging



A. From the DT position, the probe is near the apex of the right ventricle with the tricuspid annulus more perpendicular to the ultrasound beam. In this example of a patient with rheumatic tricuspid stenosis, prominent doming of the leaflets is seen in diastole.

A. The DT view can be used to acquire 3D imaging of the TV.  
B. 3D multiplanar reconstruction (MPR) is used to identify the tricuspid orifice area at the tips of the leaflets (blue box).

A. PW Doppler at the annulus is used to perform quantitative Doppler calculations of diastolic stroke volume.  
B. The most complete and highest systolic and diastolic CW Doppler velocities may be obtained from these views.

(Continued)

Table 6 (Continued)

## Imaging level: DT

B. With the ultrasound beam aligned with flow, a comprehensive Doppler assessment can be made.

C. From any well-imaged 3D volume, quantitative assessment of valve or annular area can be made using online or offline measurement tools. In this example of tricuspid stenosis, the area is significantly reduced.

A, anterior leaflet; Ao, aorta; CS, coronary sinus; LA, left atrium; LV, left ventricle; LVOT, left ventricular outflow tract; MPR, multiplanar reconstruction; P, posterior leaflet; P1, posterior leaflet adjacent to anterior leaflet; P2, posterior leaflet more posterior to P1; PG, pressure gradient; PW, pulsed-wave; Qp/Qs, ratio of pulmonary flow to systemic flow; RA, right atrium; RAA, right atrial appendage; RV, right ventricle; RVFWS, right ventricular free wall strain; RVGS, right ventricular global strain; S, septal leaflet; SV, stroke volume; TAPSE, tricuspid annular plane systolic excursion; Vmax, maximum velocity; Vmean, mean velocity; VR, velocity ratio; VTI, velocity-time integral.

primary TR, the most frequent etiology was cardiac implantable electronic devices (66.5%), representing 5% of all patients with TR.<sup>109</sup> Potential mechanisms of cardiac implantable electronic device-mediated interference of the TV apparatus include lead entrapment in the subvalvular apparatus, leaflet perforation, lead impingement on a TV leaflet, and lead adherence to the TV leaflet. An overview of how to diagnose cardiac implantable electronic device-mediated interference on echocardiography has been recently published.<sup>110</sup> The next most common etiology of primary TR was myxomatous disease.<sup>109</sup> Although some degree of prolapse is common for the nonplanar TV, a diagnosis of TV prolapse is typically reserved for excessive billowing into the right atrium associated with redundancy of the tricuspid leaflets. This abnormality is seen in 20% of patients with concomitant MV prolapse. Ebstein anomaly, a congenital valve lesion, defined as  $>8$  mm/m<sup>2</sup> apical displacement of the septal leaflet, should be differentiated from other primary causes of TR: the exaggerated displacement of the valve annulus and resultant “atrialization” of the basilar RV currently preclude transcatheter annular repair or valve replacement.

**5. Secondary TR.** Secondary TR is much more common than primary disease and can be categorized either by the etiology (disease process) or mechanism (morphologic abnormality of the tricuspid apparatus).<sup>86</sup> If classified by underlying disease, secondary TR can be associated with (1) left-sided heart disease (valve disease or LV dysfunction), (2) pulmonary hypertension (either precapillary or post-capillary), (3) RV dilatation or dysfunction (myocardial disease or RV ischemia or infarction), and (4) diseases associated with isolated atrial dilatation (atrial fibrillation and heart failure with preserved ejection fraction). Morphologic classification of secondary TR includes (1) ventricular functional TR, related to RV dilatation or dysfunction, and (2) atrial functional TR (previously known as idiopathic or isolated functional TR) associated with right atrial and tricuspid annular dilatation or dysfunction. The common TV morphologic abnormalities associated with ventricular functional TR include (1) RV dilatation resulting in a more spherical ventricle, with or without dysfunction; (2) tethering of the tricuspid leaflets in the setting of papillary muscle displacement (Carpentier class IIIb); and (3) mild dilation of the tricuspid annulus with or without right atrial dilatation. TV morphologic abnormalities associated with atrial functional TR include (1) severe dilatation and dysfunction of the right atrium and tricuspid annulus, (2) minimal tethering of the tricuspid leaflets with otherwise normal leaflet motion (Carpentier class I), and (3) dilatation of the RV base with preservation of the conical RV shape.<sup>111</sup>

The superior vena cava (SVC) and inferior vena cava (IVC) are important anatomic structures providing easy access for transcatheter approaches to the TV and thus should be comprehensively imaged. The IVC is the largest vein in the human body, with a normal size usually  $<21$  mm.<sup>8</sup> The SVC is often irregular in shape on cross-sectional images with a normal range for the major axis of 1.5 to 2.8 cm and a minor axis range of 1 to 2.4 cm. Although in young patients the outlets of the SVC and IVC face each other, lateralization and convergence of the veins occurs in older subjects<sup>112</sup> that may have significance for device or guide catheter positioning.

### G. Assessment of the LAA

Given the risk associated with surgical LAA ligation, percutaneous LAA occlusion and exclusion devices were approved by the US Food and Drug Administration for the prevention of stroke in patients with atrial fibrillation who are intolerant of long-term systemic anticoagulation and with CHA<sub>2</sub>DS<sub>2</sub>-VASc scores  $\geq 2$ .<sup>113</sup> These devices require a careful multimodality approach with a specific focus on echocardiography for preprocedural device implantation evaluation.

**1. Anatomy of the LAA.** The LAA is a fingerlike projection extending from the left atrium with a well-defined orifice. In most hearts, the LAA extends between the anterior and lateral walls of the left atrium with its tip by the pulmonary trunk or the main stem of the left coronary artery or circumflex artery.<sup>114</sup> Internally, the left lateral ridge (“Coumadin ridge”) separates the orifice of the LAA from the left upper pulmonary vein, while the smooth wall of the left atrium separates the orifice from the mitral annulus (Figures 26A–26C).<sup>115</sup>

The LAA is made up of the ostium, neck, body, and apex.<sup>116</sup> Although the walls of the LAA are relative smooth, the apex can be made up of parallel muscle bundles (pectinates, Figure 26B) that can be mistaken for thrombi.<sup>117</sup> The apex itself can be comprised of several lobes or visible outpouchings from the main tubular body of the LAA. An increase in the number of lobes has been reported to be associated with the presence of thrombus independent of other clinical risk factors.<sup>118</sup> There are four morphologic variants or types of LAA (Figure 26D–G), with “chicken wing” being the most common, followed by “cactus,” “windsock,” and “cauliflower.”<sup>119</sup> The cauliflower morphology is most often associated with embolic events.<sup>119</sup>

**2. General Imaging Protocol for the LAA (Table 7).** A comprehensive TEE evaluation of the LAA should include identification of the morphology and function of the LAA; identification of number and location of accessory lobes; identification and measurement of

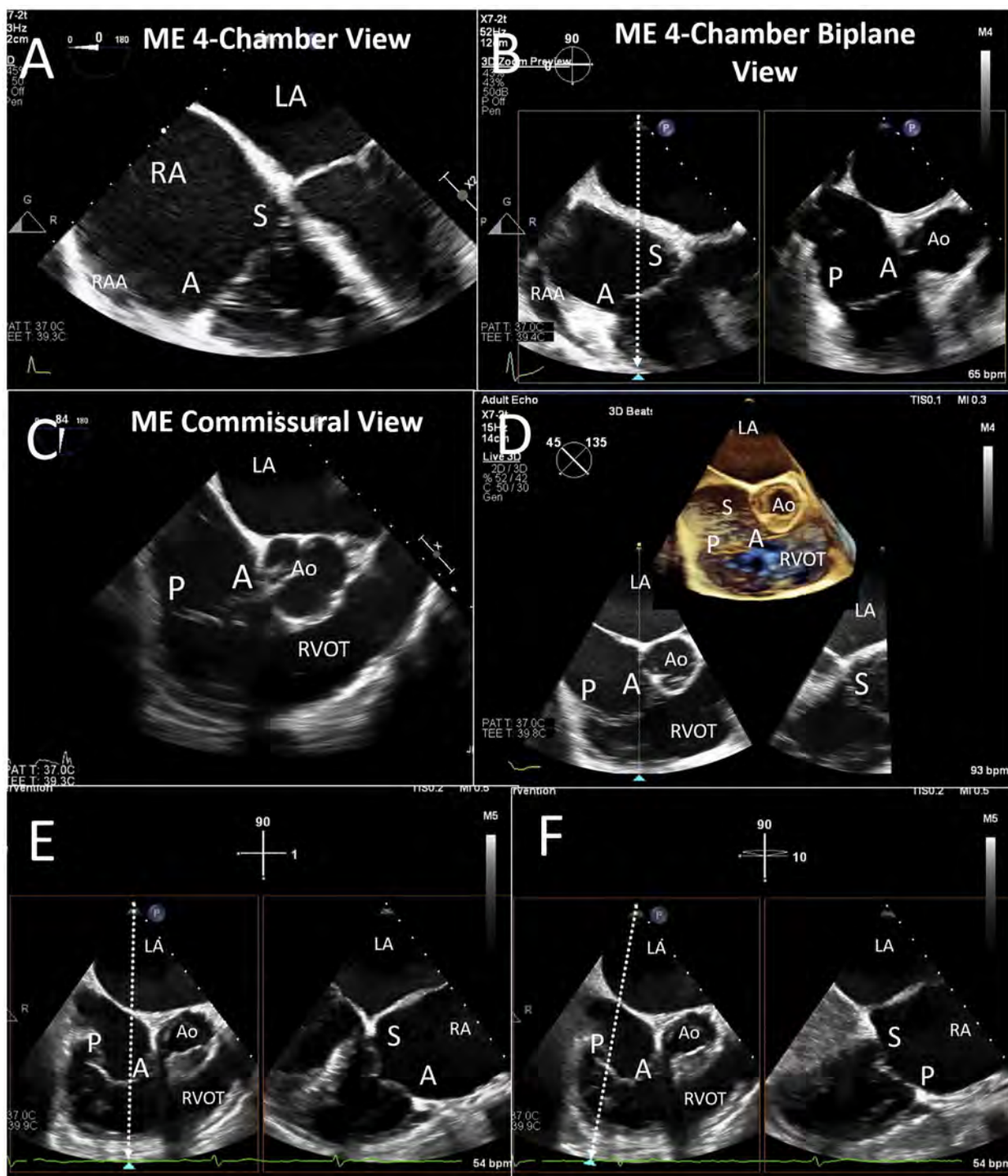


**Figure 24** ME imaging of the TV. From the ME level of imaging, the TV is in the far field, and the annular plane cannot be aligned perpendicular to the ultrasound beam (**A**). Nonetheless, right atrial and right ventricular (RV) size and function can be assessed. Biplane imaging (**B**) is essential because the three leaflets of the valve cannot be imaged at this level from a single 2D imaging plane. The RV inflow-outflow view (**C**) is the equivalent of the MV commissural view. Using live 3D (**D**), it is clear that the septal leaflet (S) is in the far field and performing a “sweep” from the aorta (anterior-septal commissure; **E**) to the posterolateral wall (posterior-septal commissure; **F**) will typically image the most common regions of leaflet malcoaptation. A, Anterior leaflet; Ao, aorta; LA, left atrium; LV, left ventricle; P, posterior leaflet; RA, right atrium; RAA, right atrial appendage.

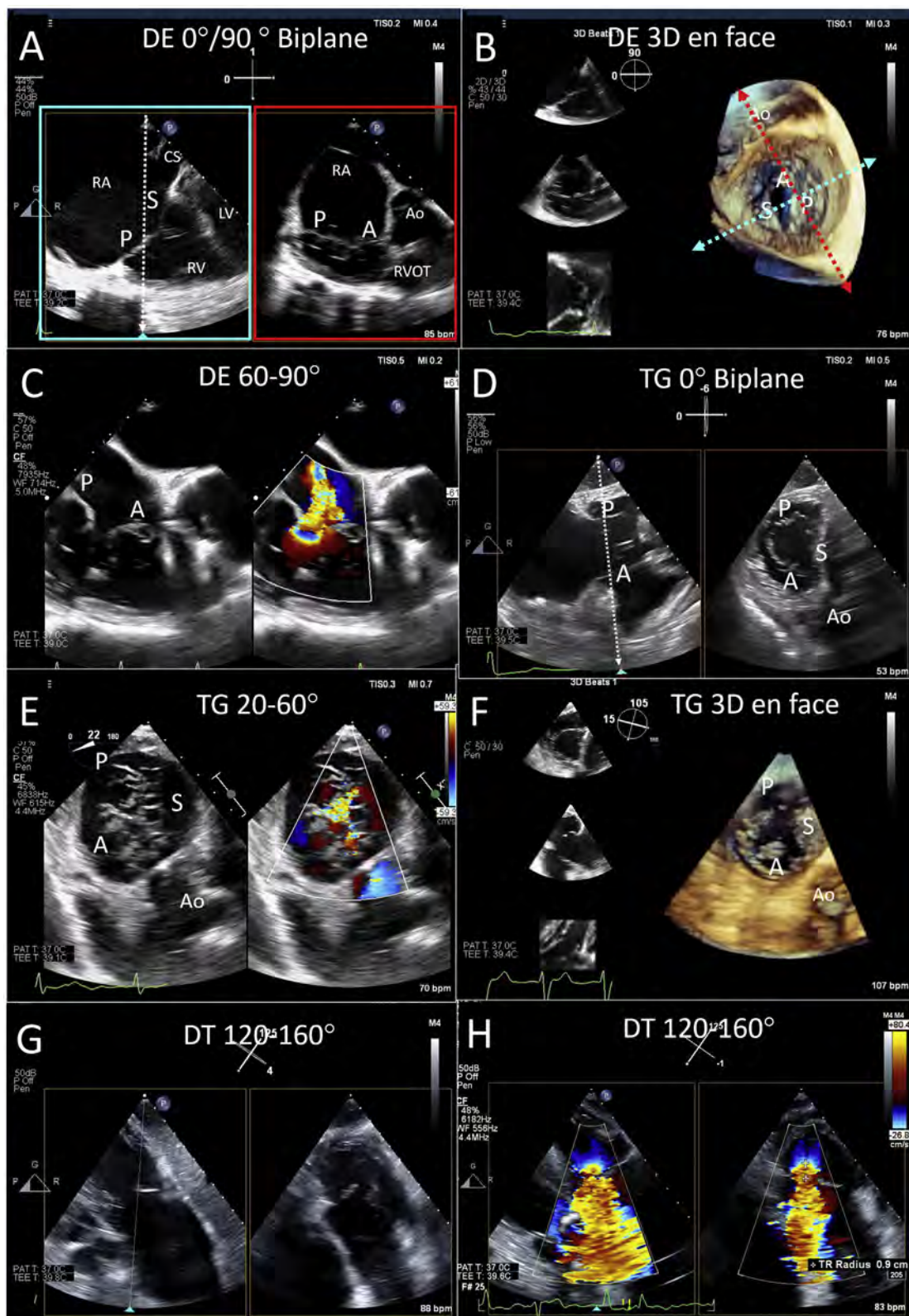


**Figure 25** DE, TG, and DT views of the TV. Careful advancement of the TEE probe into the distal esophagus brings the probe closer to the tricuspid annulus for DE views (**A–C**). From the 0° rotation, the left atrium is often not seen, and only the right atrium (RA), right ventricle (RV), and coronary sinus (CS) are visualized (*blue box*), while the orthogonal view demonstrates the RVOT (*red box*, **A**). (Figure legend continued at the bottom of the next page).

the neck, body, and apex in standard imaging planes; imaging of adjacent structures (e.g., left atrium, right atrium, IAS, pulmonary veins, and MV); evaluation of the IAS (e.g., atrial septal aneurysm, patent foramen ovale [PFO]); documentation of pericardial effusion; and presence of spontaneous echocardiographic contrast (“smoke”), sludge, or thrombus (Figure 26H–26K).

**ME Views.** Measurement and assessment of the LAA landing zone and LAA depth are crucial for these procedures. On 2D TEE imaging, the LAA is measured from the 0°, 45°, 90°, and 135° views (Figure 27).<sup>120</sup> Of note, new iterations of commercial devices are not only shorter in length but have a conformable shape; thus, measurements of the usable length of the LAA may not be orthogonal to the LAA orifice. Manipulation of the lateral plane can help in identifying the number and position of LAA lobes, as can rotating the probe from side to side when it is at 90°. It is also important to note the shape of the LAA, number of lobes, and the lobe positions relative to the ostium.

**Three-Dimensional Echocardiography.** Several LAA percutaneous occlusion devices rely on TEE assessment of the landing zone. Because of the difficulty in obtaining an adequate view using 2D imaging, 3D TEE imaging is frequently used to determine the diameter and depth of the landing zone, although newer iterations of the currently available intracardiac LAA occlusion device are not as limited by depth as prior iterations. Using multiplanar reconstruction with alignment of orthogonal planes at the proposed landing zone, LAA depth and diameter of the landing zone can be measured (Figure 28D). Three-dimensional imaging may be particularly useful before delivery of an epicardial LAA suture exclusion device, which must be maneuvered around the body of the LAA to snare the appendage epicardially (Figures 28E and 28F).<sup>121</sup>

## H. Assessment of the IAS

ASD is the third most common congenital heart defect.<sup>122</sup> Secundum ASDs, located within the fossa ovalis, are the most common and are often amenable to percutaneous device closure, in contrast to the other ASD types. Preintervention TEE assessment of the secundum ASD is typically performed in patients already identified to meet closure indications: right heart dilatation, ratio of pulmonary flow to systemic flow > 1.5, absence of cyanosis, and absence of irreversible or severe pulmonary hypertension. Severe pulmonary hypertension is defined as PA systolic pressure greater than one half systemic pressure and pulmonary vascular resistance greater than one third systemic.<sup>72</sup>

**1. Anatomy of the IAS.** Three components of the IAS can be identified during in utero development: the septum primum, septum secundum, and atrioventricular septum. The fossa ovalis develops from the

embryonic septum primum, forms the central portion of the IAS (Figures 29A–29D), and is the primary location for transeptal puncture (Figures 29E and 29F). The fossa ovalis is surrounded by the septum secundum, an infolding of the atrial roof rather than a true IAS. When this infolding is filled with epicardial fat, it is often referred to as lipomatous septal hypertrophy (Figures 29A–29C), but this is a “false septum,” as the epicardial fat layer is outside the atria.<sup>123</sup> Other important adjacent structures include the aortic root anteriorly, and the venous inflows to the right atrium, namely, the IVC, SVC, and coronary sinus, which are immediately adjacent to the left atrium. The Chiari network and Eustachian valve are normal anatomic variants, frequently present on the right atrial side of the IAS. A PFO may persist in adulthood as an opening between the septum primum and septum secundum, at the anterosuperior aspect of the fossa ovalis.

Secundum ASDs may be single or multiple defects within the thin septum primum (Figure 30A), usually with a well-formed septum secundum. The defects are surrounded by rims of tissue adjacent to the bordering structures of the right atrium. Whereas secundum defects can typically be closed using transcatheter techniques, nonsecundum defects cannot be closed percutaneously.

A primum ASD, also known as partial atrioventricular canal defect (Figure 30B), is an endocardial cushion defect. This lesion results in abnormal atrioventricular valve morphology, including what appears as a cleft of the left atrioventricular valve but is in fact the commissure of a bridging leaflet that attaches to the crest of the interventricular septum and thus lacks the normal apical offset of the TV.<sup>124</sup> The associated ostium primum ASD is bound anteriorly by the atrioventricular valve annulus and is thus not amenable to transcatheter device closure. The cleft in the septal leaflet of the left atrioventricular valve is directed toward the septum and may be accompanied by MR.

Sinus venosus septal defect is a partial or complete absence of the sinus venosus septum and thus not a true defect in the atrial septum. When the communication occurs between one or more of the right pulmonary veins and the SVC and/or posterior wall of the right atrium, it is the superior type (Figure 30C), in contrast to the less common inferior type near the IVC (Figure 30).<sup>125</sup> Anomalous coronary sinus septal defect is the least common and results from partial or complete unroofing of the coronary sinus, with a resultant shunt from the left atrium through the coronary sinus and into the right atrium. Diagnosis of coronary sinus septal defect is challenging, but if there is suspicion on TTE because of right heart and coronary sinus dilatation, TEE imaging should reliably demonstrate the defect.<sup>126</sup>

PFO is not a true deficiency of atrial septal tissue but rather a potential space or separation between the septum primum and septum secundum that occurs in up to 20% to 25% of the population.<sup>127</sup> A growing body of literature currently supports the use of closure

(Figure 25 legend continued from preceding page). Three-dimensional imaging can be performed from any view. (B) En face surgeon’s view, which, similar to the MV en face view, requires a 180° rotation. Many interventional echocardiographers prefer not to perform the final rotation. The DE 60° to 90° view (C) is similar to the ME inflow-outflow view but, given the deeper imaging plane, may visualize the anterior and posterior leaflets, aligning the color jet through this coaptation gap. Advancing the probe past the lower esophageal sphincter into the stomach results in TG views. Using biplane imaging from a TG RV inflow-outflow view (D) or a single-plane SAX view (E) allows 2D SAX imaging of all TV leaflets; the anterior leaflet (A) in the far field, the posterior leaflet (P) in the near field, and the septal leaflet (S) on the right (with aorta [Ao] also in the far field). The resulting 3D en face view mimics this TG SAX view (F). Further advancement of the probe results in the DT views (G), which may allow optimal alignment of the ultrasound beam with the TR jet for Doppler assessment of TR severity; panel H shows a midsystolic biplane still frame with color Doppler shift and measurement of the flow convergence radius (right panel) used for the calculation of effective regurgitant orifice area by PISA measurement. LV, Left ventricle.

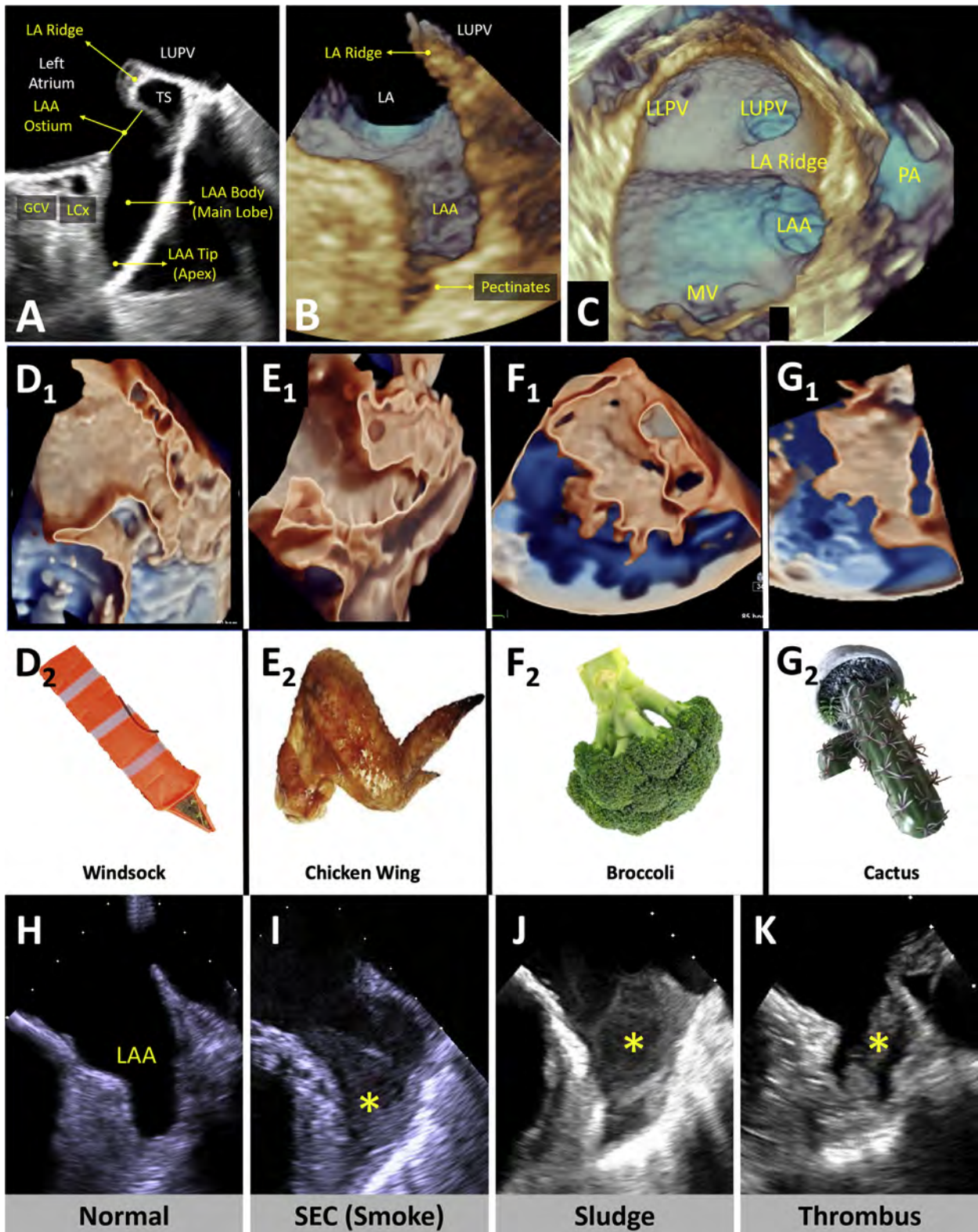


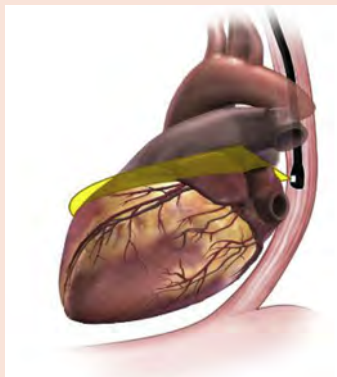
**Figure 26** Left atrial appendage (LAA) anatomy. Two-dimensional TEE imaging at 45° (**A**) demonstrates major anatomic features of a normal LAA. Three-dimensional TEE imaging in a zoom mode (**B**) demonstrates major anatomic features of a normal LAA. Three-dimensional TEE imaging can also be used to image adjacent anatomy (**C**). Advanced three-dimensional rendering tools are useful to characterize the variants of LAA anatomy (**D-G**). In these examples, the 3D-rendered anatomy (subscript 1) and representation of the anatomy (subscript 2) are shown for a “windsock” LAA (**D**<sub>1-2</sub>), “chicken wing” LAA (**E**<sub>1-2</sub>), “broccoli” LAA (**F**<sub>1-2</sub>) and “cactus” LAA (**G**<sub>1-2</sub>). Two-dimensional imaging with long digital captures are used to evaluate flow within the LAA lumen: normal (**H**), spontaneous echocardiographic contrast (SEC; also referred to as “smoke”; **I**), sludge (**yellow asterisk**, **J**), and thrombus (**yellow asterisk**, **K**). GCV, Great cardiac vein; LA, left atrium; LCx, left circumflex coronary artery; LLPV, left lower pulmonary vein; LUPV, left upper pulmonary vein; MV, mitral valve; PA, pulmonary artery; TS, transverse sinus.

**Table 7** LAA imaging protocol

**Imaging Level: Mid-Esophageal 0-135°**

**Acquisition protocol:**

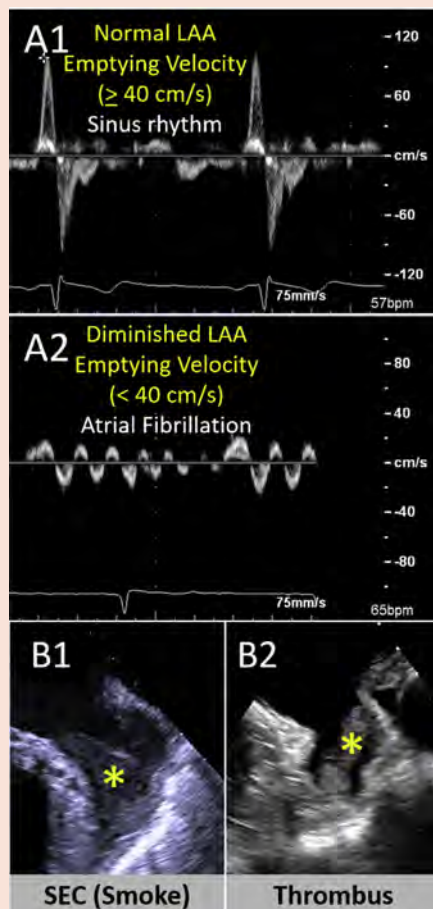
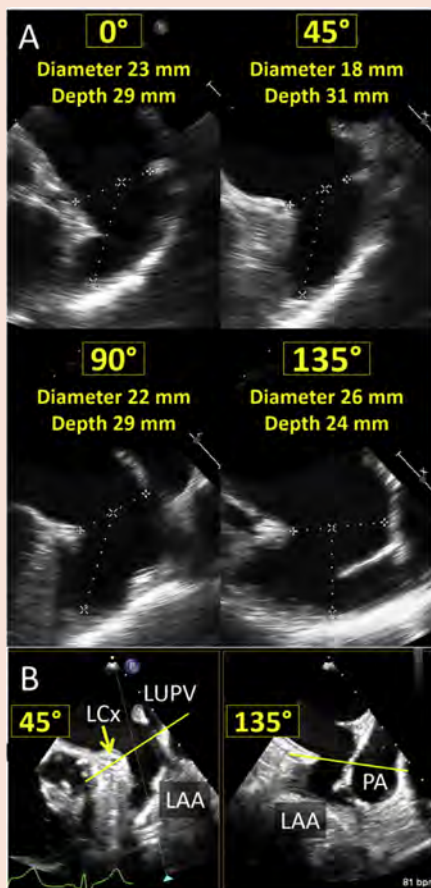
- Maneuver: advance, anteflex with lateral flexion used to optimize imaging.
- Single-plane imaging of the LAA should be performed at ME 0°, 45°, 90°, and 135°.
- Add biplane views as needed.



**Planar images**

**Volumetric imaging**

**Functional imaging**



A. Single-plane imaging of the LAA should be performed at ME 0°, 45°, 90°, and 135°; a slight anteflexion is required to bring the LAA in view. At this view, one must measure the LAA depth and the width of the landing zone.

A. Three-dimensional multiplanar reconstruction allows measurement of at least the maximum and minimum dimensions of the LAA at the intended implantation zone. LAA length can also be measured.

A. Pulsed-wave Doppler of the LAA measures LAA emptying velocity. Higher emptying velocities (toward the LA, above the baseline) in **panel A1** are normal. The lower the emptying velocity (**A2**), the higher the

(Continued)

Table 7 (Continued)

## Imaging Level: Mid-Esophageal 0-135°

B. Biplane imaging can be used from any angle. This is an example of the 45° view in the *left panel* and the 135° view of the LAA in the *right panel*. Note in the 45° view, the proximity of the LUPV and the relationship of the LCx to the LAA. At this view, one also must measure the depth of the LAA and the landing zone diameter.

B. Three-dimensional rendering of the LAA cavity using a transparency imaging mode allows an assessment of the internal structures (B1) as well as overall morphology (B2) in this case, of a “chicken wing” LAA.

chance for stasis and thrombus formation in LAA.  
B. Dense SEC (B1) or thrombus (B2) should be described.

LAA, Left atrial appendage; LCx, left circumflex coronary artery; LUPV, left upper pulmonary vein; SEC, spontaneous echocardiographic contrast.

devices for PFO with right-to-left shunting in the setting of cryptogenic stroke.<sup>128-131</sup>

**2. General Imaging Protocol for the IAS (Tables 8 and 9).** Guidelines for performing comprehensive TEE imaging to delineate the anatomic structure of the right atrium<sup>1</sup> and for the echocardiographic assessment of ASD and PFO have been previously published,<sup>127</sup> and a summary of the essential components of a comprehensive interatrial septal examination listed in Table 8. Preprocedural TTE is adequate in most pediatric patients and some adults, but TEE imaging may better characterize atrial septal anatomy in anticipation of device closure or transseptal puncture (Table 9). This is especially important because intracar-

diac echocardiography currently is increasingly adopted as the modality of choice to guide percutaneous closure of ASDs.<sup>132</sup> Biplane imaging is useful, but with larger defects the image sector may be inadequate. As secundum ASDs may be located anywhere within the septum primum, it is recommended to start imaging at 0°, then increase in 15° increments until fully rotated to 120° for complete evaluation of the septum.<sup>127</sup> The rims of IAS surrounding secundum ASDs should be measured as in Figure 31. Deficiency (<5 mm) of specific rims may preclude closure.<sup>127</sup> Defects larger than available device sizes and anomalous connections of any of the pulmonary veins are additional conditions that may necessitate surgical intervention. IVC interruption is a congenital anomaly in which the IVC terminates below the

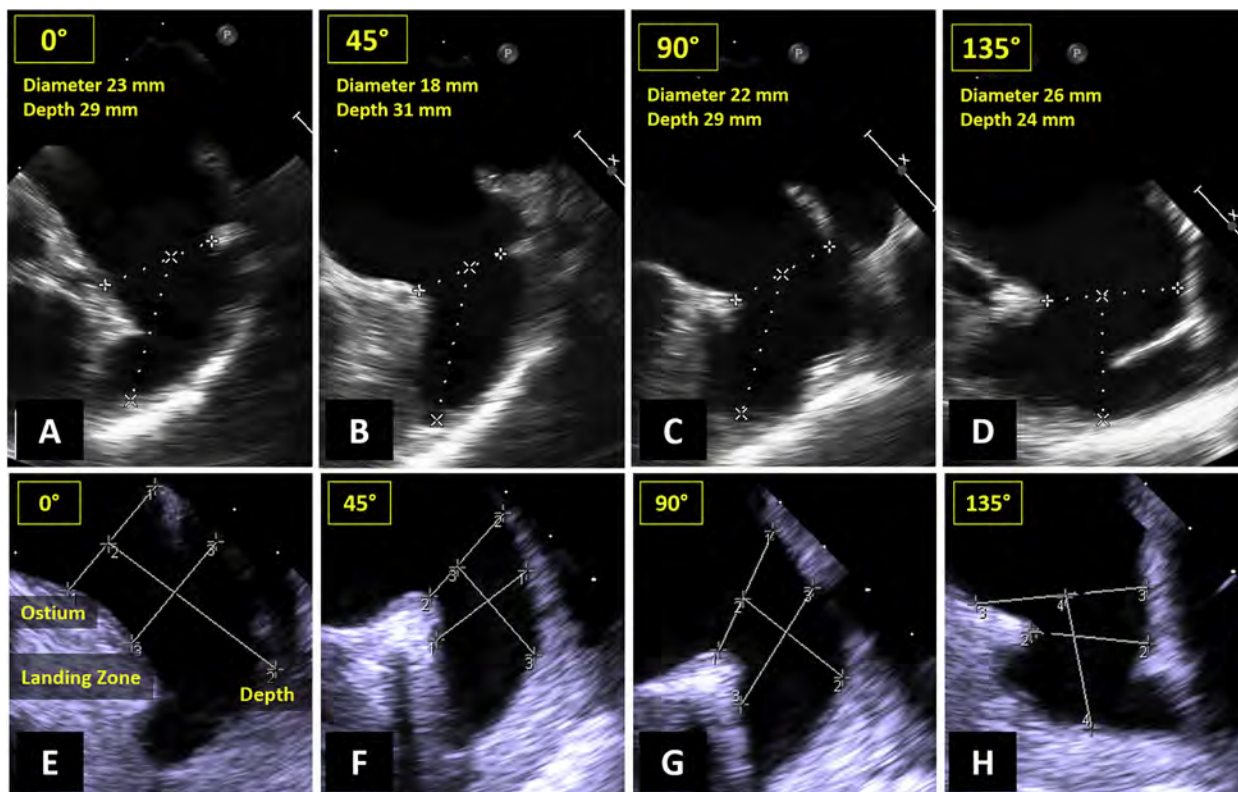


**Figure 27** Two-dimensional imaging of the LAA. The LAA should be visualized at 0°, 45°, 90°, and 135° with both diameter and depth of the LAA measured. For nondisc lobe occluder devices, the ostium is measured from the circumflex artery to a point 2 mm below the tip of the left upper pulmonary vein limbus (A–D). For disc lobe occluders, the ostium is measured from the top of the MV annulus to a point 2 mm from the tip of the pulmonary vein limbus (E–H).

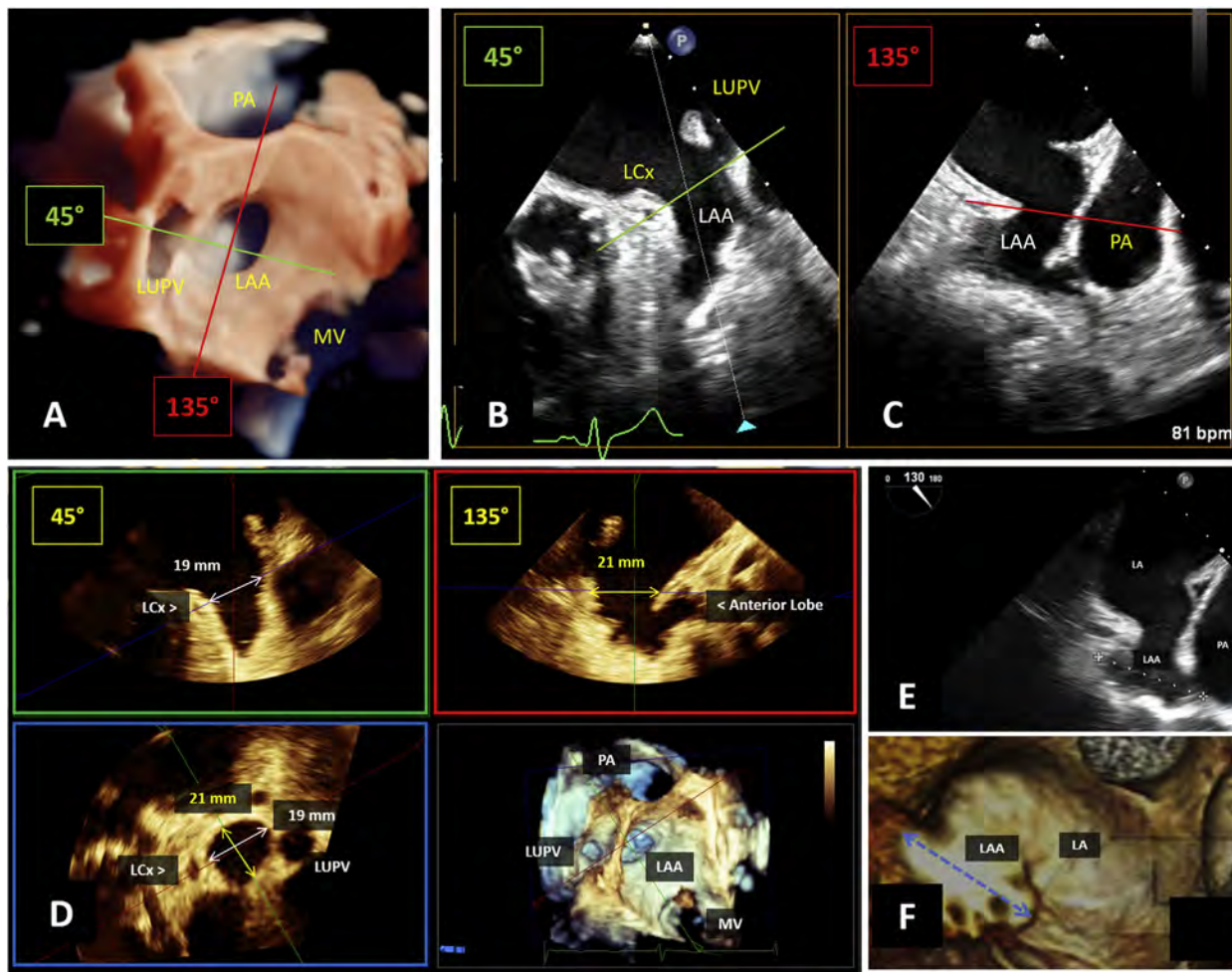


**Figure 28** Three-dimensional imaging of the LAA. Three-dimensional imaging en face zoom view of the LAA (**A**) with corresponding 2D TEE biplane imaging with corresponding axis planes of 45° (**B**) and 135° (**C**). Multiplanar reconstruction of the LAA (**D**) can be used to perform the measurements of the LAA ostium from any 2D orientation with the added benefit of identifying the largest dimension of the LAA, which may fall between the standard 2D imaging angles. Measurement of the largest dimension of the body of the LAA (**E**, **F**) is required for epicardial LAA exclusion devices. *LA*, Left atrium; *LCx*, left circumflex coronary artery; *LUPV*, left upper pulmonary vein.

hepatic vein, and hemiazygous or azygous continuation permits venous drainage into the SVC. Preferably diagnosed by TTE rather than TEE imaging, this condition necessitates either a transjugular<sup>133</sup> or transhepatic approach, which increases the complexity of ASD device placement.

**UE Views.** At 0° stepwise sweeping in 15° increments to 45° demonstrates the superior aspect of the septum. Superiorly located secundum defects or sinus venosus defects (**Figure 30C**) will be seen, as well as the roof of the left atrium and right atrium.

**ME Views.** From the ME four-chamber view at 0°, a stepwise increase of 15° in mechanical rotation to at least 90° to 110° with gentle retroflexion will allow visualization of the entirety of the atrial septum, including for ASD, PFO, and transseptal puncture evaluation. The ME four-chamber view at 0° to 30° images the posterior and atrioventricular valve rims; ostium primum and coronary sinus septal defects, as well as the right pulmonary veins, can be assessed. The ME inflow-outflow view at 45° to 60°

(with aorta in view) images the anterior/superior aortic rim. The ME bicaval view at 90° to 120° images the superior and inferior rims (**Figures 32A** and **32B**); this can be acquired as a single-plane image or as a biplane image from the ME inflow-outflow view at 45° to 60°. Biplane imaging or 3D volumes are useful to characterize elliptical defects. Clockwise rotation of the probe from this view allows imaging of the right pulmonary veins. Counterclockwise rotation (past the LAA) allows imaging of the left pulmonary veins. Our recommendation is to make maximal diameter measurements in the imaging plane, at a point during the cardiac cycle (end-systole vs end-diastole) that yields the largest diameter. Multiple defects may be present in the fossa ovalis, accounting for 4.5% of cases,<sup>134</sup> and are best seen from ME views with color Doppler (**Figure 32C**). The multifenestrated interatrial defect is present in 2.7%<sup>134</sup> of ASDs and is commonly associated with aneurysm of the atrial septum (**Figure 32D**). Delineation of the sizes and locations of multifenestrated defects informs device selection and anticipation of the complexity of transcatheter closure.<sup>135</sup>

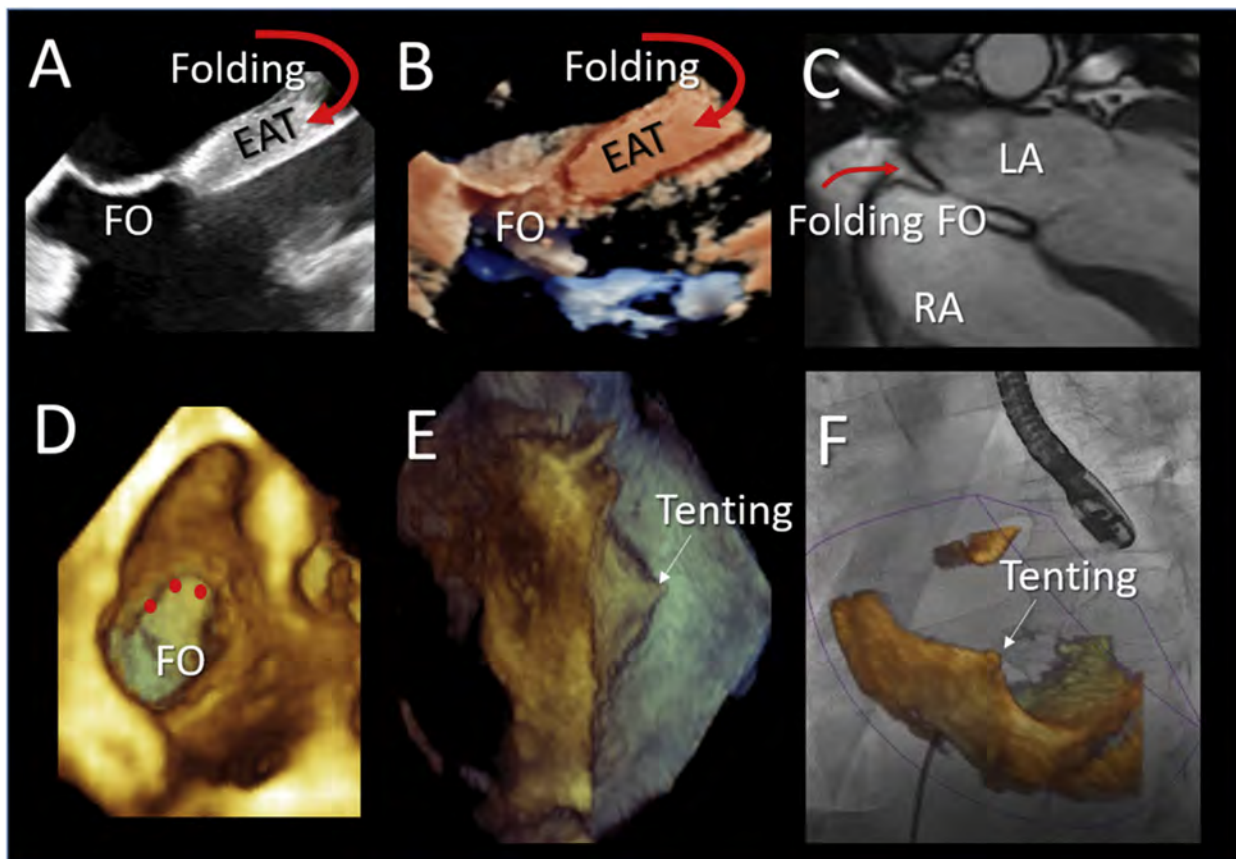


**Figure 29** IAS anatomy. TEE images in **panels A** (2D) and **B** (3D) show the IAS from a bicaval view. The superior portion of the septum secundum, which is often thought of as lipomatous hypertrophy, is not a single wall between the atria but rather infoldings (*curved arrow*) of the left and right atrial walls with epicardial adipose tissue (EAT) in between. The only true IAS is the fossa ovalis (FO). This infolding filled with adipose tissue is also seen on cardiac magnetic resonance imaging (*curved arrow*, **C**). Three-dimensional TEE image showing the FO in en face view (**D**) with the superior rim of the FO marked by *red circles*. Three-dimensional imaging without (**E**) or with (**F**) fusion imaging can be useful to help identify the site of transseptal puncture. LA, Left atrium; RA, right atrium.

Comprehensive PFO assessment, including maximal size at its right and left atrial ends, as well as tunnel length and evaluation for any additional defects, is best performed from the ME inflow-outflow view at 45° to 60° (**Figure 32B**). Color Doppler with a low Nyquist limit (<40 cm/sec) will demonstrate left-to-right interatrial shunting for the secundum ASD and right-to-left or bidirectional shunting for PFO. If color shunting is not apparent with PFO, an agitated saline contrast study (typically without and with physiologic maneuvers) can be performed.<sup>1,127</sup> Saline contrast is less frequently required to diagnose an ASD given advances in echocardiographic imaging capabilities.<sup>127</sup>

**UE View.** Retraction of the probe to the UE position will show the SVC-related septum secundum for measurement of the superior rim length for ASD closure, and length of a PFO tunnel. At 120°, a suspected coronary sinus septal defect may be seen en face behind the posterior wall of the left atrium.<sup>126</sup> The appearance of the SVC “straddling” the IAS (**Figures 30C** and **30D**) is

the classic manifestation of a superior sinus venous septal defect, and with clockwise rotation of the probe from this view, anomalous drainage of the right upper and middle pulmonary veins can be demonstrated to differentiate from a superiorly located secundum ASD.

**DE View.** Advancement of the probe to a lower esophageal position with gentle flexion should outline the inferior rim. This is the most difficult rim to delineate by TEE imaging<sup>136</sup> yet the most important, as deficiency of the inferior rim, found in 3.3% of secundum ASDs,<sup>134</sup> is associated with important device failure.<sup>134,136,137</sup> Suspicion of inferior rim deficiency may need additional confirmation by TTE in patients with good echocardiographic windows or intracardiac echocardiography at the time of percutaneous intervention, as with adjusted deployment, selective cases can be percutaneously closed.<sup>138</sup> This same probe position is ideal to identify a Chiari network (**Figure 32D**), a filamentous structure formed by incomplete resorption of the right valve of the sinus venosus, found in 2% to 3%

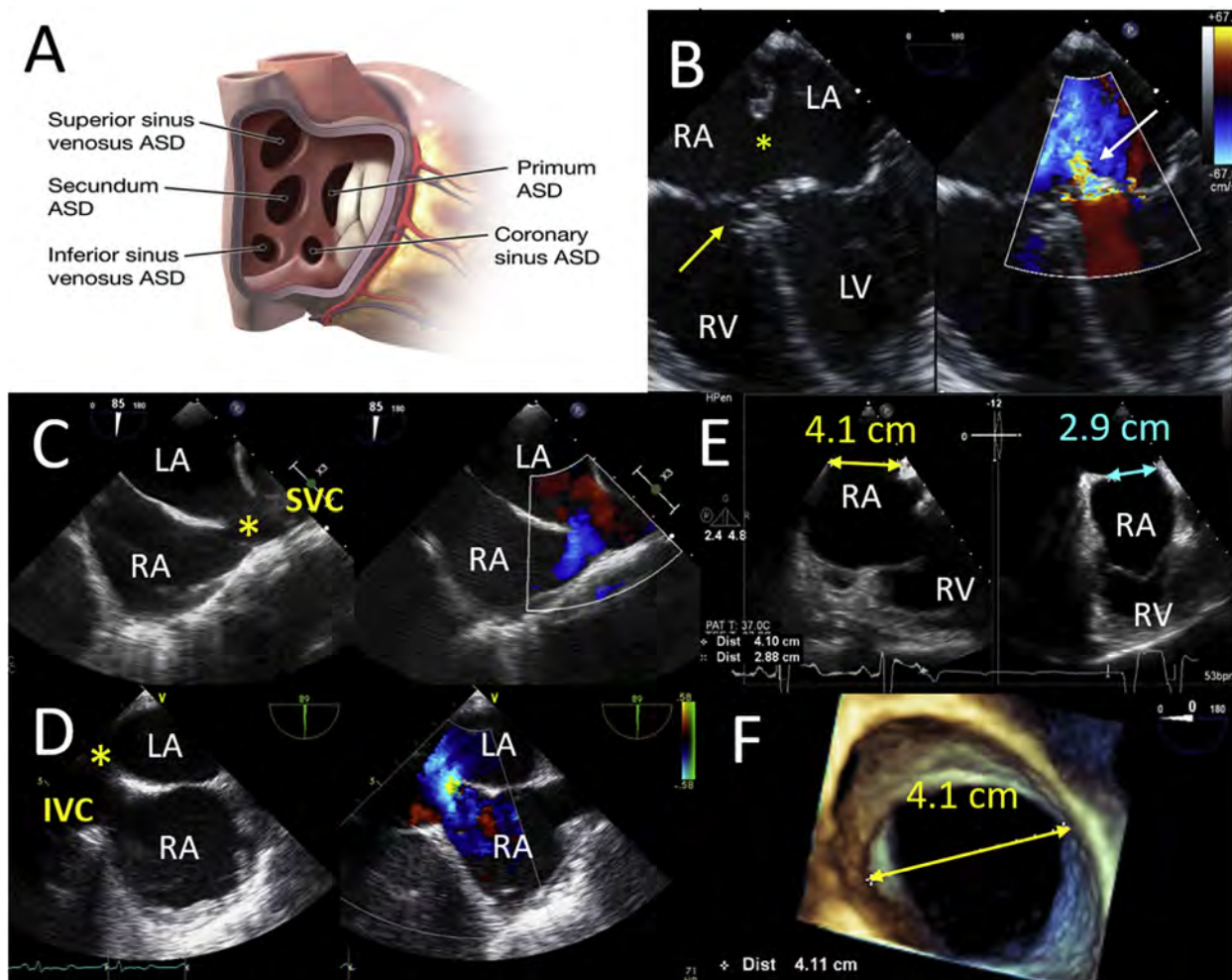


**Figure 30** ASD types and examples nonamenable to transcatheter closure: ASD type, size, and location predict candidacy for transcatheter closure. Secundum ASD may be located in the middle of the IAS, whereas nonsecundum ASD are defined by typical location (**A**). Primum ASD (**B**) is characterized by defect of the endocardial cushions (*left-hand panel, yellow asterisk*) with insertion of the left and right atrioventricular valves at the same level (*yellow arrow*) and a cleft MV frequently associated with regurgitation (*right-hand panel, white arrow*). The superior sinus venosus defect (**C, yellow asterisk**) has no superior rim and abuts the SVC. The inferior sinus venosus defect (**D, yellow asterisk**) has no inferior rim and opposes the IVC. Both these defects are not amenable to transcatheter closure. Although secundum ASDs are typically approachable by transcatheter techniques, a large defect (biplane image in **panel E** and 3D image in **panel F**) lacking the inferior rim or more than two other rims may also require surgical closure. LA, Left atrium; LV, left ventricle; RA, right atrium; RV, right ventricle.

of the population.<sup>139</sup> Catheter entrapment,<sup>140</sup> paradoxical right-to-left atrial embolus,<sup>139</sup> and herniation of ASD occluder device<sup>141</sup> have been described with Chiari networks, though fortunately complications appear to be rare.

This is also the optimal view to image the roof of the coronary sinus independently from the left atrium. Presence of a dilated coronary sinus ostium and a visualized defect with 2D imaging and color Doppler confirms the presence of a coronary sinus septal defect. An isolated persistent left SVC will generate a comparable image without an identifiable defect or right heart dilatation.

**TG View.** From the TG LV SAX view at 0° to 20°, further anteflexion will result in a SAX image of the MV. From this imaging plane, an anterior leaflet cleft, associated with ostium primum ASD, can be visualized if present.

**Three-Dimensional Imaging.** A comprehensive description of 3D image acquisition for PFO and ASD is published in the 2015 ASE guideline.<sup>127</sup> Real-time or narrow-angle initial acquisitions are followed by electrocardiographically gated, wide-angle, higher temporal and spatial resolution acquisitions from several key views:

**Table 8** Essential components of atrial septal evaluation

ASD	PFO	Site of transeptal puncture
ASD type	PFO tunnel length	Secundum septal thickness
ASD size (maximal and minimal diameters) during end-systole and end-diastole	Maximal size at right atrial end	Presence of PFO or ASD
ASD location within the septum	Maximal size at left atrial end	Three-dimensional en face view of MV to identify commissural line and medial commissure
Measurement of all rims	Total length of atrial septum	
ASD shape	Distance from PFO to venae cavae	
Exclude pulmonary arterial hypertension	Right-to-left shunting by color Doppler or agitated saline contrast injection	
Exclude anomalous pulmonary venous connections	Exclude anomalous pulmonary venous connections	
Presence of multiple fenestrations or additional ASDs	Presence of additional ASDs	

For all three categories (ASD, PFO, and transeptal puncture), the following should also be evaluated: presence or absence of atrial septal aneurysm and associated findings (Eustachian valve or Chiari network).

ME SAX starting at 0°, basal SAX 30° to 60°, bicaval 90° to 120°, deep TG bicaval 100° to 120°, and four-chamber 0° to 20° views. Anatomy of the intact septum, ASD, and rims is demonstrated with en face 3D acquisitions of the septum from right and left atrial aspects (Figure 31). Real-time en face imaging characterizes the shape and size of the defect(s) throughout the cardiac cycle.

### G. Assessment of the Interventricular Septum (Table 10)

VSDs occur in two to 10 per 1,000 live births.<sup>142-144</sup> Of the five congenital variants of VSD (Figure 33A), perimembranous and muscular are the two that can undergo percutaneous closure. Outlet (also known as supracristal or subarterial), malaligned, and atrioventricular canal type VSDs cannot undergo device closure, because of absence of circumferential rims.

**1. Anatomy of the Interventricular Septum.** The interventricular septum separates the left and right ventricles and has a complex shape and structure. Its radius of curvature is the same as that of the LV free wall and comprises about one third of the total LV mass.<sup>145</sup> When viewed from the left ventricle, it consists of posterior, anterior, and upper membranous portions. When viewed from the right ventricle, the membranous portion is divided into an interventricular region and an atrioventricular aspect, which is above the TV and forms a part of the floor of the right atrium.<sup>146</sup> The anterior septum is divided into two parts, one lying inferior and posterior to the crista supraventricularis and extending between it and the tricuspid ring and the other lying superior and anterior to the crista supraventricularis and extending from it to the annulus fibrosus of the PV. A VSD can occur anywhere in the septum. The criteria for closure of congenital or acquired VSD in adulthood may include history of endocarditis and/or ratio of pulmonary flow to systemic flow > 1.5, which may

manifest as persistent or increasing left heart dilatation, and only in the absence of significant pulmonary arterial hypertension.<sup>72</sup>

Congenital VSDs are shown in Figure 34.<sup>147</sup> Outlet VSDs, also referred to as supracristal or subarterial, are defects located in the infundibular/outlet septum and immediately below the PV with no anterior or superior rim of conal septum. Because of the proximity of the defect to the PV with absence of conal septum, this VSD is usually closed surgically, though periventricular hybrid device placement is possible.<sup>148-150</sup> Malaligned defects, within the conoventricular or conal septum, occur in patients with tetralogy of Fallot, double-outlet right ventricle, and interrupted aortic arch. These invariably require surgical closure at the time of repair for the associated lesion(s). Inlet VSD (VSD of the atrioventricular canal type) is characterized by its location posterior and inferior to the septal leaflet of the TV. The proximity of both atrioventricular valves and association with straddling chordal and papillary muscle attachments<sup>151</sup> across the VSD preclude device closure. Muscular VSDs can be located anywhere within the trabecular septum and may be single or multiple. They are circumferentially surrounded by muscular tissue and rarely adjacent to important structures. Defects that lie entirely within the membranous septum or extend into the adjacent septum and structures are termed para- or perimembranous and account for 80% of VSDs in surgical and autopsy series.<sup>152,153</sup> The membranous septum lies adjacent to the TV on the right side and the right coronary/non-coronary commissure of the AV on the left side. This portion of the septum is thin and has both an interventricular and an atrioventricular component, accounting for the apical offset of the TV. Conduction tissue courses in the posteroinferior border of the membranous septum.<sup>151</sup> Tethering of the anteroseptal TV leaflet has been implicated in spontaneous closure of these defects, as well as aneurysm of the membranous septum, a common finding with important implications for percutaneous device closure. Finally, perimembranous

**Table 9** IAS imaging protocol**Imaging level: ME 0°–30° and right ventricular inflow-outflow 30°–65°****Acquisition protocol:**

- At 0°–30°, pulmonary veins, ostium primum and coronary sinus septal defects can be visualized.
- At 30°–65°, with AV en face, probe position may require advancement or withdrawal to optimize visualization of a secundum ASD and/or PFO and rims.
- Retroflexion and full sector width may be required for larger defects.

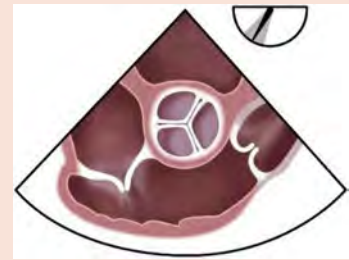
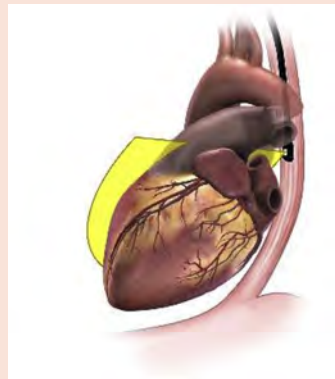
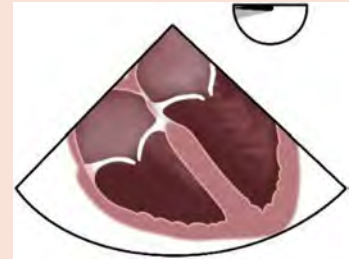
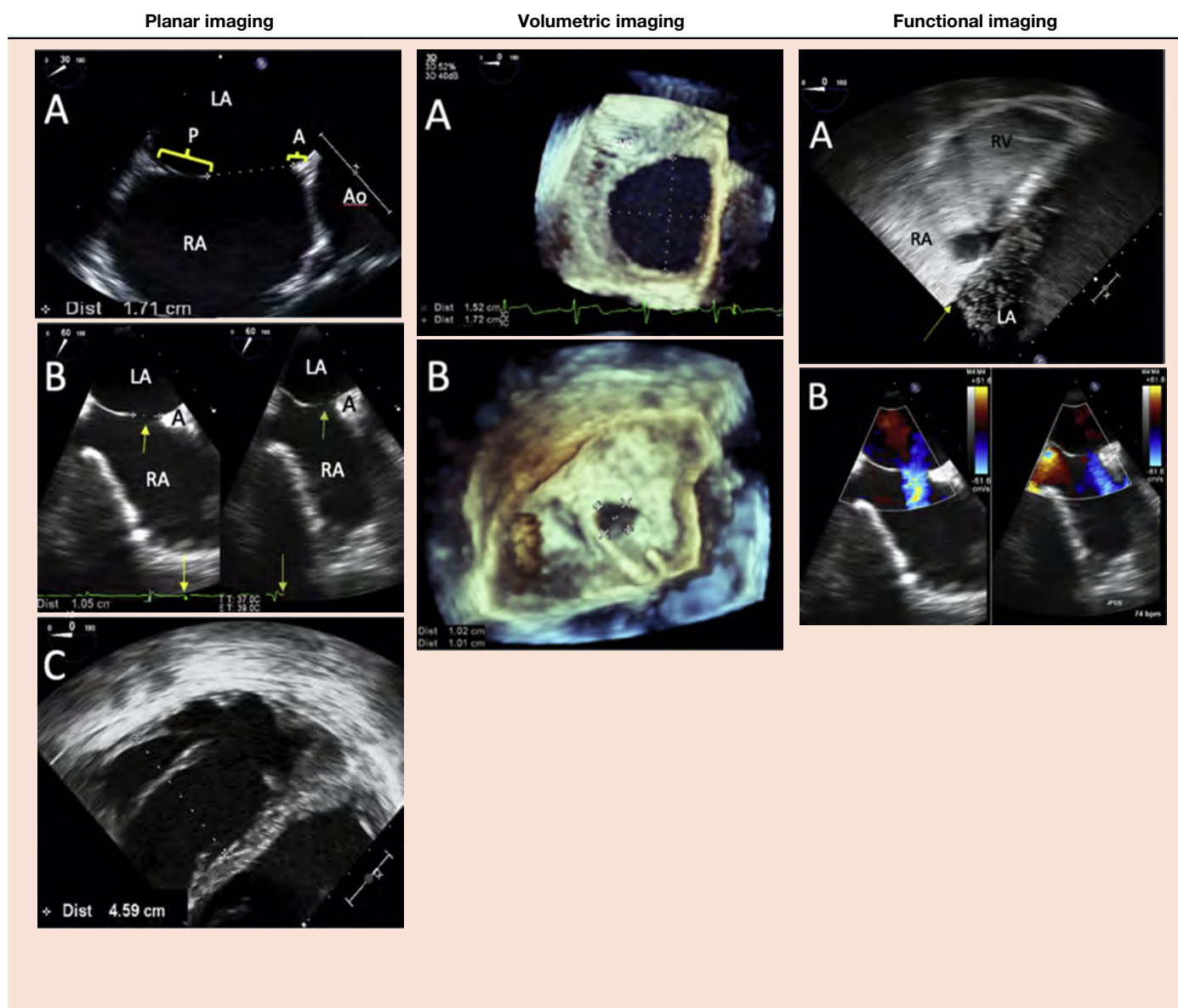
*(Continued)*

Table 9 (Continued)



- A. In SAX the aortic (A) and posterior (P) rims of the defect (*yellow brackets*) are defined, and measurement is made of the secundum ASD. Deficiency (<5 mm diameter) of the aortic rim does not typically preclude device closure.
- B. A small secundum ASD, also seen in SAX, during diastole (*yellow arrow* indicates diastole on ECG) and systole (*green arrow* indicates systole on ECG). Measurements should be made when the defect is largest during the cardiac cycle.
- C. At 0° angulation, right ventricular dilatation is demonstrated.
- D. PFO is best seen at 30°–65°. Here tunnel length (shown), and diameter at the right atrial and left atrial aspects can be measured.

- A. The large secundum ASD defect is mildly elliptical, and measurements are comparable with 2D images shown in both SAX and long-axis (**A**) planar imaging panels.
- B. Three-dimensional imaging of even smaller defects can assist in localizing and measuring the defect. In this case, a centrally located, symmetrically round secundum ASD is demonstrated with measurements corresponding with 2D derived measurements in both ME SAX and long axis (**B**) planar imaging panels.

- A. Positive agitated saline contrast study with dense opacification of RA and RV, and clear early passage of microbubbles to the LA (*arrow*) in a case of PFO.
- B. Color Doppler should demonstrate left-to-right shunting through an ASD at a moderate Nyquist limit. As shown in the adjacent planar images, there can be marked dynamic size variation in diastole (*left panel*) compared with systole (*right panel*).

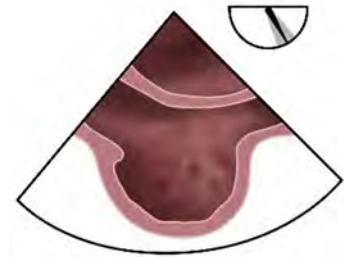
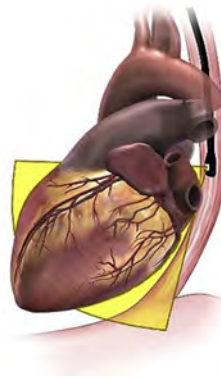
(Continued)

**Table 9** (Continued)

**Imaging level: ME long-axis 70°–110° view**

**Acquisition protocol:**

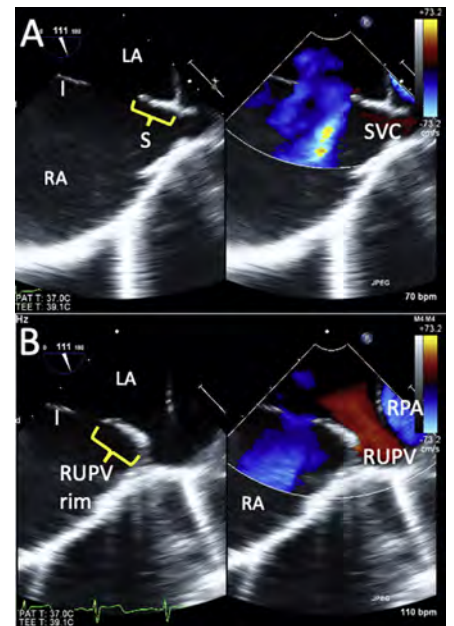
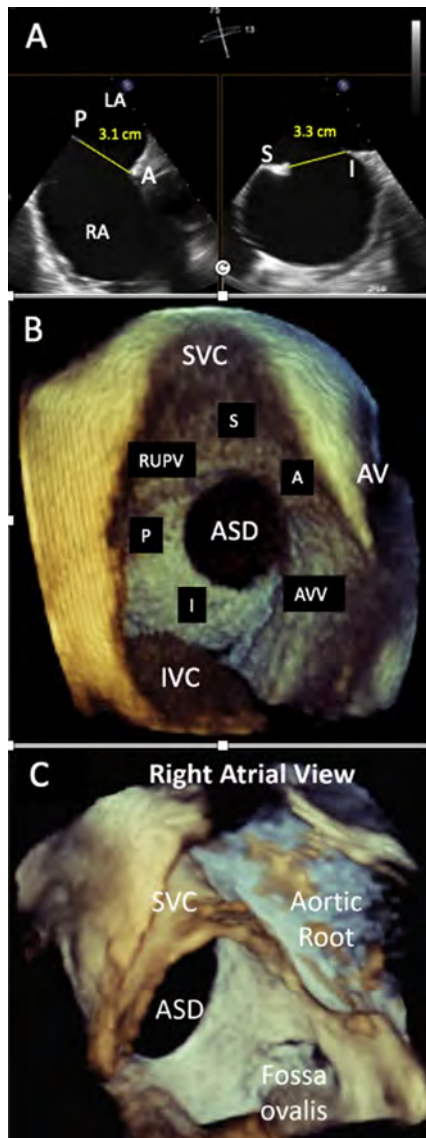
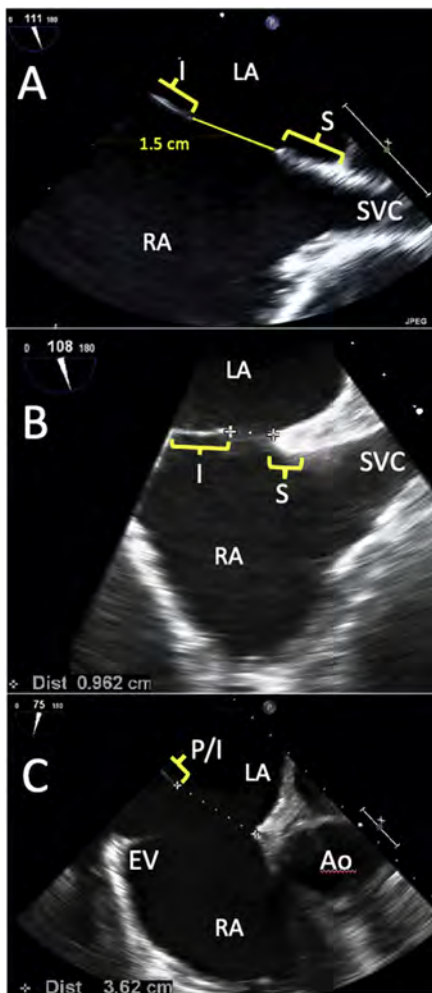
- Maneuver: when the ASD is in view on aortic SAX view, mechanical rotation to this view shows superior and inferior rims.
- Withdraw probe to show superior defects and rim.
- Advancement of the probe and gentle ante-flexion may assist with the most difficult to visualize inferior rim.



**Planar imaging**

**Volumetric imaging**

**Functional imaging**



(Continued)

Table 9 (Continued)

## Imaging level: ME long-axis 70°–110° view

<p>A. Large secundum ASD (as seen in ME 0–30° view, Volumetric imaging, <b>panel A</b>) demonstrating measurement at maximal diameter with superior (S) and inferior (I) rims (<i>yellow brackets</i>) indicated. The inferior rim, best seen in this bicaval view, may be difficult to measure but visualization of &gt;5 mm rim suggests adequate size for device closure.</p> <p>B. Small secundum ASD (as seen in ME 0–30° view, Volumetric imaging, <b>panel B</b>) with adequate superior (S) and inferior (I) rims.</p> <p>C. Another larger secundum ASD measured from the anterosuperior (A) rim to the posterior/inferior (P/I) rim. With severe right ventricular dilatation and levorotation of the heart, as in this example, a 75° angulation demonstrates a view more typical of aortic short axis. Note the prominent Eustachian valve (EV), which can easily be mistaken for the P/I rim. Again, note the poor visualization of the entirety of the inferior rim, but sufficient length is seen to consider device closure.</p>	<p>A. Biplane imaging showing the anterior/posterior and inferior/superior aspects of the large secundum ASD and maximal measurements in both planes.</p> <p>B. Three-dimensional imaging (right atrial perspective) shows the location of the rims of a large secundum ASD: (1) SVC rim, the posterior/superior rim between the ASD and the SVC; (2) aortic rim, the anterior/superior rim between the ASD and atrioventricular annulus and aortic root; (3) atrioventricular valve rim, the anterior/inferior rim between the ASD and the AVVs; (4) IVC rim, the posterior/inferior rim between the ASD and the IVC; (5) posterior rim, the posterior rim toward the pulmonary veins.</p> <p>C. Three-dimensional imaging of a sinus venosus ASD (absence of the sinus venosus IAS) from the right atrial perspective. Note the defect is superior to the fossa ovalis.</p>	<p>A. The superior rim (S; <i>yellow bracket</i>) of the defect is adjacent to the SVC as demonstrated in this color-compare image. Left-to-right shunting through the defect may overestimate sizing, thus 2D images are preferred for diameter. Any right-to-left shunting may be indicative of pulmonary hypertension.</p> <p>B. Clockwise rotation from the SVC view will demonstrate the rim between the ASD to the RUPV (<i>yellow bracket</i>) and normal drainage of the RUPV to the LA. Deficiency of this rim may result in obstruction of RUPV flow after device closure.</p>
--	---	--

A, Anterior; Ao, aorta; AVV, atrioventricular valve; EV, Eustachian valve; I, inferior; IAS, interatrial septum; IVC, inferior vena cava; LA, left atrium; LUPV, left upper pulmonary vein; P, posterior; RA, right atrium; RPA, right PA; RUPV, right upper pulmonary vein; S, superior; SAX, short axis.

VSDs can be associated with the development of hemodynamically important lesions, including AV prolapse,<sup>154</sup> subaortic membrane,<sup>154,155</sup> and double-chambered right ventricle (a condition in which the subpulmonary infundibular os becomes narrowed and stenotic).<sup>156</sup> The identification of any of these associated lesions usually prompts surgical repair. In the absence of contraindications, transcatheter device closure is a feasible option in expert hands, with multiple meta-analyses describing comparable transcatheter and surgical outcomes for closure success, incidence of complete heart block, and valvular regurgitation in both children and adults.<sup>157-159</sup>

Acquired VSDs fall into two main categories: ventricular septal rupture in the setting of septal infarction and traumatic disruption, typically in the setting of a penetrating injury. Ventricular septal rupture as a mechanical complication of acute myocardial infarction has a bimodal occurrence, with peak frequencies in the first 24 hours and at day 3 to 5 after acute myocardial infarction.<sup>160</sup> Transcatheter device closure of a VSD caused by ventricular septal rupture is an attractive alternative to surgical closure, with almost 50% reduction in the 30-day mortality rate, especially for late intervention (>2 weeks after acute myocardial infarction), in contrast to conservative therapy, which carries a 92% 30-day mortality rate.<sup>161</sup> However, despite high technical success and relatively low procedural complication rates, there remains very high in-hospital mortality.<sup>160</sup>

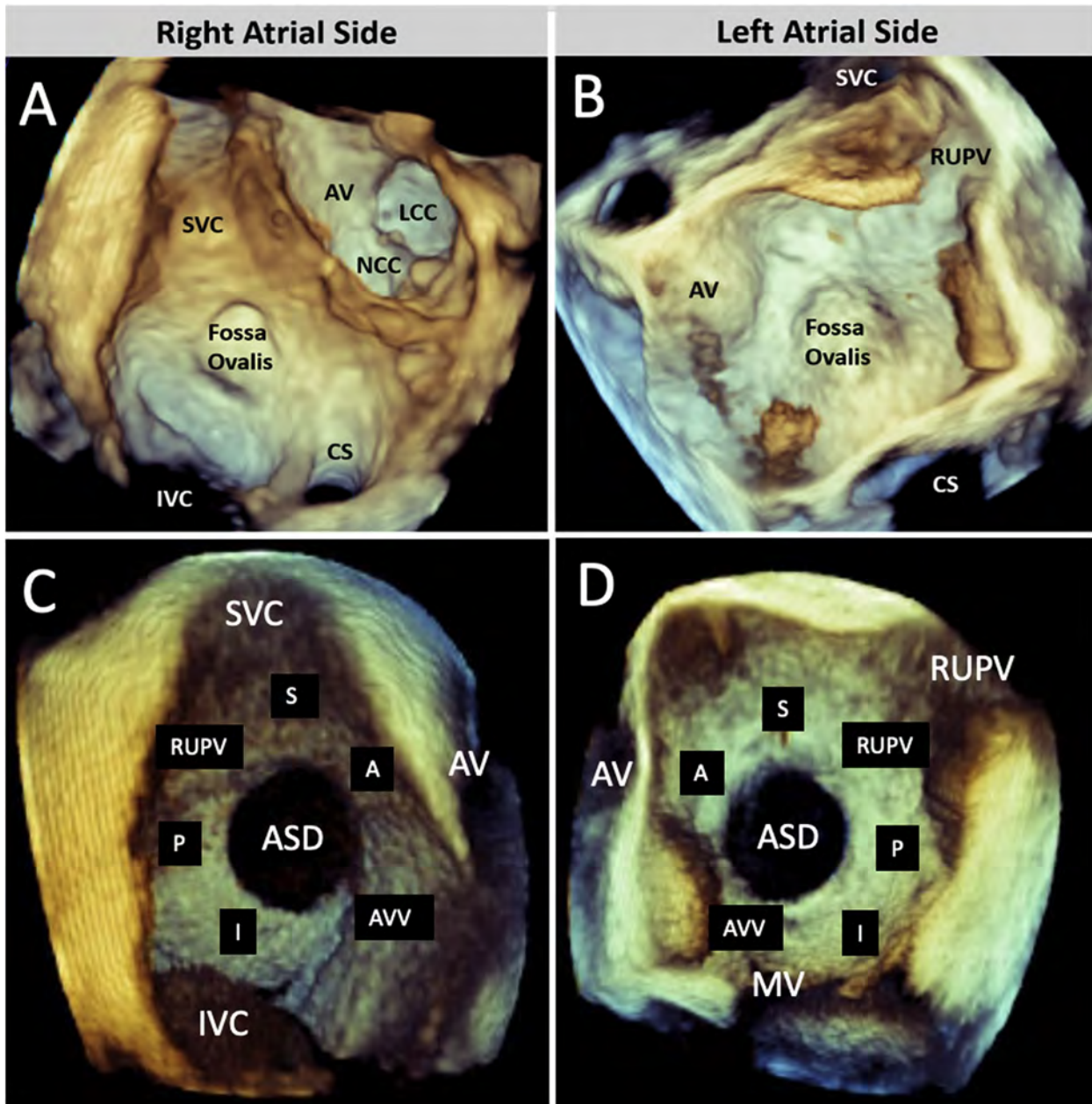
Traumatic VSD is a relatively rare but important complication of penetrating cardiac trauma, blunt chest trauma, and cardiac surgery.<sup>162</sup> Transcatheter closure of traumatic VSDs has been described in patients who are poor candidates for open surgical repair.<sup>162</sup>

## 2. General Imaging Protocol for the Interventricular Septum

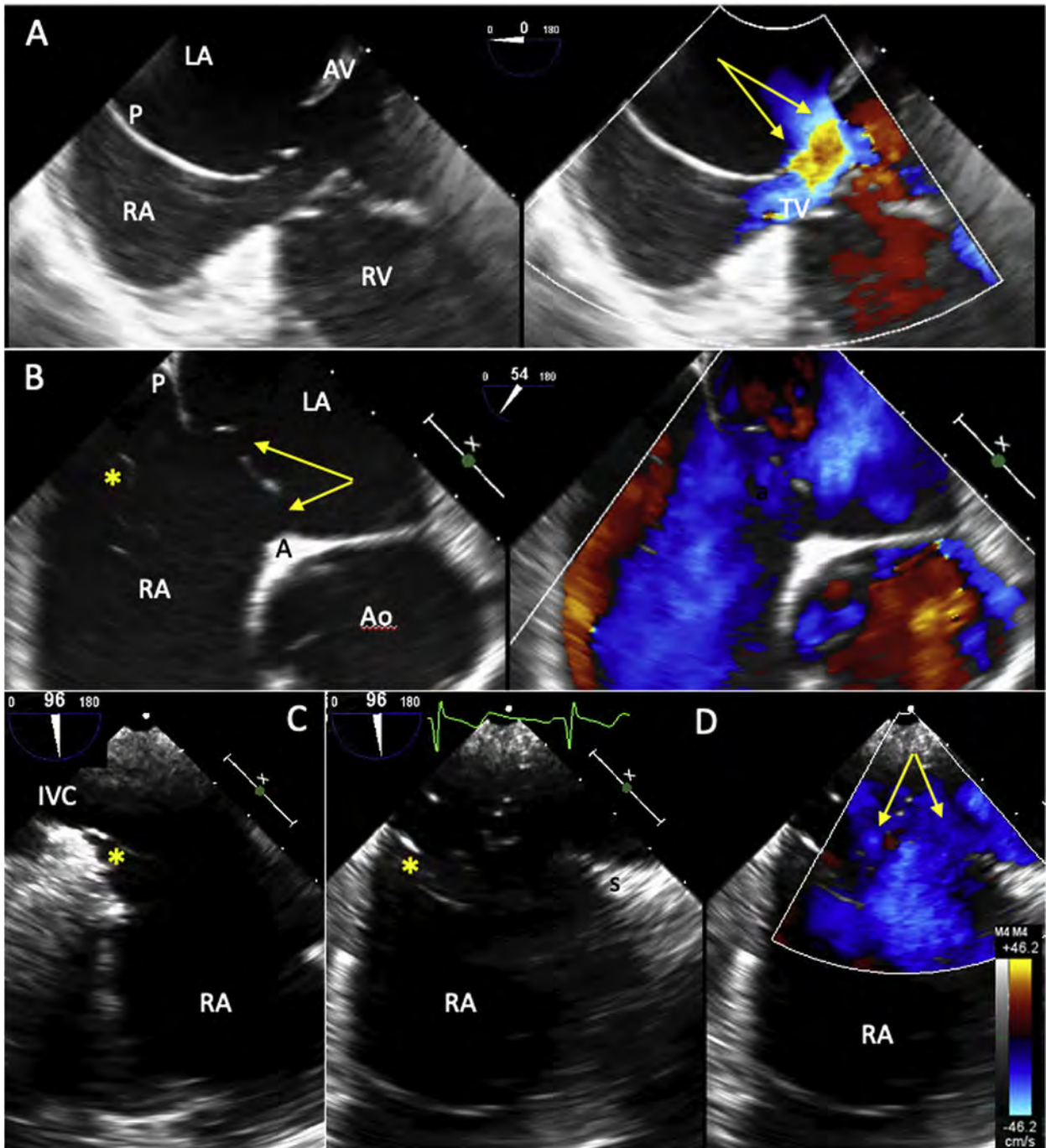
(Table 10). As congenital and acquired muscular VSDs may be located anywhere within the muscular septum, and may be multiple, it is recommended that all TEE positions that image the interventricular septum be acquired with 2D and color Doppler echocardiography. Once a VSD is identified, an orthogonal image should also be obtained in 2D single- or biplane imaging to fully characterize the defect. The peak velocities of TR and flow through the VSD should be sampled using CW Doppler in the view that provides the most in-line angle of interrogation to estimate PA pressure. If either of these measures suggests pulmonary arterial hypertension, further imaging should confirm absence of RVOT obstruction (Figures 33A and 33B) that may contribute to abnormal Doppler velocities. If there remains any suspicion for pulmonary hypertension in patients with congenital VSD, we recommend referral to an adult congenital heart disease center of excellence,<sup>72</sup> as the patient may have Eisenmenger syndrome with irreversible pulmonary arterial hypertension and therefore not be a candidate for VSD closure.

**ME Views.** The ME four-chamber view at 0°, sweeping anterior to posterior in the septum with gentle flexion and anteflexion, may demonstrate an apical, mid, or basilar muscular congenital or acquired VSD but is not ideal for anterior muscular defects. The poor Doppler angle of interrogation from this view will rarely estimate PA pressure reliably; however, a sample of the TR jet may be possible.

The ME AV SAX view at 45° to 60° will display a perimembranous VSD in the 7 to 8 o'clock position immediately adjacent to the septal leaflet of the TV (Figure 33B). These defects



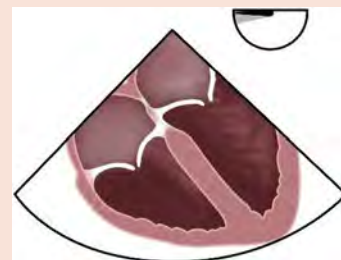
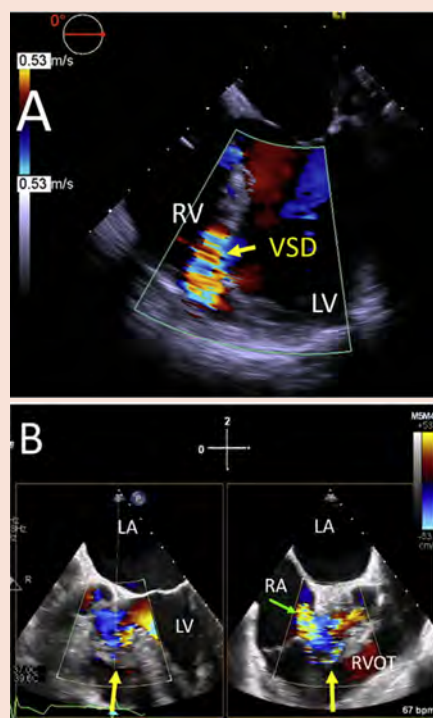
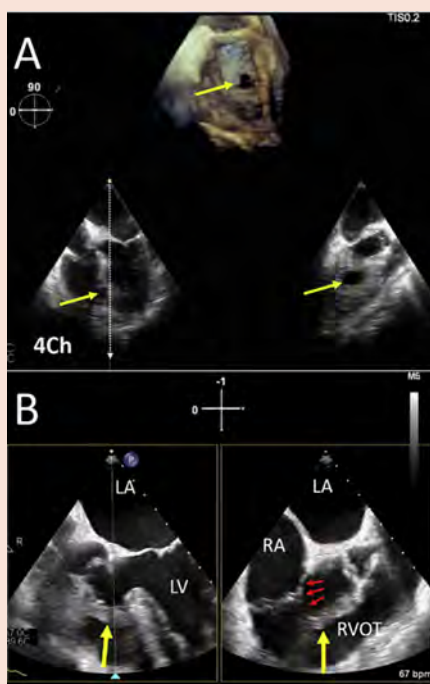
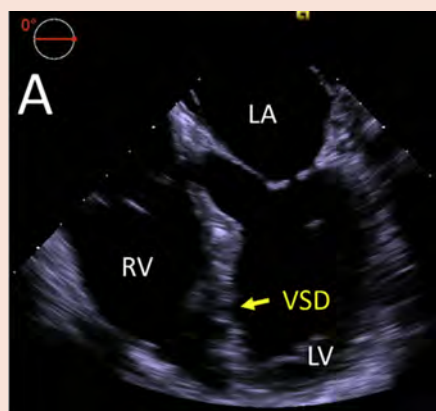
**Figure 31** ASD rims: these 3D volumes show the intact IAS (**A**, from the right atrial view; **B**, from the left atrial view) and a large secundum ASD (**C**, from the right atrial view; **D**, from the left atrial view). The rims are identified by their anatomic location and measured from the ASD to the adjacent structure(s): superior rim (S), bordered by the SVC; aortic rim (A), the anterior/superior rim adjacent to the aortic root; atrioventricular valve rim (AVV), the anterior/inferior rim adjacent to the atrioventricular valves; inferior rim (I), the posterior/inferior rim adjacent to the IVC and most difficult to visualize by TEE imaging; and posterior rim (P), measured to the posterior atrial wall, often adjacent to the pulmonary veins. CS, Coronary sinus; IAS, interatrial septum; LCC, left coronary cusp; NCC, noncoronary cusp; RUPV, right upper pulmonary vein.



**Figure 32** Complex secundum ASDs. Moderate-sized secundum ASD (**A**) with aneurysmal septum primum and fenestrations (*yellow arrows*). The aneurysm is seen extending almost to the TV. Another multiply fenestrated and aneurysmal septum primum (**B–D**), which is separate from an adjacent Chiari network (*asterisk*). In low esophageal long-axis position (**C**), the Chiari network insertion (*asterisk*) is seen anterior to the IVC, separate from the inferior rim of the ASD. Color-compare imaging (**D**) shows left-to-right shunting through multiple fenestrations (*yellow arrows*) in the septum primum, which may be difficult to differentiate from the filamentous Chiari network. Both cases were amenable to transcatheter device closure. ASD rims are indicated where visible: A, Aortic; AV, atrioventricular; P, posterior; S, superior from the various mid- and low-esophageal views.

**Table 10** Interventricular septum imaging protocol**Imaging level: ME 0°–30°****Acquisition Protocol:**

- ME 0°–30° position with probe advancement, retraction, and anterior-to-posterior sweep for muscular septum/VSDs.
- AVC defects seen at the level of the atrioventricular valves.

**Planar imaging****Volumetric imaging****Functional imaging**

A. A muscular VSD can be imaged from the ME views of the interventricular septum.

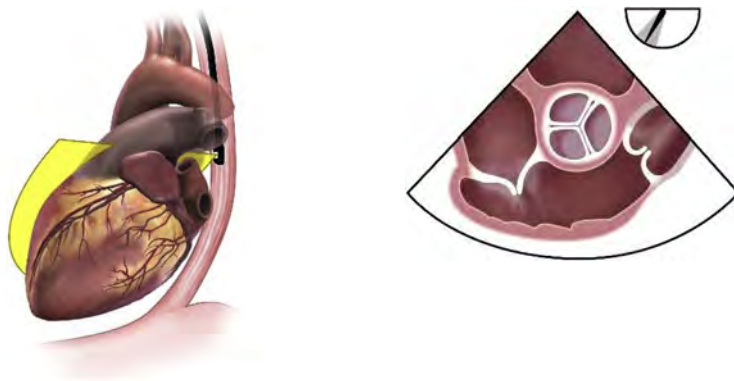
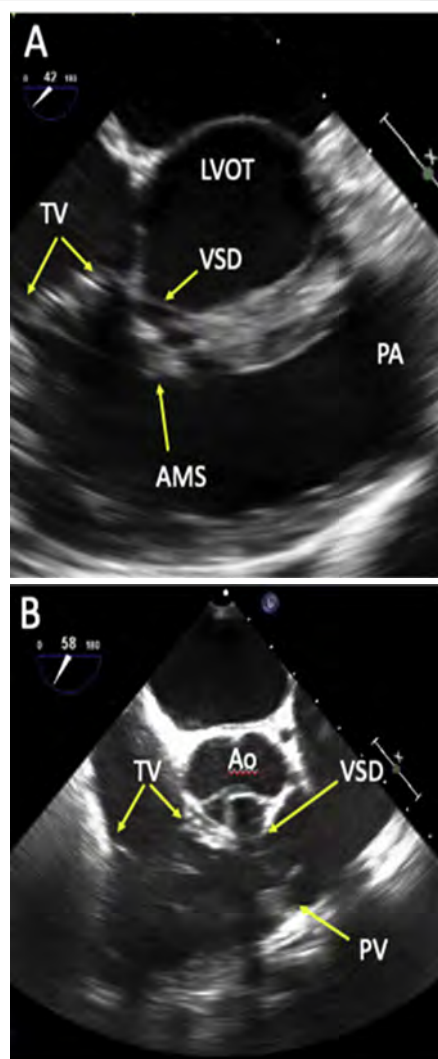
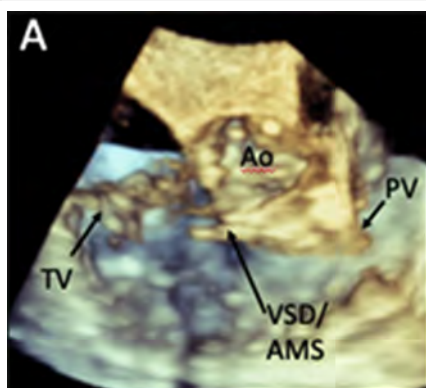
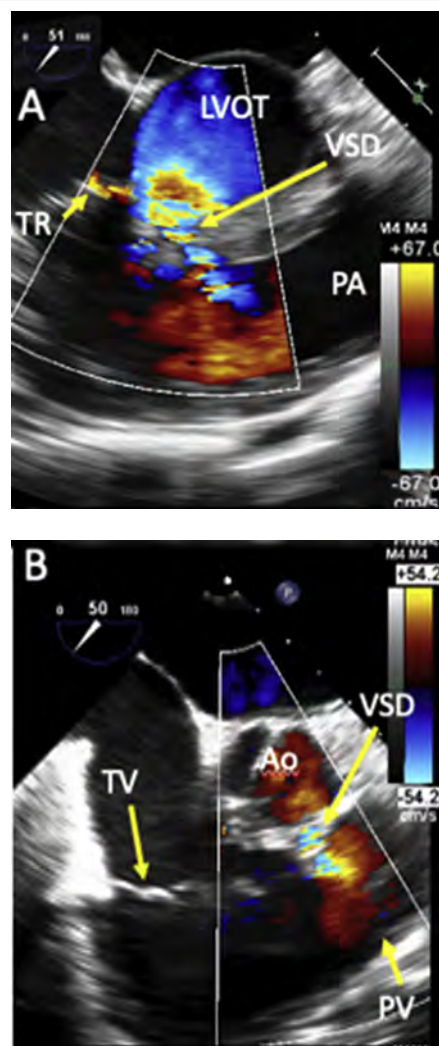
A. Triplane imaging shows the en face 3D VSD (yellow arrow) on the top image, with 2D biplane imaging of the defect from the apical 4Ch view and orthogonal image of the interventricular septum.  
B. Biplane imaging of a membranous VSD (yellow arrow) and an associated AMS (red arrows) formed by the septal TV leaflet.

A. Color Doppler imaging of the muscular VSD confirms the direction of the turbulent flow, but CW Doppler may not be optimally aligned to assess peak velocities and gradients.  
B. Biplane imaging with color Doppler of the same membranous VSD as in volumetric imaging panel B with turbulent flow across the VSD (yellow arrow) as well as TR (green arrow).

(Continued)

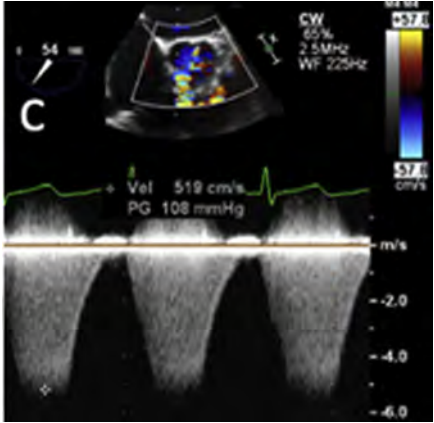
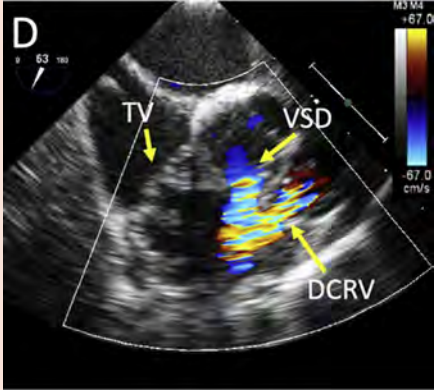
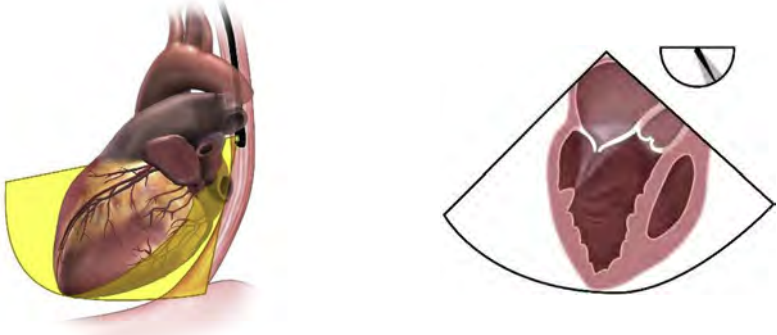
**Table 10** (Continued)**Imaging level: ME SAX 40°–65°****Acquisition Protocol:**

- From ME 40°–65° view, with anteflexion and probe rotation clock- or counterclockwise, one can achieve better alignment for visualization and comprehensive Doppler assessment of the VSD jet and/or TR jet.
- Advancing the probe (thus positioning the RVOT perpendicular to the ultrasound beam) may allow visualization and Doppler assessment of a subpulmonic VSD.

**Planar imaging****Volumetric imaging****Functional imaging**

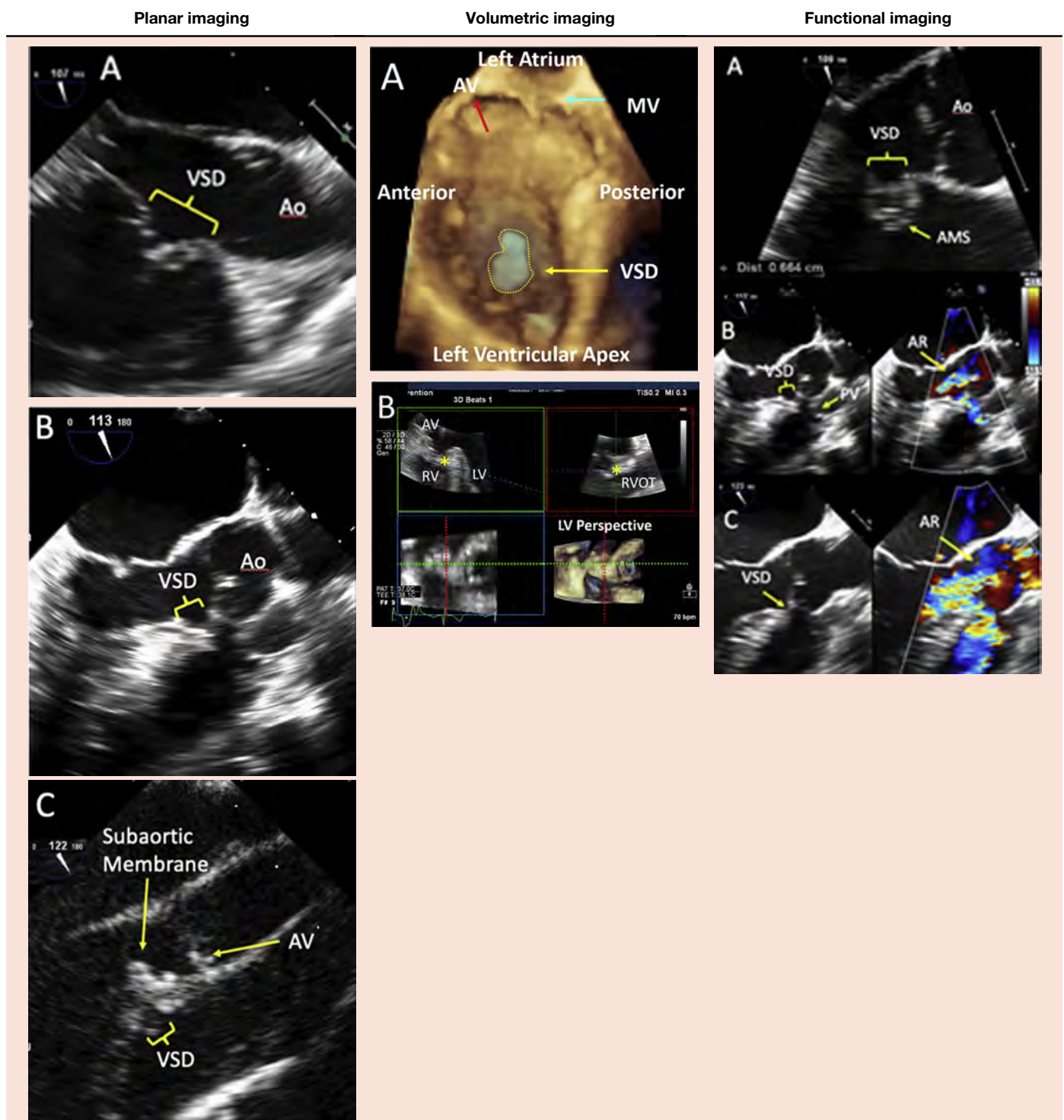
(Continued)

Table 10 (Continued)

Planar imaging	Volumetric imaging	Functional imaging
		
<p>A. A membranous VSD will be visualized behind the septal leaflet of the TV, including AMS, if present, which frequently involves TV tissue.</p> <p>B. Subpulmonic VSD, in contrast, is positioned immediately below the PV, remote from the TV.</p>	<p>A. Three-dimensional imaging is best achieved from the ME position. Image quality may be compromised by thin, hypermobile AMS commonly seen with membranous VSD.</p>	 <p>A. Color Doppler shows membranous VSD location size, and presence of often multiple fenestrations in AMS.</p> <p>B. Color Doppler of subpulmonic VSD jet below PV.</p> <p>C. Spectral Doppler through the VSD without contamination from the TR jet, which is in the opposite direction. High VSD jet velocity suggests normal estimated PA pressure.</p> <p>D. Color aliasing through the infundibular os (subpulmonic area) alerts to presence of DCRV.</p>
<p><b>Imaging level: ME aortic long axis 110°–150° view</b></p>		
<p><b>Acquisition protocol:</b></p>		
<ul style="list-style-type: none"> <li>• Maneuver: advance, anteflex</li> <li>• Angulation from 110°–150° and/or rotation of the probe clockwise to TV valve and counterclockwise to PV can achieve optimal visualization of membranous and subpulmonic VSD and proximity to Ao leaflets.</li> </ul> 		

(Continued)

Table 10 (Continued)



- A. Membranous VSD with an AMS, immediately below the AV but posterior and distant from the PV (not shown).
- B. Subpulmonic VSD located immediately below the AV and PV.
- C. Subaortic membrane, associated with membranous VSD, in the LVOT

- A. Three-dimensional imaging from the ME view shows a muscular VSD (outlined in yellow) en face, allowing an assessment of defect size and shape.
- B. Three-dimensional multiplanar reconstruction can be performed to visualize the defect en face. In this example there is a very small membranous septal defect (yellow asterisk), which aligned in the short axis and 3D views using the orthogonal green and red planes.

- A. Distance between a membranous VSD and the AV and/or AMS is important for transcatheter closure.
- B. AV prolapse and regurgitation in the case of subpulmonary VSD with jet directed below the PV. The systolic VSD shunt and diastolic regurgitation may not be seen in the same still frame
- C. AV prolapse nearly occluding this membranous VSD. Note that the PV is not seen in this image.

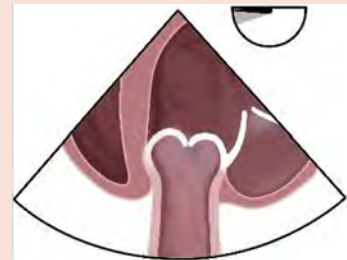
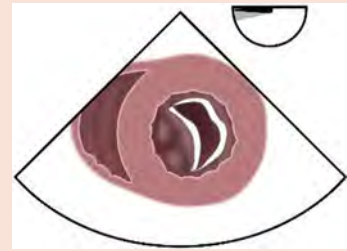
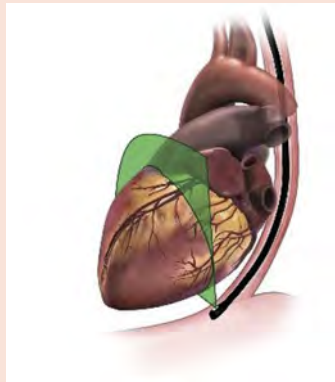
(Continued)

**Table 10** (Continued)

**Imaging level: TG and DT 0°–60°**

**Acquisition protocol:**

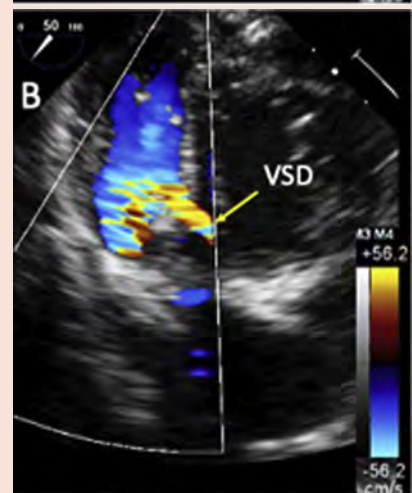
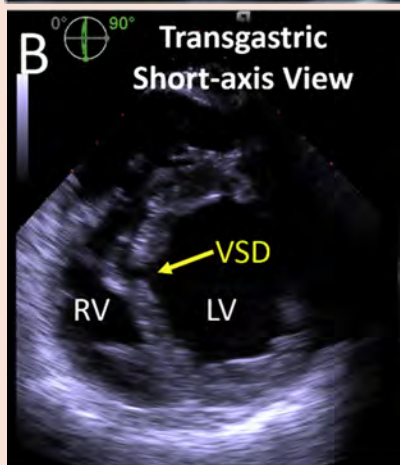
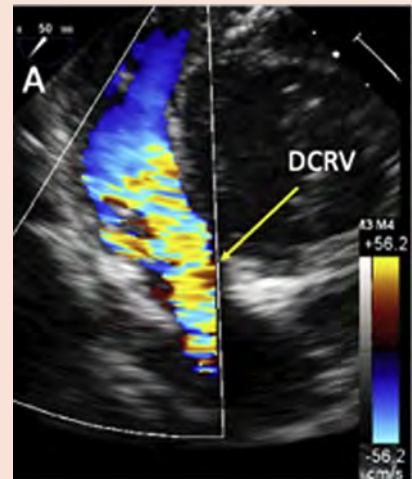
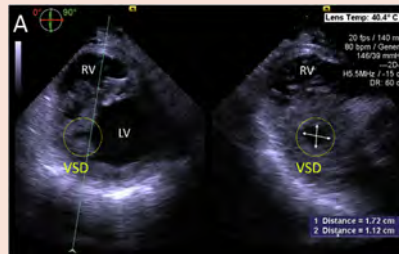
- Advance and strong flexion, 0°–60° rotation to demonstrate the LVOT and membranous VSD.
- Leftward rotation to display the RVOT and DCRV.



**Planar imaging**

**Volumetric imaging**

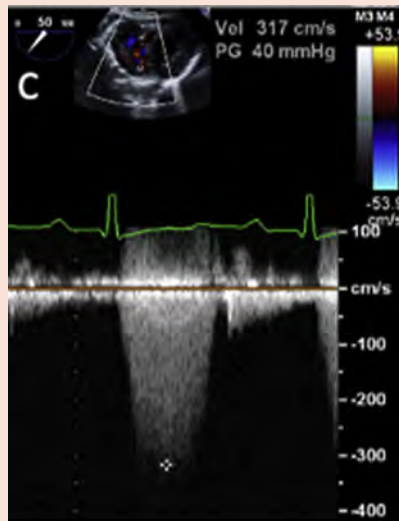
**Functional imaging**



(Continued)

Table 10 (Continued)

Planar imaging	Volumetric imaging	Functional imaging
<p>A. Membranous VSD and AMS may be visualized from TG between 0°–60°.</p> <p>B. From TG SAX views (0°) the muscular VSD with echo dropout of the interventricular septum (<i>yellow arrow</i>) can be clearly imaged.</p>	<p>A. The same patient in planar imaging <b>panel B</b> is now imaged using biplane mode with the SAX of the VSD imaged in the orthogonal view.</p>	<p>A. DCRV demonstrated as color aliasing in the subpulmonic region due to infundibular os narrowing.</p> <p>B. Rotation of the probe demonstrates the membranous VSD jet separate from the RVOT flow.</p> <p>C. Peak spectral Doppler gradient obtained in ideal alignment from this view.</p>



4Ch, Four-chamber; AMS, aneurysm of the membranous septum; Ao, aorta; AVC, atrioventricular canal; DCRV, double-chambered right ventricle; LA, left atrium; LV, left ventricle; LVOT, left ventricular outflow tract; PG, pressure gradient; RA, right atrium; RV, right ventricle; Vel, velocity.

may display aneurysmal accessory tissue associated with the TV and/or aneurysm of the membranous septum, resulting in variable TR and/or LV-to-right atrial shunting. Aneurysms of the membranous septum may have multiple defects within the tissue that can be difficult to delineate individually because of hypermobility of the thin tissue. Transcatheter closure can be performed in these cases, and indeed, device placement within the aneurysm may be a preferable approach to further reduce the low risk for complete heart block that is described with surgical perimembranous VSD closure.<sup>163</sup> Spectral and color Doppler interrogation of the defect as well as the TR jet should be performed; it is crucial to differentiate TR from VSD flow to avoid overestimating the PA pressure. The 45° to 60° view will also demonstrate AR, possibly indicating AV prolapse, which is associated with perimembranous VSD, and necessitates surgical rather than transcatheter intervention.

The ME AV long-axis view at 110° to 150° is orthogonal to the first recommended view, is important to evaluate the size of the defect, and may provide a better angle for spectral Doppler sampling. This view is ideal to measure the distance of the defect from the AV insertion, as it represents the superior rim that will be needed to seat a device. With the current wide range of septal occluders, vascular

plugs and asymmetric VSD devices, transcatheter closure may be possible with even minimal subaortic rims. AV prolapse can be readily appreciated in this view as distortion of the noncoronary or right coronary commissure and associated AR due to the Venturi effect.<sup>164,165</sup> AV prolapse without regurgitation does not mandate VSD closure if the defect does not otherwise warrant closure.<sup>165</sup>

**TG Views.** From the TG location, the entirety of the muscular septum can be evaluated in increments of 15° covering base to apex. This is the ideal position to identify and characterize most types of congenital and acquired muscular VSDs. These defects may be serpiginous, have multiple points of exit within RV trabeculations, and are best characterized from an angle showing most of the defect in the long axis. Delineation of the surrounding tissue and maximal diameter will inform candidacy for device closure.

**Three-Dimensional Imaging.** Three-dimensional imaging can be obtained from whichever TEE level demonstrates the VSD most clearly on 2D imaging. The en face views from RV and LV aspects, and ME four-chamber view best demonstrate the anatomic features.<sup>166</sup> Real-time 3D imaging shows the dynamic changes in defect

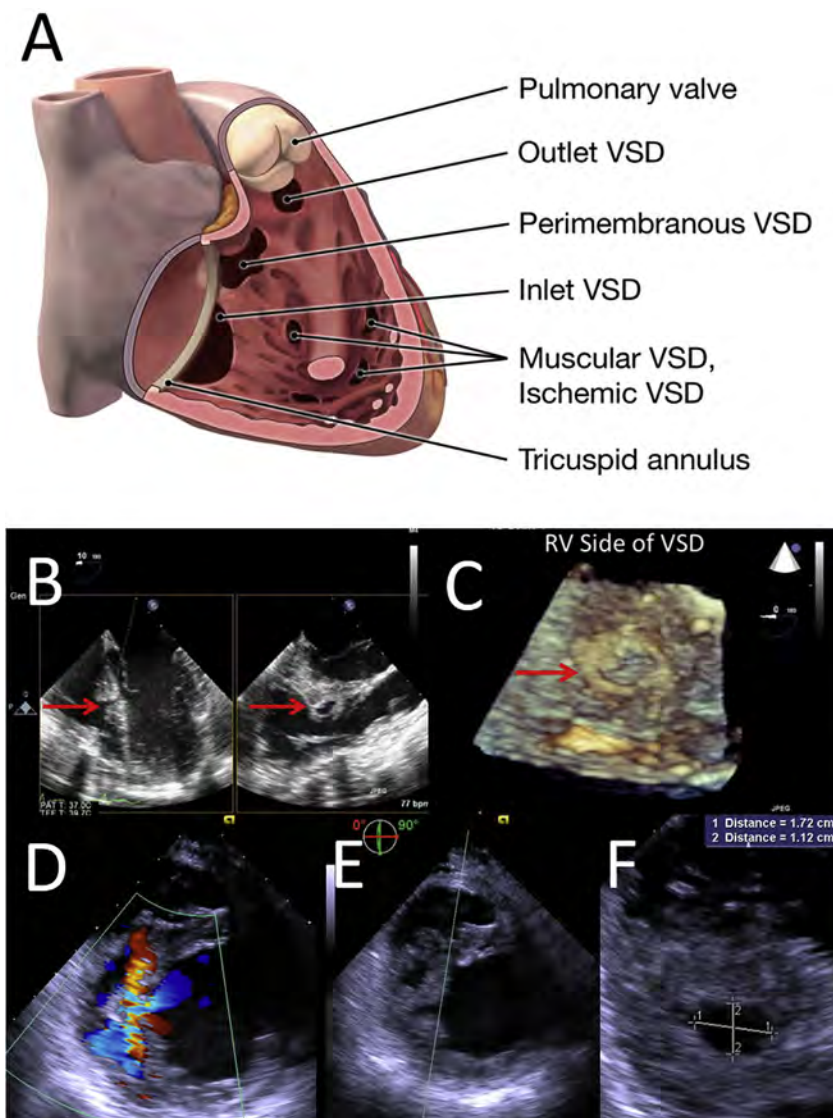


**Figure 33** VSD classification. VSDs may be located anywhere within the septum (A). Muscular VSDs may be congenital or a consequence of trauma (B, C) or myocardial infarction (D–F). Unlike the other VSD types, these defects are typically surrounded by myocardium and thus are usually amenable to device closure. The dynamic shape and size of the defects should be characterized by 2D (B), 3D (C), and color Doppler (D) echocardiography from the ME and TG views.

size and shape from both the left and right ventricular aspects to facilitate device selection.

## CONCLUSION

Current American College of Cardiology and American Heart Association guidelines suggest that echocardiographers who are members of multidisciplinary teams taking care of patients with structural heart disease should have expertise in valve disease and transcatheter and surgical interventions, whether or not they are guiding procedures.<sup>4</sup> The present document is a reference guideline focused on the acquisition of essential TEE images for structural heart disease assessment before intervention. These imaging protocols are intended to facilitate the multidisciplinary team's shared decision-making by

identifying (1) the mechanism of structural or valvular dysfunction, (2) the hemodynamics as well as anatomic severity of the disease, and (3) the specific anatomic features that may determine candidacy for intervention.

**NOTICE AND DISCLAIMER:** This report is made available by ASE as a courtesy reference source for members. This report contains recommendations only and should not be used as the sole basis to make medical practice decisions or for disciplinary action against any employee. The statements and recommendations contained in this report are based primarily on the opinions of experts rather than on scientifically verified data. The ASE makes no express or implied warranties regarding the completeness or accuracy of the information in this report, including the warranty of merchantability or fitness for a particular purpose. In no event shall the ASE be liable to you, your patients, or any other third parties for any decision made or

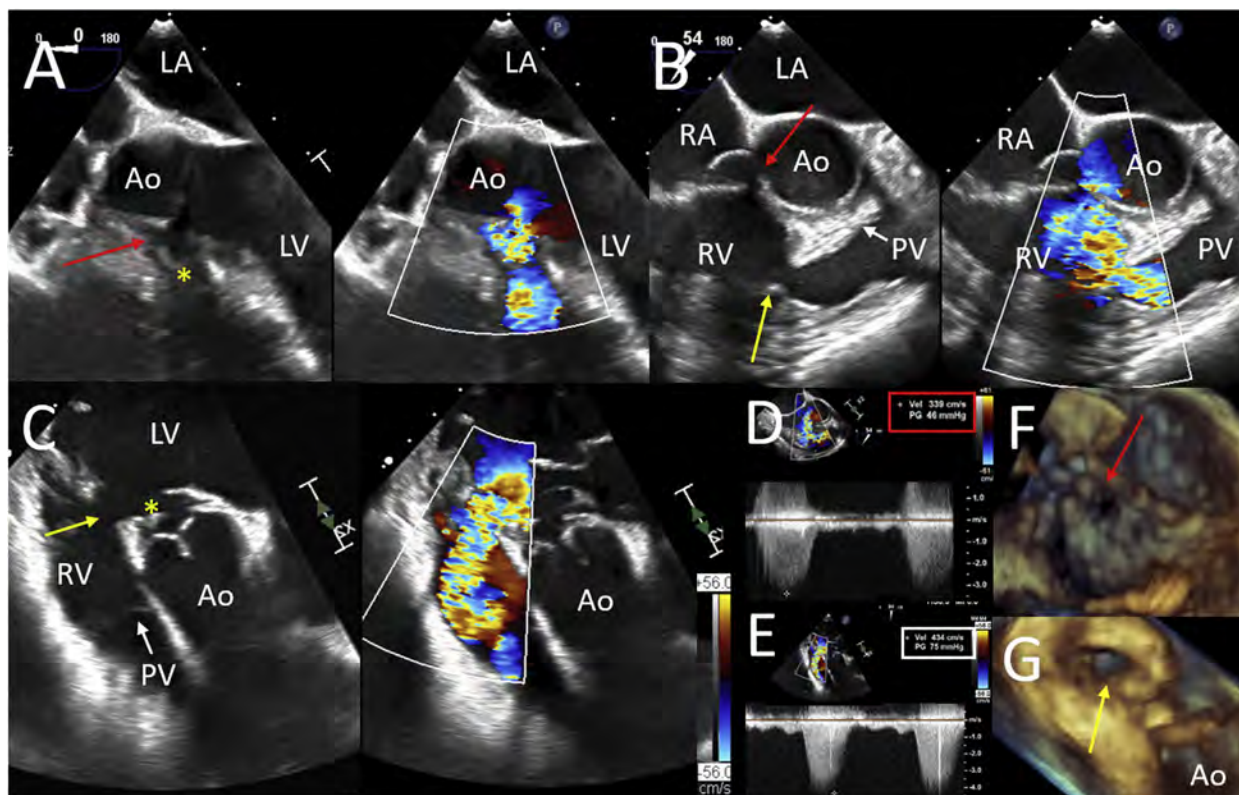


**Figure 34** Perimembranous ventricular septal defect (VSD) and double-chambered right ventricle (DCRV). Perimembranous VSD is sometimes, but not always amenable to transcatheter closure. In this example mid-esophageal (ME) imaging (panels **A**, **B**) demonstrates the VSD (red arrow), proximity to the aortic valve, presence of aneurysm of the membranous septum (\*), and defect size and shape. (**B**) Narrowing of the infundibulum due to DCRV (yellow arrow) as well as color aliasing is seen below the pulmonic valve. (**C**) Deep transgastric (DT) views allow a clearer image of the narrowed infundibulum (yellow arrow) and membranous septal aneurysm (yellow asterisk) with color Doppler flow across the infundibulum aligned with the ultrasound beam. RV systolic pressure is estimated by CW Doppler through the VSD however from ME views the measured VSD gradient is low at 45 mm Hg (panel **D**). Peak DCRV Doppler gradient is measured from the DT view (panel **E**, see also [Figures 22A](#) and [B](#)) and is in this case severe and resulted in the low VSD gradient. These findings are indicative of right ventricular but not pulmonary arterial hypertension. ME 3D imaging shows the VSD as viewed from the aortic root (red arrow, **F**) and 3D DT imaging shows the severe infundibular stenosis due to DCRV (yellow arrow, **G**). This patient was not a candidate for transcatheter closure, rather was sent for surgery due to DCRV and proximity of the defect to the aortic valve. Ao, Aorta; PV, pulmonic valve.

action taken by you or such other parties in reliance on this information. Nor does your use of this information constitute the offering of medical advice by the ASE or create any physician-patient relationship between the ASE and your patients or anyone else.

#### ACKNOWLEDGMENTS

This document was reviewed by members of the 2020–2021 ASE Guidelines and Standards Committee, ASE Board of Directors, ASE Executive Committee, and designated reviewers. Reviewers included Piers Barker, MD, FASE, Meryl Cohen, MD, FASE, Benjamin Freed, MD, FASE, Edward Gill, MD, FASE, David Harrild, MD, FASE, Lanqi Hua, ACS, APCA, RDCS, FASE, Thomas Johnson, MD, FASE, Anuj Mediratta, MD, FASE, David Orsinelli, MD, FASE, Anitha Parthiban, MD, FASE, Alan S. Pearlman, MD, FASE, Andrew Pellett, PhD, RDCS, FASE, Geoffrey A. Rose, MD, FASE, and David H. Wiener, MD, FASE.

#### REFERENCES

1. Hahn RT, Abraham T, Adams MS, Bruce CJ, Glas KE, Lang RM, et al. Guidelines for performing a comprehensive transesophageal echocardiographic examination: recommendations from the American Society of Echocardiography and the Society of Cardiovascular Anesthesiologists. *J Am Soc Echocardiogr* 2013;26:921-64.
2. Wieggers SE, Ryan T, Arrighi JA, Brown SM, Canaday B, Damp JB, et al. 2019 ACC/AHA/ASE advanced training statement on echocardiography (revision of the 2003 ACC/AHA clinical competence statement on echocardiography): a report of the ACC Competency Management Committee. *J Am Soc Echocardiogr* 2019;32:919-43.
3. Hahn RT, Mahmood F, Kodali S, Lang R, Monaghan M, Gillam LD, et al. Core competencies in echocardiography for imaging structural heart disease interventions: an expert consensus statement. *JACC Cardiovasc Imaging* 2019;12:2560-70.
4. Otto CM, Nishimura RA, Bonow RO, Carabello BA, Erwin JP III, Gentile F, et al. 2020 ACC/AHA guideline for the management of patients with valvular heart disease: executive summary: a report of the American College of Cardiology/American Heart Association Joint

- Committee on Clinical Practice Guidelines. *J Am Coll Cardiol* 2021;77:450-500.
5. Quinones MA, Douglas PS, Foster E, Gorcsan J III, Lewis JF, Pearlman AS, et al. ACC/AHA clinical competence statement on echocardiography: a report of the American College of Cardiology/American Heart Association/American College of Physicians-American Society of Internal Medicine Task Force on Clinical Competence. *J Am Soc Echocardiogr* 2003;16:379-402.
  6. Zoghbi WA, Adams D, Bonow RO, Enriquez-Sarano M, Foster E, Grayburn PA, et al. Recommendations for noninvasive evaluation of native valvular regurgitation: a report from the American Society of Echocardiography developed in collaboration with the Society for Cardiovascular Magnetic Resonance. *J Am Soc Echocardiogr* 2017;30:303-71.
  7. Baumgartner H, Hung J, Bermejo J, Chambers JB, Edvardsen T, Goldstein S, et al. Recommendations on the echocardiographic assessment of aortic valve stenosis: a focused update from the European Association of Cardiovascular Imaging and the American Society of Echocardiography. *J Am Soc Echocardiogr* 2017;30:372-92.
  8. Lang RM, Badano LP, Mor-Avi V, Afilalo J, Armstrong A, Ernande L, et al. Recommendations for cardiac chamber quantification by echocardiography in adults: an update from the American Society of Echocardiography and the European Association of Cardiovascular Imaging. *J Am Soc Echocardiogr* 2015;28:1-39.e14.
  9. Ozpelit E, Akdeniz B, Ozpelit EM, Tas S, Alpaslan E, Bozkurt S, et al. Impact of severe tricuspid regurgitation on accuracy of echocardiographic pulmonary artery systolic pressure estimation. *Echocardiography* 2015;32:1483-90.
  10. Rudski LG, Lai WW, Afilalo J, Hua L, Handschumacher MD, Chandrasekaran K, et al. Guidelines for the echocardiographic assessment of the right heart in adults: a report from the American Society of Echocardiography endorsed by the European Association of Echocardiography, a registered branch of the European Society of Cardiology, and the Canadian Society of Echocardiography. *J Am Soc Echocardiogr* 2010;23:685-713; quiz 86-8.
  11. Lang RM, Badano LP, Tsang W, Adams DH, Agricola E, Buck T, et al. EAE/ASE recommendations for image acquisition and display using three-dimensional echocardiography. *J Am Soc Echocardiogr* 2012;25:3-46.
  12. Badano LP, Agricola E, Perez de Isla L, Gianfagna P, Zamorano JL. Evaluation of the tricuspid valve morphology and function by transthoracic real-time three-dimensional echocardiography. *Eur J Echocardiogr* 2009;10:477-84.
  13. Faletra FF, Ramamurthi A, Dequarti MC, Leo LA, Moccetti T, Pandian N. Artifacts in three-dimensional transesophageal echocardiography. *J Am Soc Echocardiogr* 2014;27:453-62.
  14. Yoon SH, Schmidt T, Bleiziffer S, Schofer N, Fiorina C, Munoz-Garcia AJ, et al. Transcatheter aortic valve replacement in pure native aortic valve regurgitation. *J Am Coll Cardiol* 2017;70:2752-63.
  15. Hensey M, Murdoch DJ, Sathananthan J, Alenezi A, Sathananthan G, Moss R, et al. First-in-human experience of a new-generation transfemoral transcatheter aortic valve for the treatment of severe aortic regurgitation: the J-Valve transfemoral system. *EuroIntervention* 2019;14:e1553-5.
  16. Seiffert M, Bader R, Kappert U, Rastan A, Krapf S, Bleiziffer S, et al. Initial German experience with transapical implantation of a second-generation transcatheter heart valve for the treatment of aortic regurgitation. *JACC Cardiovasc Interv* 2014;7:1168-74.
  17. Hahn RT, Nicoara A, Kapadia S, Svensson L, Martin R. Echocardiographic imaging for transcatheter aortic valve replacement. *J Am Soc Echocardiogr* 2018;31:405-33.
  18. Ho SY. Structure and anatomy of the aortic root. *Eur J Echocardiogr* 2009;10:i3-10.
  19. Anderson RH. Clinical anatomy of the aortic root. *Heart* 2000;84:670-3.
  20. Maeno Y, Abramowitz Y, Kawamori H, Kazuno Y, Kubo S, Takahashi N, et al. A highly predictive risk model for pacemaker implantation after TAVR. *JACC Cardiovasc Imaging* 2017;10:1139-47.
  21. Goldstein SA, Evangelista A, Abbara S, Arai A, Asch FM, Badano LP, et al. Multimodality imaging of diseases of the thoracic aorta in adults: from the American Society of Echocardiography and the European Association of Cardiovascular Imaging: endorsed by the Society of Cardiovascular Computed Tomography and Society for Cardiovascular Magnetic Resonance. *J Am Soc Echocardiogr* 2015;28:119-82.
  22. Clavel MA, Malouf J, Messika-Zeitoun D, Araoz PA, Michelena HI, Enriquez-Sarano M. Aortic valve area calculation in aortic stenosis by CT and Doppler echocardiography. *JACC Cardiovasc Imaging* 2015;8:248-57.
  23. Malouf J, Le Tourneau T, Pellikka P, Sundt TM, Scott C, Schaff HV, et al. Aortic valve stenosis in community medical practice: determinants of outcome and implications for aortic valve replacement. *J Thorac Cardiovasc Surg* 2012;144:1421-7.
  24. Thaden JJ, Nkomo VT, Lee KJ, Oh JK. Doppler imaging in aortic stenosis: the importance of the nonapical imaging windows to determine severity in a contemporary cohort. *J Am Soc Echocardiogr* 2015;28:780-5.
  25. Bernard Y, Meneveau N, Vuilleminot A, Magnin D, Anguenot T, Schiele F, et al. Planimetry of aortic valve area using multiplane transoesophageal echocardiography is not a reliable method for assessing severity of aortic stenosis. *Heart* 1997;78:68-73.
  26. Shirazi S, Golmohammadi F, Tavooosi A, Salehi M, Larti F, Sardari A, et al. Quantification of aortic valve area: comparison of different methods of echocardiography with 3-D scan of the excised valve. *Int J Cardiovasc Imaging* 2021;37:529-38.
  27. Anger T, Bauer V, Plachtzik C, Geisler T, Gawaz MP, Oberhoff M, et al. Non-invasive and invasive evaluation of aortic valve area in 100 patients with severe aortic valve stenosis: comparison of cardiac computed tomography with echo (transesophageal/transsthoracic) and catheter examination. *J Cardiol* 2014;63:189-97.
  28. Klass O, Walker MJ, Olszewski ME, Bahner J, Feuerlein S, Hoffmann MH, et al. Quantification of aortic valve area at 256-slice computed tomography: comparison with transesophageal echocardiography and cardiac catheterization in subjects with high-grade aortic valve stenosis prior to percutaneous valve replacement. *Eur J Radiol* 2011;80:151-7.
  29. Boodhwani M, de Kerchove L, Glineur D, Poncelet A, Rubay J, Astarci P, et al. Repair-oriented classification of aortic insufficiency: impact on surgical techniques and clinical outcomes. *J Thorac Cardiovasc Surg* 2009;137:286-94.
  30. Rusted IE, Scheifley CH, Edwards JE. Studies of the mitral valve. I. Anatomic features of the normal mitral valve and associated structures. *Circulation* 1952;6:825-31.
  31. Perloff JK, Roberts WC. The mitral apparatus. Functional anatomy of mitral regurgitation. *Circulation* 1972;46:227-39.
  32. Ho SY. Anatomy of the mitral valve. *Heart* 2002;88(suppl 4):iv5-10.
  33. Faletra FF, Leo LA, Paiocchi VL, Caretta A, Viani GM, Schlossbauer SA, et al. Anatomy of mitral annulus insights from non-invasive imaging techniques. *Eur Heart J Cardiovasc Imaging* 2019;20:843-57.
  34. Levine RA, Handschumacher MD, Sanfilippo AJ, Hagege AA, Harrigan P, Marshall JE, et al. Three-dimensional echocardiographic reconstruction of the mitral valve, with implications for the diagnosis of mitral valve prolapse. *Circulation* 1989;80:589-98.
  35. Blanke P, Naoum C, Webb J, Dvir D, Hahn RT, Grayburn P, et al. Multimodality imaging in the context of transcatheter mitral valve replacement: establishing consensus among modalities and disciplines. *JACC Cardiovasc Imaging* 2015;8:1191-208.
  36. Carpentier A. Cardiac valve surgery—the “French correction”. *J Thorac Cardiovasc Surg* 1983;86:323-37.
  37. Shah PM. Current concepts in mitral valve prolapse—diagnosis and management. *J Cardiol* 2010;56:125-33.

38. Hyodo E, Iwata S, Tugcu A, Oe Y, Koczo A, Shimada K, et al. Accurate measurement of mitral annular area by using single and biplane linear measurements: comparison of conventional methods with the three-dimensional planimetric method. *Eur Heart J Cardiovasc Imaging* 2012;13:605-11.
39. Wang W, Wang Z, Li J, Gong K, Zhao L, Tang G, et al. The impact of different geometric assumption of mitral annulus on the assessment of mitral regurgitation volume by Doppler method. *Cardiovasc Ultrasound* 2020;18:5.
40. Sud K, Agarwal S, Parashar A, Raza MQ, Patel K, Min D, et al. Degenerative mitral stenosis: unmet need for percutaneous interventions. *Circulation* 2016;133:1594-604.
41. Guerrero M, Urena M, Himbert D, Wang DD, Eleid M, Kodali S, et al. 1-year outcomes of transcatheter mitral valve replacement in patients with severe mitral annular calcification. *J Am Coll Cardiol* 2018;71:1841-53.
42. Russell HM, Guerrero ME, Salinger MH, Manzuk MA, Pursnani AK, Wang D, et al. Open atrial transcatheter mitral valve replacement in patients with mitral annular calcification. *J Am Coll Cardiol* 2018;72:1437-48.
43. Baumgartner H, Hung J, Bermejo J, Chambers JB, Evangelista A, Griffin BP, et al. Echocardiographic assessment of valve stenosis: EAE/ASE recommendations for clinical practice. *J Am Soc Echocardiogr* 2009;22:1-23; quiz 101-2.
44. Zamorano J, Cordeiro P, Sugeng L, Perez de Isla L, Weinert L, Macaya C, et al. Real-time three-dimensional echocardiography for rheumatic mitral valve stenosis evaluation: an accurate and novel approach. *J Am Coll Cardiol* 2004;43:2091-6.
45. Schlosshan D, Aggarwal G, Mathur G, Allan R, Cranney G. Real-time 3D transesophageal echocardiography for the evaluation of rheumatic mitral stenosis. *JACC Cardiovasc Imaging* 2011;4:580-8.
46. Quinones MA, Otto CM, Stoddard M, Waggoner A, Zoghbi WA. Recommendations for quantification of Doppler echocardiography: a report from the Doppler Quantification Task Force of the Nomenclature and Standards Committee of the American Society of Echocardiography. *J Am Soc Echocardiogr* 2002;15:167-84.
47. Abramowitz Y, Jilaihawi H, Chakravarty T, Mack MJ, Makkar RR. Mitral annulus calcification. *J Am Coll Cardiol* 2015;66:1934-41.
48. Bertrand PB, Mihos CG, Yucel E. Mitral annular calcification and calcific mitral stenosis: therapeutic challenges and considerations. *Curr Treat Options Cardiovasc Med* 2019;21:19.
49. Murphy DJ, Ge Y, Don CW, Keraliya A, Aghayev A, Morgan R, et al. Use of cardiac computerized tomography to predict neo-left ventricular outflow tract obstruction before transcatheter mitral valve replacement. *J Am Heart Assoc* 2017;6:e007353.
50. Vukicevic M, Mosadegh B, Min JK, Little SH. Cardiac 3D printing and its future directions. *JACC Cardiovasc Imaging* 2017;10:171-84.
51. Barasch E, Gottdiener JS, Larsen EK, Chaves PH, Newman AB, Manolio TA. Clinical significance of calcification of the fibrous skeleton of the heart and atherosclerosis in community dwelling elderly. The Cardiovascular Health Study (CHS). *Am Heart J* 2006;151:39-47.
52. Movva R, Murthy K, Romero-Corral A, Seetha Rammohan HR, Fumo P, Pressman GS. Calcification of the mitral valve and annulus: systematic evaluation of effects on valve anatomy and function. *J Am Soc Echocardiogr* 2013;26:1135-42.
53. Kohsaka S, Jin Z, Rundek T, Boden-Albala B, Homma S, Sacco RL, et al. Impact of mitral annular calcification on cardiovascular events in a multi-ethnic community: the Northern Manhattan Study. *JACC Cardiovasc Imaging* 2008;1:617-23.
54. Chu JW, Levine RA, Chua S, Poh KK, Morris E, Hua L, et al. Assessing mitral valve area and orifice geometry in calcific mitral stenosis: a new solution by real-time three-dimensional echocardiography. *J Am Soc Echocardiogr* 2008;21:1006-9.
55. Eleid MF, Foley TA, Said SM, Pislaru SV, Rihal CS. Severe mitral annular calcification: multimodality imaging for therapeutic strategies and interventions. *JACC Cardiovasc Imaging* 2016;9:1318-37.
56. Khan JM, Babaliaros VC, Greenbaum AB, Foerst JR, Yazdani S, McCabe JM, et al. Anterior Leaflet Laceration to Prevent Ventricular Outflow Tract Obstruction During Transcatheter Mitral Valve Replacement. *J Am Coll Cardiol* 2019;73:2521-34.
57. Khan JM, Babaliaros VC, Greenbaum AB, Foerst JR, Yazdani S, McCabe JM, et al. Correction: Anterior Leaflet Laceration to Prevent Ventricular Outflow Tract Obstruction During Transcatheter Mitral Valve Replacement. *J Am Coll Cardiol* 2019;74:595.
58. El Sabbagh A, Reddy YNV, Nishimura RA. Mitral valve regurgitation in the contemporary era: insights into diagnosis, management, and future directions. *JACC Cardiovasc Imaging* 2018;11:628-43.
59. Adams DH, Rosenhek R, Falk V. Degenerative mitral valve regurgitation: best practice revolution. *Eur Heart J* 2010;31:1958-66.
60. Narang A, Addetia K, Weinert L, Yamat M, Shah AP, Blair JE, et al. Diagnosis of isolated cleft mitral valve using three-dimensional echocardiography. *J Am Soc Echocardiogr* 2018;31:1161-7.
61. Séguéla PE, Houyel L, Acar P. Congenital malformations of the mitral valve. *Arch Cardiovasc Dis* 2011;104:465-79.
62. Bonow RO, O'Gara PT, Adams DH, Badhwar V, Bavaria JE, Elmariah S, et al. 2020 focused update of the 2017 ACC expert consensus decision pathway on the management of mitral regurgitation: a report of the American College of Cardiology Solution Set Oversight Committee. *J Am Coll Cardiol* 2020;75:2236-70.
63. Bapat V, Rajagopal V, Meduri C, Farivar RS, Walton A, Duffy SJ, et al. Early experience with new transcatheter mitral valve replacement. *J Am Coll Cardiol* 2018;71:12-21.
64. Kagiya N, Mondillo S, Yoshida K, Mandoli GE, Cameli M. Subtypes of atrial functional mitral regurgitation: imaging insights into their mechanisms and therapeutic implications. *JACC Cardiovasc Imaging* 2020;13:820-35.
65. Deferm S, Bertrand PB, Verbrugge FH, Verhaert D, Rega F, Thomas JD, et al. Atrial functional mitral regurgitation: JACC review topic of the week. *J Am Coll Cardiol* 2019;73:2465-76.
66. Nielsen SL, Nygaard H, Mandrup L, Fontaine AA, Hasenkam JM, He S, et al. Mechanism of incomplete mitral leaflet coaptation—interaction of chordal restraint and changes in mitral leaflet coaptation geometry. Insight from in vitro validation of the premise of force equilibrium. *J Biomech Eng* 2002;124:596-608.
67. Aruta P, Muraru D, Guta AC, Mihaila S, Ruozio N, Palermo C, et al. Comparison of mitral annulus geometry between patients with ischemic and non-ischemic functional mitral regurgitation: implications for transcatheter mitral valve implantation. *Cardiovasc Ultrasound* 2018;16:27.
68. Goebel B, Heck R, Hamadanchi A, Otto S, Doenst T, Jung C, et al. Vena contracta area for severity grading in functional and degenerative mitral regurgitation: a transoesophageal 3D colour Doppler analysis in 500 patients. *Eur Heart J Cardiovasc Imaging* 2018;19:639-46.
69. Fishbein GA, Fishbein MC. Tricuspid and pulmonic valve pathology. *Curr Cardiol Rep* 2019;21:54.
70. Taskesen T, Prabhu SJ, Steinberg ZL, Oxom D, Gill EA. Feasibility of pulmonary valve imaging using transesophageal echocardiography upper esophageal view. *Echocardiography* 2019;36:930-7.
71. Marelli AJ, Mackie AS, Ionescu-Ittu R, Rahme E, Pilote L. Congenital heart disease in the general population: changing prevalence and age distribution. *Circulation* 2007;115:163-72.
72. Stout KK, Daniels CJ, Aboulhosn JA, Bozkurt B, Broberg CS, Colman JM, et al. 2018 AHA/ACC guideline for the management of adults with congenital heart disease: a report of the American College of Cardiology/American Heart Association Task Force on Clinical Practice Guidelines. *Circulation* 2019;139:e698-800.
73. Driscoll D, Allen HD, Atkins DL, Brenner J, Dunnigan A, Franklin W, et al. Guidelines for evaluation and management of common congenital cardiac problems in infants, children, and adolescents. A statement for healthcare professionals from the Committee on Congenital Cardiac Defects of the Council on Cardiovascular Disease in the Young, American Heart Association. *Circulation* 1994;90:2180-8.

74. Valente AM, Cook S, Festa P, Ko HH, Krishnamurthy R, Taylor AM, et al. Multimodality imaging guidelines for patients with repaired tetralogy of Fallot: a report from the American Society of Echocardiography: developed in collaboration with the Society for Cardiovascular Magnetic Resonance and the Society for Pediatric Radiology. *J Am Soc Echocardiogr* 2014;27:111-41.
75. Pellikka PA, Tajik AJ, Khandheria BK, Seward JB, Callahan JA, Pitot HC, et al. Carcinoid heart disease. Clinical and echocardiographic spectrum in 74 patients. *Circulation* 1993;87:1188-96.
76. Maciel BC, Simpson IA, Valdes-Cruz LM, Recusani F, Hoit B, Dalton N, et al. Color flow Doppler mapping studies of "physiologic" pulmonary and tricuspid regurgitation: evidence for true regurgitation as opposed to a valve closing volume. *J Am Soc Echocardiogr* 1991;4:589-97.
77. Puchalski MD, Askovich B, Sower CT, Williams RV, Minich LL, Tani LY. Pulmonary regurgitation: determining severity by echocardiography and magnetic resonance imaging. *Congenit Heart Dis* 2008;3:168-75.
78. Schievano S, Coats L, Migliavacca F, Norman W, Frigiola A, Deanfield J, et al. Variations in right ventricular outflow tract morphology following repair of congenital heart disease: implications for percutaneous pulmonary valve implantation. *J Cardiovasc Magn Reson* 2007;9:687-95.
79. Parikh KN, Shah NC, Clark JB, Myers JL. Pulmonary valve restitution following transannular patch repair of tetralogy of Fallot. *Interact Cardiovasc Thorac Surg* 2017;25:985-6.
80. Bonhoeffer P, Boudjemline Y, Saliba Z, Merckx J, Aggoun Y, Bonnet D, et al. Percutaneous replacement of pulmonary valve in a right-ventricle to pulmonary-artery prosthetic conduit with valve dysfunction. *Lancet* 2000;356:1403-5.
81. Wang N, Fulcher J, Abeysuriya N, McGrady M, Wilcox J, Celermajer D, et al. Tricuspid regurgitation is associated with increased mortality independent of pulmonary pressures and right heart failure: a systematic review and meta-analysis. *Eur Heart J* 2019;40:476-84.
82. Dreyfus GD, Martin RP, Chan KM, Dulguerov F, Alexandrescu C. Functional tricuspid regurgitation: a need to revise our understanding. *J Am Coll Cardiol* 2015;65:2331-6.
83. Zack CJ, Fender EA, Chandrashekar P, Reddy YNV, Bennett CE, Stulak JM, et al. National trends and outcomes in isolated tricuspid valve surgery. *J Am Coll Cardiol* 2017;70:2953-60.
84. Taramasso M, Alessandrini H, Latib A, Asami M, Attinger-Toller A, Biasco L, et al. Outcomes after current transcatheter tricuspid valve intervention: mid-term results from the international TriValve Registry. *JACC Cardiovasc Interv* 2019;12:155-65.
85. Hahn RT. State-of-the-art review of echocardiographic imaging in the evaluation and treatment of functional tricuspid regurgitation. *Circ Cardiovasc Imaging* 2016;9:e005332.
86. Dahou A, Levin D, Reisman M, Hahn RT. Anatomy and physiology of the tricuspid valve. *JACC Cardiovasc Imaging* 2019;12:458-68.
87. Faletta RF, Leo LA, Paiocchi VL, Schlossbauer SA, Borruso MG, Pedrazzini G, et al. Imaging-based tricuspid valve anatomy by computed tomography, magnetic resonance imaging, two and three-dimensional echocardiography: correlation with anatomic specimen. *Eur Heart J Cardiovasc Imaging* 2019;20:1-13.
88. Utsunomiya H, Itabashi Y, Mihara H, Berdejo J, Kobayashi S, Siegel RJ, et al. Functional tricuspid regurgitation caused by chronic atrial fibrillation: a real-time 3-dimensional transesophageal echocardiography study. *Circ Cardiovasc Imaging* 2017;10:e004897.
89. Hahn RT, Weckbach LT, Noack T, Hamid N, Kitamura M, Bae R, et al. Proposal for a standard echocardiographic tricuspid valve nomenclature. *JACC Cardiovasc Imaging* 2021;14:1299-305.
90. Hausleiter J, Braun D, Orban M, Latib A, Lurz P, Boekstegers P, et al. Patient selection, echocardiographic screening and treatment strategies for interventional tricuspid repair using the edge-to-edge repair technique. *EuroIntervention* 2018;14:645-53.
91. Tretter JT, Sarwark AE, Anderson RH, Spicer DE. Assessment of the anatomical variation to be found in the normal tricuspid valve. *Clin Anat* 2016;29:399-407.
92. Silver MD, Lam JH, Ranganathan N, Wigle ED. Morphology of the human tricuspid valve. *Circulation* 1971;43:333-48.
93. Fukuda S, Saracino G, Matsumura Y, Daimon M, Tran H, Greenberg NL, et al. Three-dimensional geometry of the tricuspid annulus in healthy subjects and in patients with functional tricuspid regurgitation: a real-time, 3-dimensional echocardiographic study. *Circulation* 2006;114:1492-8.
94. Anwar AM, Geleijnse ML, Soliman OI, McGhie JS, Frowijn R, Nemes A, et al. Assessment of normal tricuspid valve anatomy in adults by real-time three-dimensional echocardiography. *Int J Cardiovasc Imaging* 2007;23:717-24.
95. Ton-Nu TT, Levine RA, Handschumacher MD, Dorer DJ, Yosefy C, Fan D, et al. Geometric determinants of functional tricuspid regurgitation: insights from 3-dimensional echocardiography. *Circulation* 2006;114:143-9.
96. Addetia K, Muraru D, Veronesi F, Jenei C, Cavalli G, Besser SA, et al. 3-dimensional echocardiographic analysis of the tricuspid annulus provides new insights into tricuspid valve geometry and dynamics. *JACC Cardiovasc Imaging* 2019;12:401-12.
97. Praz F, Khalique OK, Dos Reis Macedo LG, Pulerwitz TC, Jantz J, Wu IY, et al. Comparison between three-dimensional echocardiography and computed tomography for comprehensive tricuspid annulus and valve assessment in severe tricuspid regurgitation: implications for tricuspid regurgitation grading and transcatheter therapies. *J Am Soc Echocardiogr* 2018;31:1190-202.e3.
98. Volpato V, Lang RM, Yamat M, Veronesi F, Weinert L, Tamborini G, et al. Echocardiographic assessment of the tricuspid annulus: the effects of the third dimension and measurement methodology. *J Am Soc Echocardiogr* 2019;32:238-47.
99. Lancellotti P, Moura L, Pierard LA, Agricola E, Popescu BA, Tribouilloy C, et al. European Association of Echocardiography recommendations for the assessment of valvular regurgitation. Part 2: mitral and tricuspid regurgitation (native valve disease). *Eur J Echocardiogr* 2010;11:307-32.
100. Dahou A, Ong G, Hamid N, Avenatti E, Yao J, Hahn RT. Quantifying tricuspid regurgitation severity: a comparison of proximal isovelocity surface area and novel quantitative Doppler methods. *JACC Cardiovasc Imaging* 2019;12:560-2.
101. Hahn RT, Zamorano JL. The need for a new tricuspid regurgitation grading scheme. *Eur Heart J Cardiovasc Imaging* 2017;18:1342-3.
102. Santoro C, Marco Del Castillo A, Gonzalez-Gomez A, Monteagudo JM, Hinojar R, Lorente A, et al. Mid-term outcome of severe tricuspid regurgitation: are there any differences according to mechanism and severity? *Eur Heart J Cardiovasc Imaging* 2019;20:1035-42.
103. Peri Y, Sadeh B, Sherez C, Hochstadt A, Biner S, Aviram G, et al. Quantitative assessment of effective regurgitant orifice: impact on risk stratification, and cut-off for severe and torrential tricuspid regurgitation grade. *Eur Heart J Cardiovasc Imaging* 2019;21:768-76.
104. Utsunomiya H, Harada Y, Susawa H, Takahari K, Ueda Y, Izumi K, et al. Comprehensive evaluation of tricuspid regurgitation location and severity using vena contracta analysis: a color Doppler three-dimensional transesophageal echocardiographic study. *J Am Soc Echocardiogr* 2019;32:1526-37.e2.
105. Kebed KY, Addetia K, Henry M, Yamat M, Weinert L, Besser SA, et al. Refining severe tricuspid regurgitation definition by echocardiography with a new outcomes-based "massive" grade. *J Am Soc Echocardiogr* 2020;33:1087-94.
106. Muraru D, Previtiero M, Ochoa-Jimenez RC, Guta AC, Figliozzi S, Gregori D, Bottigliengo D, Parati G, Badano LP. Prognostic validation of partition values for quantitative parameters to grade functional tricuspid regurgitation severity by conventional echocardiography. *Eur Heart J Cardiovasc Imaging* 2021 Jan 22;22(2):155-65.
107. Waller BF, Howard J, Fess S. Pathology of tricuspid valve stenosis and pure tricuspid regurgitation—part I. *Clin Cardiol* 1995;18:97-102.
108. Husain A, Raja FT, Fatallah A, Fadel B, Alsanei A, Raja FT, et al. Tricuspid stenosis: an emerging disease in cardiac implantable

- electronic devices era. Case report and literature review. *J Cardiol Cases* 2017;15:190-3.
109. Vieitez JM, Monteagudo JM, Mahia P, Perez L, Lopez T, Marco I, et al. New insights of tricuspid regurgitation: a large-scale prospective cohort study. *Eur Heart J Cardiovasc Imaging* 2021;22:196-202.
  110. Addetia K, Harb SC, Hahn RT, Kapadia S, Lang RM. Cardiac implantable electronic device lead-induced tricuspid regurgitation. *JACC Cardiovasc Imaging* 2019;12:622-36.
  111. Muraru D, Addetia K, Guta AC, Ochoa-Jimenez RC, Genovese D, Veronesi F, Basso C, Iliceto S, Badano LP, Lang RM. Right atrial volume is a major determinant of tricuspid annulus area in functional tricuspid regurgitation: a three-dimensional echocardiographic study. *Eur Heart J Cardiovasc Imaging* 2021 May 10;22(6):660-9.
  112. Wehrum T, Lodemann T, Hagenlocher P, Stuplich J, Ngo BTT, Grundmann S, et al. Age-related changes of right atrial morphology and inflow pattern assessed using 4D flow cardiovascular magnetic resonance: results of a population-based study. *J Cardiovasc Magn Reson* 2018;20:38.
  113. Holmes DR, Reddy VY, Turi ZG, Doshi SK, Sievert H, Buchbinder M, et al. Percutaneous closure of the left atrial appendage versus warfarin therapy for prevention of stroke in patients with atrial fibrillation: a randomised non-inferiority trial. *Lancet* 2009;374:534-42.
  114. Beigel R, Wunderlich NC, Ho SY, Arsanjani R, Siegel RJ. The left atrial appendage: anatomy, function, and noninvasive evaluation. *JACC Cardiovasc Imaging* 2014;7:1251-65.
  115. Lopez-Minguez JR, Gonzalez-Fernandez R, Fernandez-Vegas C, Millan-Nunez V, Fuentes-Canamero ME, Nogales-Asensio JM, et al. Anatomical classification of left atrial appendages in specimens applicable to CT imaging techniques for implantation of Amplatzer Cardiac Plug. *J Cardiovasc Electrophysiol* 2014;25:976-84.
  116. Wunderlich NC, Beigel R, Swaans MJ, Ho SY, Siegel RJ. Percutaneous interventions for left atrial appendage exclusion: options, assessment, and imaging using 2D and 3D echocardiography. *JACC Cardiovasc Imaging* 2015;8:472-88.
  117. Ho SY, McCarthy KP, Faletra FF. Anatomy of the left atrium for interventional echocardiography. *Eur J Echocardiogr* 2011 Oct;12(10):i11-5.
  118. Yamamoto M, Seo Y, Kawamatsu N, Sato K, Sugano A, Machino-Ohtsuka T, et al. Complex left atrial appendage morphology and left atrial appendage thrombus formation in patients with atrial fibrillation. *Circ Cardiovasc Imaging* 2014;7:337-43.
  119. Di Biase L, Santangeli P, Anselmino M, Mohanty P, Salvetti I, Gili S, et al. Does the left atrial appendage morphology correlate with the risk of stroke in patients with atrial fibrillation? Results from a multicenter study. *J Am Coll Cardiol* 2012;60:531-8.
  120. Vainrib AF, Harb SC, Jaber W, Benenstien RJ, Aizer A, Chinitz LA, et al. Left atrial appendage occlusion/exclusion: procedural image guidance with transesophageal echocardiography. *J Am Soc Echocardiogr* 2018;31:454-74.
  121. Srivastava MC, See VY, Dawood MY, Price MJ. A review of the LARIAT device: insights from the cumulative clinical experience. *Springerplus* 2015;4:522.
  122. Botto LD, Correa A, Erickson JD. Racial and temporal variations in the prevalence of heart defects. *Pediatrics* 2001;107:E32.
  123. Faletra FF, Leo LA, Paiocchi VL, Schlossbauer SA, Pedrazzini G, Moccetti T, et al. Revisiting anatomy of the interatrial septum and its adjoining atrioventricular junction using noninvasive imaging techniques. *J Am Soc Echocardiogr* 2019;32:580-92.
  124. Faletra FF, Nucifora G, Ho SY. Real-time 3-dimensional transesophageal echocardiography of the atrioventricular septal defect. *Circ Cardiovasc Imaging* 2011;4:e7-9.
  125. Van Praagh S, Carrera ME, Sanders SP, Mayer JE, Van Praagh R. Sinus venosus defects: unroofing of the right pulmonary veins—anatomic and echocardiographic findings and surgical treatment. *Am Heart J* 1994;128:365-79.
  126. Sun T, Fei HW, Huang HL, Chen OD, Zheng ZC, Zhang CJ, et al. Transesophageal echocardiography for coronary sinus imaging in partially unroofed coronary sinus. *Echocardiography* 2014;31:74-82.
  127. Silvestry FE, Cohen MS, Armsby LB, Burkule NJ, Fleishman CE, Hijazi ZM, et al. Guidelines for the echocardiographic assessment of atrial septal defect and patent foramen ovale: from the American Society of Echocardiography and Society for Cardiac Angiography and Interventions. *J Am Soc Echocardiogr* 2015;28:910-58.
  128. Mas JL, Derumeaux G, Guillon B, Massardier E, Hosseini H, Mechtouff L, et al. Patent foramen ovale closure or anticoagulation vs. antiplatelets after stroke. *N Engl J Med* 2017;377:1011-21.
  129. Saver JL, Carroll JD, Thaler DE, Smalling RW, MacDonald LA, Marks DS, et al. Long-term outcomes of patent foramen ovale closure or medical therapy after stroke. *N Engl J Med* 2017;377:1022-32.
  130. Søndergaard L, Kasner SE, Rhodes JF, Andersen G, Iversen HK, Nielsen-Kudsk JE, et al. Patent foramen ovale closure or antiplatelet therapy for cryptogenic stroke. *N Engl J Med* 2017;377:1033-42.
  131. Turc G, Calvet D, Guérin P, Sroussi M, Chatellier G, Mas JL. Closure, anticoagulation, or antiplatelet therapy for cryptogenic stroke with patent foramen ovale: systematic review of randomized trials, sequential meta-analysis, and new insights from the CLOSE study. *J Am Heart Assoc* 2018;7:e008356.
  132. Alqahtani F, Bhirud A, Aljohani S, Mills J, Kawsara A, Runkana A, et al. Intracardiac versus transesophageal echocardiography to guide transcatheter closure of interatrial communications: nationwide trend and comparative analysis. *J Interv Cardiol* 2017;30:234-41.
  133. Truong QB, Dao AQ, Do NT, Le MK. Percutaneous atrial septal defect closure through femoral and transjugular approaches in patients with interrupted inferior vena cava. *J Cardiol Cases* 2018;18:106-9.
  134. Butera G, Romagnoli E, Carminati M, Chessa M, Piazza L, Negura D, et al. Treatment of isolated secundum atrial septal defects: impact of age and defect morphology in 1,013 consecutive patients. *Am Heart J* 2008;156:706-12.
  135. Masseli J, Bertog S, Stanczak L, Blankenbach K, Majunke N, Reiffenstein I, et al. Transcatheter closure of multiple interatrial communications. *Catheter Cardiovasc Interv* 2013;81:825-36.
  136. Baruteau AE, Petit J, Lambert V, Gouton M, Piot D, Brenot P, et al. Transcatheter closure of large atrial septal defects: feasibility and safety in a large adult and pediatric population. *Circ Cardiovasc Interv* 2014;7:837-43.
  137. Amedro P, Bayburt S, Assaidi A, Kreitmann B, Habib G, Fouilloux V, et al. Should transcatheter closure of atrial septal defects with inferior-posterior deficient rim still be attempted? *J Thorac Dis* 2019;11:708-16.
  138. Papa M, Gaspardone A, Fragasso G, Sidoti F, Agricola E, Gioffre G, et al. Feasibility and safety of transcatheter closure of atrial septal defects with deficient posterior rim. *Catheter Cardiovasc Interv* 2013;81:1180-7.
  139. Schneider B, Hofmann T, Justen MH, Meinertz T. Chiari's network: normal anatomic variant or risk factor for arterial embolic events? *J Am Coll Cardiol* 1995;26:203-10.
  140. Goldschlager A, Goldschlager N, Brewster H, Kaplan J. Catheter entrapment in a Chiari network involving an atrial septal defect. *Chest* 1972;62:345-6.
  141. Cooke JC, Gelman JS, Harper RW. Chiari network entanglement and herniation into the left atrium by an atrial septal defect occluder device. *J Am Soc Echocardiogr* 1999;12:601-3.
  142. Samanek M, Voriskova M. Congenital heart disease among 815,569 children born between 1980 and 1990 and their 15-year survival: a prospective Bohemia survival study. *Pediatr Cardiol* 1999;20:411-7.
  143. Meberg A, Otterstad JE, Frøland G, Sørland S, Nitter-Hauge S. Increasing incidence of ventricular septal defects caused by improved detection rate. *Acta Paediatr* 1994;83:653-7.
  144. Cresti A, Giordano R, Koestenberger M, Spadoni I, Scalese M, Limbruno U, et al. Incidence and natural history of neonatal isolated ventricular septal defects: do we know everything? A 6-year single-center Italian experience follow-up. *Congenit Heart Dis* 2018;13:105-12.
  145. Kaul S. The interventricular septum in health and disease. *Am Heart J* 1986;112:568-81.
  146. Allwork SP, Anderson RH. Developmental anatomy of the membranous part of the ventricular septum in the human heart. *Br Heart J* 1979;41:275-80.

147. Lopez L, Houyel L, Colan SD, Anderson RH, Béland MJ, Aiello VD, et al. Classification of ventricular septal defects for the eleventh iteration of the International Classification of Diseases—striving for consensus: a report from the International Society for Nomenclature of Paediatric and Congenital Heart Disease. *Ann Thorac Surg* 2018;106:1578-89.
148. Lin K, Zhu D, Tao K, Gan C, Tang H, Feng Y, et al. Hybrid perventricular device closure of doubly committed subarterial ventricular septal defects: mid-term results. *Catheter Cardiovasc Interv* 2013;82:E225-32.
149. Pan S, Xing Q, Cao Q, Wang P, Duan S, Wu Q, et al. Perventricular device closure of doubly committed subarterial ventral septal defect through left anterior minithoracotomy on beating hearts. *Ann Thorac Surg* 2012;94:2070-5.
150. Zhang S, Zhu D, An Q, Tang H, Li D, Lin K. Minimally invasive perventricular device closure of doubly committed sub-arterial ventricular septal defects: single center long-term follow-up results. *J Cardiothorac Surg* 2015;10:119.
151. Lai WW, Mertens L, Cohen M, Geva T. Echocardiography in pediatric and congenital heart disease: from fetus to adult. 2nd ed. Chichester, West Sussex; Hoboken, NJ: Wiley Blackwell/John Wiley & Sons Inc.; 2016.
152. Glen S, Burns J, Bloomfield P. Prevalence and development of additional cardiac abnormalities in 1448 patients with congenital ventricular septal defects. *Heart* 2004;90:1321-5.
153. Baumgartner H, Bonhoeffer P, De Groot NM, de Haan F, Deanfield JE, Galie N, et al. ESC Guidelines for the management of grown-up congenital heart disease (new version 2010). *Eur Heart J* 2010;31:2915-57.
154. Eroglu AG, Oztunc F, Saltik L, Bakari S, Dedeoglu S, Ahunbay G. Evolution of ventricular septal defect with special reference to spontaneous closure rate, subaortic ridge and aortic valve prolapse. *Pediatr Cardiol* 2003;24:31-5.
155. Leichter DA, Sullivan I, Gersony WM. "Acquired" discrete subvalvular aortic stenosis: natural history and hemodynamics. *J Am Coll Cardiol* 1989;14:1539-44.
156. Simpson WF Jr, Sade RM, Crawford FA, Taylor AB, Fyfe DA. Double-chambered right ventricle. *Ann Thorac Surg* 1987;44:7-10.
157. Santhanam H, Yang L, Chen Z, Tai BC, Rajgor DD, Quek SC. A meta-analysis of transcatheter device closure of perimembranous ventricular septal defect. *Int J Cardiol* 2018;254:75-83.
158. Saurav A, Kaushik M, Mahesh Alla V, White MD, Satpathy R, Lanspa T, et al. Comparison of percutaneous device closure versus surgical closure of peri-membranous ventricular septal defects: a systematic review and meta-analysis. *Catheter Cardiovasc Interv* 2015;86:1048-56.
159. Yi K, You T, Ding ZH, Hou XD, Liu XG, Wang XK, et al. Comparison of transcatheter closure, mini-invasive closure, and open-heart surgical repair for treatment of perimembranous ventricular septal defects in children: a PRISMA-compliant network meta-analysis of randomized and observational studies. *Medicine (Baltimore)* 2018;97:e12583.
160. Wilson WM, Horlick EM. Management of post-myocardial infarction ventricular septal rupture. *EuroIntervention* 2016;12(suppl X):X18-23.
161. Omar S, Morgan GL, Panchal HB, Thourani V, Rihal CS, Patel R, et al. Management of post-myocardial infarction ventricular septal defects: a critical assessment. *J Interv Cardiol* 2018;31:939-48.
162. Dehghani P, Ibrahim R, Collins N, Latter D, Cheema AN, Chisholm RJ. Post-traumatic ventricular septal defects—review of the literature and a novel technique for percutaneous closure. *J Invasive Cardiol* 2009;21:483-7.
163. Landman G, Kipps A, Moore P, Teitel D, Meadows J. Outcomes of a modified approach to transcatheter closure of perimembranous ventricular septal defects. *Catheter Cardiovasc Interv* 2013;82:143-9.
164. Tatsuno K, Konno S, Ando M, Sakakibara S. Pathogenetic mechanisms of prolapsing aortic valve and aortic regurgitation associated with ventricular septal defect. Anatomical, angiographic, and surgical considerations. *Circulation* 1973;48:1028-37.
165. Tweddell JS, Pelech AN, Frommelt PC. Ventricular septal defect and aortic valve regurgitation: pathophysiology and indications for surgery. *Semin Thorac Cardiovasc Surg Pediatr Card Surg Annu* 2006;147-52.
166. Puchalski MD, Lui GK, Miller-Hance WC, Brook MM, Young LT, Bhat A, et al. Guidelines for performing a comprehensive transesophageal echocardiographic: examination in children and all patients with congenital heart disease: recommendations from the American Society of Echocardiography. *J Am Soc Echocardiogr* 2019;32:173-215.